An implicit non-ordinary state-based peridynamics for large deformation solid mechanics problems

NUR ANIRA ASYIKIN BINTI HASHIM

HASHIM, NUR ANIRA ASYIKIN BINTI (2021) An implicit non-ordinary state-based peridynamics for large deformation solid mechanics problems. Doctoral thesis, Durham University.

An implicit non-ordinary state-based peridynamics for large deformation solid mechanics problems

Nur Anira Asyikin binti Hashim

Submitted as partial consideration towards
the degree of Doctor of Philosophy

Sustainable Infrastructure Research Challenge
Department of Engineering
Durham University
United Kingdom

May 2021

This thesis is dedicated to
my family

An implicit non-ordinary state-based peridynamics for large deformation solid mechanics problems

Nur Anira Asyikin Hashim

Abstract

The numerical simulation of the cracking process remains one of the most significant challenges in solid mechanics. Compared classical approaches, peridynamics (PD) has some attractive features because the basic equations remain applicable even when singularities appear in the deformation. Numerical time-integration plays a big role in any computational framework and unlike explicit time-integration, implicit time-integration methods can be much more efficient because of the ability to adopt fairly large time increments, making it a suitable option for PD analyses of large deformation problems. The objective of this thesis is to propose an implicit non-ordinary state-based peridynamics (NOSB PD) approach focusing on quasi-static analyses with large deformation mechanics. Firstly, the use of the adaptive dynamic relaxation (ADR) method as a solution strategy for quasi-static analyses with large deformation mechanics is discussed. Next, an analytical expression of the Jacobian matrix based on the equation of motion of NOSB PD is formulated to ensure optimum convergence of the global residual force. To address some instability issues in the existing "corresponding material" model, caused by zero-energy modes instability, recent approaches proposed by Silling (2017) are used to control the spurious deformation modes. An additional stabilisation term with respect to displacement is included in the derivatives for Jacobian formulation. This allows a more accurate NOSB PD approach to model material behaviour where correspondence materials have previously failed due to instability. Finally, to validate the proposed methodology, several numerical examples of 2D damage problems model using a stabilised correspondence model are verified, and suggestions are made for future implementation. The novelty of this thesis lies in providing theoretical development and numerical implementation of an implicit non-linear NOSB PD focusing on quasi-static analyses with large deformation mechanics. Findings from this thesis will interest researchers working in numerical methods, along with those solving discontinuous solid mechanics problems.

Declaration

The work in this thesis is based on research carried out in the Sustainable Infrastructure Research Challenge, Department of Engineering, Durham University. No part of this report has been submitted elsewhere for any other degree or qualification and it is all my own work unless referenced to the contrary in the text. Parts of this work have been published or submitted for possible publication in the following:

Conferences

UKACM 2017 - Birmingham
Hashim, N.A. and Coombs, W.M. and Hattori, G. and Augarde, C.E. (2017). "An implicit implementation of non-ordinary state-based peridynamics". In Proceedings of the 25th UKACM Conference on Computational Mechanics Birmingham, UK.
https://www.researchgate.net/publication/318108816

IWCMM28 - Glasgow
Hashim, A. and Coombs, W.M. and Hattori, G. and Augarde, C.E. (2018). "Comparison of implicit and explicit method for non-ordinary state-based peridynamics for quasi-static problems". 28th IWCMM28 Glasgow, UK.
https://www.peridynamics.org/past-events/2018/9/10/iwcmm28

UKACM 2019 - London
Hashim, Nur A. and Coombs, W.M. and Hattori, G. and Augarde, C.E. (2019) "An implicit non-ordinary state-based peridynamics for large deformation analysis". UKACM 2019 London, UK.
https://www.researchgate.net/publication/337077336

Journal Articles

Hashim, N.A., Coombs, W.M., Augarde, C.E.,Hattori, G.(2020). "An implicit non-ordinary state-based peridynamics with stabilised correspondence material model for finite deformation analysis". Computer Methods in Applied Mechanics and Engineering, 371 (2020): 113304.

Acknowledgements

First and foremost, all praise to God for his showers of blessing throughout my research work. I wish to thank the Ministry of Higher Education Malaysia and University Malaysia Perlis for their financial support, for which I am very grateful.

I would like to express my deepest gratitude to Dr Will Coombs and Professor Charles Augarde for providing invaluable guidance and persistent help throughout the entirety of this PhD. I humbly extend my thank to Dr Gabriel Hattori for his great help and guidance. Without their immense knowledge and advice, this work would not have been possible.

I would like to extend thanks to my family, especially my parents, for their love and sacrifices through tough times of completing this PhD work. Without their support, I would not be where I am today. I am extremely grateful to my husband for continuing support and love throughout the years. To my lovely son Haryz, thank you for your love and understanding. Also, I am thankful to my friends, colleagues, and the Malaysian community in Durham, past and present, for friendship and support. I would also like to give a special thanks to my sister and brother for their passionate encouragement and support.

Contents

List of Figures

List of Tables

Nomenclature

Abrreviation

$ndof$	Number of degrees of freedom
ADR	Adaptive Dynamic Relaxation
BB PD	Bond-based PeriDynamics
BC	Boundary Condition
DEM	Discrete Element Method
FEM	Finite Element Method
MM	Meshless Methods
NOSB PD	Non-ordinary State-based PeriDynamics
NR	Newton-Raphson
OSB PD	Ordinary State-based PeriDynamics
PD	PeriDynamics
PMB	Prototype Microelastic Brittle
SB PD	State-based PeriDynamics
SPH	Smooth Particle Hydrodynamics
XFEM	eXtended Finite Element Method

Scalar

Δx	Particle spacing
δ	Horizon

Δt	Time step
Δt_{cr}	Allowable time step size
ρ	Mass density
J	Volumetric ratio
t	Time
μ	History-dependent scalar valued function
ν	Poisson ratio
ω	Weight function
$\overline{\omega}$	Modified weight function
ϕ	Elevation angle
ρ	Mass density
σ^1	Maximum principal stress
σ^3	Minimum principal stress
τ	Maximum shear stress
τ_{cr}	Critical shear stress
R_d	Dirichlet boundary layer
R_t	Neumann boundary layer
cd	Damping coefficient
c'	dilatational wave speed
ft	Uniaxial tensile strength
g	Scalar-valued function
I_n	Total number of particles
k’	Bulk modulus
θ	Azimuthal angle
ε^d	Bond strain

ε^{d}_{max}	Critical bond strain
φ	Damage index
bc	Bond constant
C	Cohesive strength
c	Constant micromodulus
d	Damage criteria value
d_0	Depth
d_c	Critical damage criteria value
E	Young's Modulus
E'_{IJ}	Averaged deviatoric strain tensor
E_{eq}	Equivalent strain
E_{vol}	Volumetric strain
f	Internal frictional angle
G_0	Energy
h	Thickness
L	Length
R	Circular neighbourhood
s	Stretch
s_{cr}	Critical stretch value
V	Volume
w_0	Critical energy density
w_{xi}	Bond energy density
G	Stabilisation parameter
n_{NRit}	Number of NR iterations

Vector

$\boldsymbol{\eta}$	Relative displacement
$\boldsymbol{\sigma}$	Cauchy stress
$\boldsymbol{\xi}$	Relative position
$\ddot{\mathbf{u}}$	Second-order derivatives of displacement
$\dot{\mathbf{u}}$	Velocity vector
$\mathbf{b}$	Body force density
$\mathbf{f}^{ext}$	External force
$\mathbf{f}^{int}$	Internal force
$\mathbf{f}^{oobf}$	Global residual
$\mathbf{L}$	Internal force vector
$\bar{\mathbf{u}}$	Stabilised displacement field
$\underline{\mathbf{Y}}$	Deformation vector state
$\underline{\mathbf{Y}}_{\mathrm{z}}$	New deformation vector-state
$\mathbf{f}$	Pairwise force function
$\mathbf{u}$	Displacement vector
$\mathbf{x}$	Position vector of the particle
$\underline{\mathbf{T}}$	Force vector-state

Matrix

$\boldsymbol{\epsilon}$	Logarithmic elastic strain
$\boldsymbol{\Lambda}$	Diagonal density matrix
$\boldsymbol{\tau}$	Kirchhoff stress
$\mathbf{A}$	Material tangent modulus
$\mathbf{D_e}$	Elastic stiffness
$\mathbf{F}$	Deformation gradient
$\mathbf{K}$	Jacobian matrix

$\mathbf{K}$	Spatial tangent stiffness matrix
$\mathbf{K}^n$	Diagonal stiffness matrix
$\mathbf{M}$	Spatial tangent stiffness matrix
$\mathbf{N}$	Derivative of the Cauchy-Green strain with respect to the deformation gradient
$\mathbf{Q}$	derivative of the Kirchhoff stress with respect to the elastic logarithmic strain tensor
$\underline{\mathbf{T}}_z$	Penalty force
$\mathbf{c}$	Elastic left Cauchy Green strain
$\mathbf{P}$	First Piola Kirchhoff stress

Tensor

$\mathbf{B}$	Shape tensor
$\mathbf{C}$	Right Cauchy-Green deformation tensor
$\mathbf{c}$	Left Cauchy-Green deformation tensor
$\mathbf{R}$	Orthogonal tensor
$\mathbf{U}$	Symmetric right stretch tensors
$\mathbf{V}$	Symmetric left stretch tensors

Others

$(.)'$	Associated to neighbour
∇	Divergence
$\otimes$	Dirac delta
x	Cross product

Chapter 1

Introduction

1.1 Overview

Various problems in solid mechanics involve the existing and spontaneous formation of discontinuities that may emerge in a body such as cracks. Over the past few decades, researchers from all over the world have proposed many numerical methods to model crack problems, ranging from the evaluation of stress intensities due to existing cracks to the modelling of complex crack propagation. However, despite the development of several numerical approaches for modelling crack initiation and prediction of its growth in materials, it is still considered as one of the most challenging problems in the case of classical continuum mechanics (CCM). Although powerful, the main difficulty within the realm of CCM lies in the formulation, where the classical theory is formulated using spatial partial differential equations (PDE). This introduces a limitation to the classical theory, as the stresses at the fracture surfaces are mathematically singular, spatial derivatives by definition, lose their meaning or are not valid in the presence of discontinuities [1].

The numerical method that has been most widely used in solid mechanics is the Finite Element Method (FEM). However, the method has a limitation of solving problems with continuous spatial variation; FEM is less accurate in the treatment of discontinuous problems which, if the discontinuity propagates, require continuous remeshing of the physical domain so that the mesh conforms with the discontinuities. This process leads to complexity in the computer programming and degradation of solution accuracy [2].

An alternative to the conventional numerical methods which has gained much interest are known as meshfree or meshless methods which do not rely on meshes for their numerical solution. These methods have attracted much attention in recent years, as the term "meshless" or "meshfree" indicates that a set of particles is used to eliminate the mesh and thus can eliminate the mesh distortion problem and enable the modelling of crack propagation in a straightforward manner [3]. Since a set of discretised particles can model a growing crack, the analysis can be simplified since the remeshing process can be avoided, and in addition it does not suffer from mesh distortion in large deformation analyses [3, 4].

Peridynamics (PD) is a meshfree method based on non-local continuum theory, which Silling [5] initially introduced as an approach to deal with material failure. It is a novel numerical method that has been developed in integral form and takes into account long-range interactions, making it well suited for fracture mechanics problems. The PD theory is a reformulation of the solid mechanics equations of motion, and the advantages are apparent as it uses spatial integral equations and does not require spatial derivatives to be determined at discontinuities. PD still employs displacement in its formulation, but the difference between PD theory and CCM is that PD utilises displacement without spatial derivatives. As a result, sharp corners and spontaneous fracture propagation can be modelled easily since the governing equation of PD is well-posed even on fracture surfaces. PD methods have advantages over the previously developed classical methods for the following reasons:

(i) PD has been attractive as the governing equation employs an integral form rather than a PDE. In PD, the equation of motion is reformulated from the differential forms of the classical governing equation. One of the features of PD that classical theory does not seem to have is that the governing equations of motion accept the existence of discontinuities within the domain. Thus, no exclusive techniques are needed to handle the case of particles located throughout the length of interfaces which enables proponents of PD to state, for instance, [5]: *"a potential advantage for solving practical problems in which these discon-*

tinuities form spontaneously or grow along trajectories not known in advance".

(ii) Damage and failure zones are presented naturally in PD formulation, as in the concept of bond failure (i.e. bond breakage) when a specific failure criterion is satisfied. For example, bond failure occurs when the stretch value exceeds the prescribed critical stretch value, and this allows removal of the bond interactions. The bond failure is then used as the fundamental unit of damage. No external crack growth criteria to guide the crack or specify its propagation behaviour is needed, therefore, as stated in [5]: *"the reformulated approach permits the solution of fracture problems using the same equations either on or off the crack surface or crack tip"*.

(iii) Numerous studies have attempted to demonstrate that PD is an extremely reliable formulation to model a wide range of fracture phenomena, including coalition of multiple cracks, crack evolution, crack branching and crack curving, areas where traditional FE-based methods struggle [6–9]. These fracture phenomena are autonomously generated in PD by a failure criterion.

(iv) PD is a non-local continuum theory, and this non-local character of PD prescribes that each particle interacts with its neighbours within a given distance. This non-local continuum theory introduces a characteristic length-scale of interaction into the continuum description; the latter is called the horizon, which allows consideration of different horizon sizes within the same domain. PD formulation allows multi-scale analysis involving intrinsic length scales which can be linked to macro-scale modelling and micro or nano scales, as in the statement from [10]: *"one is led to the conclusion that a continuum model that permits a finite length scale for force interactions could potentially be highly relevant to current trends in technology"*.

(v) In PD, the nature of the failure can be modelled spontaneously without computationally expensive remeshing techniques, and this primary feature manifests the potential of PD theory as a practical and encouraging method for analysing the continuous damage and failure of structures as mentioned in [11]: *"fracture*

> *is treated as a natural outcome of deformation that emerges according to the equations of motion and constitutive model".*

Since its inception in 2000 as an alternative method in handling discontinuities in solid mechanics, numerous advances have been made using PD methods, particularly in the last decade, including a non-ordinary state-based peridynamics (NOSB PD) method. With PDs unique capability in capturing failure, much of the research that has taken place has focused on crack growth modelling. In the context of NOSB PD, researchers have focused on the modification of the PD equation to remove the deformations induced by spurious zero-energy modes. It is also interesting to note that the majority of previous PD research has used explicit time-stepping formulations. Three further points that have gained less attention than they might otherwise have done are described below:

- The NOSB PD theory has several drawbacks, including the instability problem, which leads to spurious zero-energy modes. Recent contributions have included attempts to control these modes. Recently, Silling has introduced a stabilised "correspondence" material model which satisfies the stability condition. However, this stabilised correspondence material model has not been studied in the context of the elimination of zero-energy modes for large deformation or implicit NOSB PD.
- PD is chosen for its potential advantage to solve practical problems including large deformation problems with geometrically non-linear response, especially where the discontinuities occur. This requires constitutive relationships between the rate of stress and the rate of strain in the body. However, an incorrect formulation could lead to lack of convergence to equilibrium within each step and unable to converge towards large deformation solutions.
- It is interesting to note that the focus of the majority of previous PD research has used explicit time-stepping approaches. While some work has been done on implicit approaches to PD, it is limited to the development and numerical implementation of a small strain linearly elastic material model. Specifically,

to date, there has been no implementation of an implicit large deformation NOSB PD method to the author's knowledge.

1.2 Scope and Outline

This thesis attempts to focus on the theoretical derivation, numerical development and implementation of an implicit approach of NOSB PD for large deformation problems. Within this remit, one of the primary aims of the thesis is to demonstrate the capability of PD in handling large deformation problems. This thesis also extends the formulation to include the study of crack propagation problems. This thesis consists of the following chapters, which can be split into four main sections:

- The first section will deliver the related background details for the research. Furthermore, the basic principles of the PD which will then be expanded further throughout the thesis.

  Chapter 1 includes a general introduction of the thesis, including the motivation of research of the choices of PD, advantages of PD and scope and overview of the thesis.

- The second part of this thesis demonstrates the essential tools which will then be used in the remainder of the thesis:

  Chapter 2 initially covers a literature review of PD since its inception as well as other numerical methods being used to analyse fracture modelling. The fundamental explicit bond-based peridynamics (BB PD) formulations are then reviewed, including five different damage criteria, as a foundation for the next chapters. An explicit BB PD algorithm is described in detail. The chapter closes with a numerical example using BB PD formulation with explicit time integration.

  Chapter 3 is concerned with NOSB PD with explicit time integration. The chapter presents the necessary concept of NOSB PD, together with the NOSB PD formulation and numerical examples. An Adaptive Dynamic Relaxation (ADR) approach for PD is also proposed, allowing for the application of explicit time-stepping schemes to quasi-static analysis. An explicit NOSB PD implementation algorithm with and without ADR is given, leading to verification against some numerical examples. A framework for the NOSB PD analysis is extended to model damage without a pre-existing crack.

- The main part of this thesis is concerned with the development and implementation of NOSB PD with implicit time integration. Every chapter here will begin by expanding the principle outlined in the previous chapters, which will lead to an implicit NOSB PD method being developed. This approach is then certified using numerical examples with analytical solutions. Every algorithm, theoretical derivation, differentiation, numerical implementation, and calibration in every developed NOSB PD is explained in detail.

  Chapter 4 develops an implicit NOSB PD approach based on a numerically built tangent stiffness. It is shown through comparison with explicit NOSB PD that implicit time integration has significant advantages in terms of the shorter run-time. The run-time and error associated with the numerical examples with implicit time integration, over an explicit time integration are demonstrated.

  Chapter 5 presents an analytically constructed tangent stiffness in large deformation with quasi-static problem of an implicit NOSB PD. The computational simulation of the development of the NOSB PD Jacobian matrices with a constitutive correspondence material model for both the standard and stabilised versions [12] is given in this chapter. Finally, the chapter illustrates the method's capabilities, and the effect of changing the stabilisation parameters to the formulation accuracy will also be tested with varying horizon sizes and particle spacing.

  Chapter 6 provides further development of the proposed implicit method for modelling crack propagation. This section provides an implicit solution method for quasi-static crack propagation for the first time on NOSB PD. A damage model is proposed to ensure the optimum convergence of the global equilibrium equations together with the stabilised NOSB PD with an analytically constructed Jacobian matrix. The details of the pragmatic approach specifying a degradation function in the interaction of the bond are given, and the framework is verified with numerical examples.

- The last section of the thesis provides a conclusion.

  Chapter 7 summarises all the research work in this thesis. The final section in this thesis provides some recommendations as to future directions that have the potential to be explored.

A development of NOSB PD for large deformation with an implicit time integration scheme is the main contribution in this thesis. The construction of the Jacobian matrix based on the analytical expression of the equation of motion of NOSB PD is proposed (for the first time in the author's paper). Since NOSB PD suffers from zero-energy modes, an attempt to include modification of the correspondence material model in eliminating zero-energy modes is made, based on the introduction of an additional term added to the PD force. This new proposed implicit NOSB PD models large deformation problems with varying horizon sizes and particle spacing in different problems.

1.3 Notation

In the interest of compactness and clarification, the author demonstrates the majority of quantities throughout the thesis in both index and matrix/vector notation. All analyses in this study were coded and run in MATLAB 2015b software using an Intel Core i5, CPU @ 2.40 GHz unless otherwise specified. The author chose MATLAB for its advantages in easy to implement, modify and debug the computational codes spontaneously.

The run times stated in the numerical examples are the average times over three measurements. There was no emphasis on optimising specific algorithms or parallelisation for use in large problems, and for this reason, this thesis does not include clear speed comparisons.

Chapter 2

Peridynamics

Peridynamics (PD) is a relatively new development of continuum mechanics and has established itself as a promising computational method for application in solid mechanics involving the spontaneous formation of cracks or discontinuities. This chapter will include an overview of the computational methods for fracture modelling and developments in PD since its inception, in Section 2.1 and Section 2.2, respectively. The basic bond-based peridynamics (BB PD) formulations are introduced in Section 2.3 as a base for later chapters in this thesis, followed by different PD damage criteria available in the literature in Section 2.4. An example is used to demonstrate the BB PD formulation in Section 2.5, and finally, the last section of this chapter, Section 2.6 presents an observation of this whole chapter.

2.1 Numerical methods for fracture modelling

The numerical method that has been dominated the realm of computational analysis of structures and solid mechanics is the well-developed Finite Element Method (FEM). Despite its many successes, FEM has a limitation of solving problems with continuous spatial variation. FEM faces problems in the treatment of discontinuities problems where a crack can only propagate along the interface of elements which require continuous remeshing of the physical domain so that mesh conforms with the discontinuities. This process leads to additional complexity in computer programming, further increasing the computational cost and degrading the solution accuracy

[2, 13–15]. Besides, FEM can become impractical when a large number of remeshings is necessary to model large deformation. The arbitrary Lagrangian-Eulerian method is more effective in reducing the mesh distortion and reduce the remeshing overhead in terms of accuracy in FEM. However, it still cannot completely prevent remeshing, and the corresponding remaping of the state variables [16].

The extended finite element method (XFEM) has been introduced based on FEM as a way to model crack growth without remeshing during the crack propagating process [17–20]. It does this by introducing discontinuous enrichment functions to approximate the displacement. This means, the cracks can propagate independently from elements and the crack opening value can be obtained through the enrichment functions [21]. The capability of the XFEM to gain better convergence of curved cracks by using high order enrichment functions or elements were highlighted in [22, 23]. However, XFEM is a highly enrichment dependent method and proper modelling techniques are needed for capturing crack-tip singularities in fracture mechanics problems. The simulation of multiplied fractures with XFEM is also cumbersome due to the need for multiple jump enrichment functions on the elements that feature crack intersections to track the kinematics of crack opening, and the need to track all of the crack lines/surfaces using some method (such as level sets) [24, 25]. An alternative to finite element based techniques is to use meshfree or meshless methods. Recently, advances in the development and application of these techniques show they can be strong competitors to the FEM [26].

A growing crack can be modelled using a set of particles, and remeshing is avoided. One of the earliest meshless method (MM) that has been proposed is the Smooth Particle Hydrodynamics (SPH) method originating about forty years ago by Lucy [27]. In terms of discretisation, SPH is similar to PD however, in SPH the partial differential equations are transformed into an integral equation using interpolation functions [28] while PD completely removes partial differential operators by relying on integration. The idea of SPH is that particles have a spatial distance known as the smoothing length, over which a kernel function smoothes their properties. SPH has been used to model fracture [29, 30], however, SPH is not flexible enough to support crack branching and the significant drawbacks of SPH are that the shape of the kernel can affect results. SPH also suffers from a numerical problem called tensile instability that manifests itself as a bunching of particles and formation of artificial voids [31] and there are significant issues in modelling certain boundary conditions for solids.

The element-free Galerkin method (EFGM) [32] is a weak-form based MM that has been applied to solve static and dynamic crack problems in [26, 33, 34], where separate description of crack geometry is still necessary by using either lines (2D) or surfaces (3D). The level set method, which is normally used to describe evolving surfaces, was introduced into the EFGM to model crack geometry in [35–37].

Another example of particle-based numerical simulations is the Discrete Element Method (DEM) [38–41]. In DEM, particles represent a physical object and the interaction between particles is modelled using contact laws instead of a weak form. DEM has been used for the investigation of particle crushing [42–45]. However, unlike PD methods, this method is used for discrete modelling and fundamentally replaces a continuum by a discrete medium. DEM is closely related to molecular dynamics [46, 47] and was developed for materials that are comprised of particles, for example, soil and rocks. One of the fundamental characteristics of particle simulation is that every particle can interact with every other particle in principle, this means two parts of the body that were not in contact at the beginning can come into contact at the later time during the ongoing analysis.

The phase-field method, which has of late attracted interest, has the ability to predict spontaneous emergence and propagation of cracks with the added attraction of mathematical simplicity [48] and can be combined with any continuum method. The concept can be used to model cracks as interfaces of intact and broken material, and the crack phase-field describes the transition zone. The phase-field has been used for a large number of problems [49–51]. However, the calculation and the evolution of the phase-field during crack propagation increases the computational expense. The phase-field method is perhaps the key competitor to PD for fracture mechanics at present. However, in the phase-field method, the crack is considered as diffuse damage instead of a sharp discontinuity [52]. Another key disadvantage of the phase-field method is the link between the phase-field transition length and the mesh size. In comparison to these methods, the inspiration in PD development is that the fracture process is modelled naturally as the cracks initiate and propagate via bond breakage, leading to progressive failure. Therefore, PD can simulate any new crack behaviour and model complex fracture pattern without any modification.

2.2 Review of the peridynamics (PD) method

In the light of the inadequacies of classical local theory, PD theory was introduced by Silling [5] in 2000, as a non-local reformulation of the solid mechanics equations of motion to handle solid mechanics problems involving discontinuities. PD theory is relatively new and stands in contrast to the classical formulation as it uses spatial integral equations rather than differential equations as with conventional continuum analyses. The advantages of this approach are apparent as the governing equation is in an integral form and, since no spatial derivatives are required, it offers an advantage as a promising technique to be used when modelling spontaneously emerged discontinuities without special remedial or remeshing techniques [1, 53]. As a result, autonomous crack initiation, propagation and branching can be captured easily and naturally without any simplifying assumptions or other separate damage law, which is normally needed in other approaches [1]. The word peridynamics derived from the Greek word *peri* meaning near or surrounding and the Ancient Greek word *dunamis* referring to the force, alluding to the force exerted by surrounding particles [5, 54]. PD is a long-range (non-local) theory and can be captured as a transition from the classical local theory of continuum mechanics to molecular dynamics as demonstrated in Figure 2.1. Non-local continuum field theories in continuum mechanics have been proposed in [55–59] that consider the effects of finite distance interactions. Similar to non-local theories [55–59], the PD method employs displacement in its formulation but it differs from the classical continuum method in that PD utilises displacement without considering its spatial derivatives within the statement of equilibrium.

Peridynamics (PD) is a continuum theory, where interactions occur between particles representing a portion of the continuum which are separated by a finite distance. The change of state at a particle is influenced by the states of particles that are at some finite distance away [60]. As illustrated in Figure 2.1, in the local continuum model, the interactions of particle **x** is limited to the nearest neighbour particles, located in its immediate proximity. In contrast, in PD, the state of a particle is influenced by particles located within a region of the finite radius or particle's "horizon" denoted by δ. For example, the value of force at a particle is influenced directly by the values of the field in the neighbourhood of that particle. With the region of finite radius close to infinity, the theory can be thought of as the continuous version of the molecular dynamics model. Conversely, as the horizon approaches zero, PD theory converges to local classical continuum mechanics [10, 61, 62]. However, naturally, one would use PD models for problems that are difficult or impossible to solve using the CCM and not for problems for which classical models already provide satisfactory results [63].

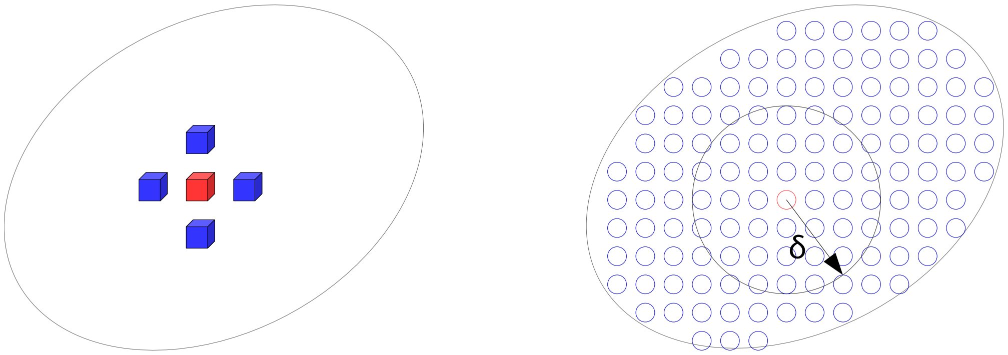

(a) Local continuum model (b) Non-local continuum model

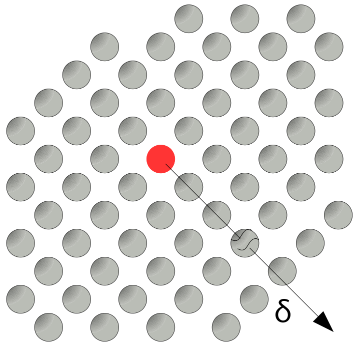

(c) Molecular dynamics

Figure 2.1: Graphic representation of: (a) local continuum models, (b) non-local continuum models and (c) molecular dynamics (reproduced from [1])

2.2.1 Bond-based peridynamics (BB PD)

Bond-based peridynamics (BB PD) is the original version of PD formulation developed by Silling in 2000 where the interactions between particles act like spring forces and only depend on the relative position and relative displacement of the interacting particle pairs [5]. This means that the connection of two particles is insensitive to the states of other particles. One of the earliest paper that employed the BB PD, written by Silling and Askari [53], presented the numerical simulation of a predicted crack tip growth with the variations in particle spacing. The damage contours due to the impact of a sphere on a brittle solid were also investigated. However, the BB PD scheme is restricted to constitutive models with fixed Poisson's ratios: ν of $1/4$ for plane strain and 3D problems and $1/3$ for plane stress conditions [64]. Another drawback to this BB PD model is the requirement to completely recast the constitutive behaviour of a material in terms of a pairwise force function when traditionally material behaviour has been formulated in terms of a stress tensor [65]. As a consequence, although plasticity can be included in the bond-based theory by permitting permanent deformation of individual bonds, plastic incompressibility condition cannot be captured directly with the BB PD [66] because the materials are undergoing volumetric strain without shear [65]. In order to remove the constraint on Poisson's ratio, Gerstle *et al.* [64] proposed a specific constitutive micropolar peridynamics model by considering not only pairwise forces but also the pairwise moments in the BB PD formulation. This overcomes the limitation in the original BB PD for isotropic linear elastic materials by allowing the simulation of Poisson's ratios between -1 and ∞. Since BB PD is comparatively simple to be implemented, BB PD formulation method has been employed to study a variety of mechanical systems and applied to investigate some solid fracture problems. For example, fracture analysis of plain and reinforced concrete structures has been studied by Gerstle *et al.* [64, 67–69] and fracture in rubbery sheets by Silling [11]. On the other hand, Dayal and Bhattacharya [70] studied the kinetics of phase transformations using BB PD formulation. The BB PD model has also been applied to the simulation of dynamic fracture in the materials [63, 71–73]. It was seen that the dynamic crack propagation phenomenon is well captured and the crack propagation speed is unaffected by the size of the non-local interaction. It is also shown in [63] that the location of crack branching is independent of the horizon size. However, it was also shown in [74] that the crack propagation speed depends on the horizon size. Ha and Bobaru [74] investigate the characteristics of dynamic brittle crack propagation branching, and it was identified that the fracture phenomenon is very sensitive due to the effects of impurities and material inhomogeneities. A further extension of the BB PD was made by Huang *et al.* [6, 75] through the introduction of local damping into the PD equation of motion where it was concluded that the magnitude of the local damping does not influence the accuracy. However, it does affect the convergence rate [75]. Recently PD has been employed for damage analysis in isotropic solids which includes quasi-static failure [64, 76, 77]. Liu and Hong have proposed another attempt [78] to remove the restriction on Poisson's ratio by introducing a force compensation scheme adding additional forces on each pairwise force between particles. However, errors are seen to increase in the results of strain as the horizon increases [78]. Throughout its development, the BB PD has been successfully used in a wide range of application including the dynamic fracture of homogeneous and heterogeneous bars [79], failure of concrete structures [64, 80–82], composites [11, 53], composite laminates [83–86] and crack branching [74]. The BB PD formulation has also been used to model fracture of polycrystals [87], quenched glass [81] and impact damage [53, 88–91]. In addition, coupling between the BB PD model and classical continuum models has been performed in [10, 85, 92–96] for multi-scale failure analysis. An important extension of BB PD, the non-ordinary state-based peridynamics (NOSB PD) formulation introduced by Silling *et al.* in [66], is a generalisation of the BB PD framework and is the subject of the next section.

2.2.2 Non-ordinary state-based peridynamics (NOSB PD) method

PD formulations can be categorised into BB PD and state-based peridynamics (SB PD) [66, 97]. SB PD allows the response of a given particle to depend on the collective deformation of all bonds that are within a finite distance. SB PD formulations can be further classified as ordinary state-based peridynamics (OSB PD) and non-ordinary state-based peridynamics (NOSB PD) depending on the modelling of the force term. In the BB PD, the forces, $\mathbf{f}$, between two particles ($\mathbf{x}$ and $\mathbf{x}'$) always have equal magnitude and opposite directions, thus conserving linear and angular momentum. On the other hand, in the OSB PD formulation, the forces in the bonds, $\underline{\mathbf{T}}$ and $\underline{\mathbf{T}}'$ defined as the force-vector states, are aligned in the direction of the bonds, as in the bond-based approach but can have different magnitudes [98–107]. The conservation of angular momentum is satisfied in the OSB PD formulation, whereas in the NOSB PD formulation, the force states place no restriction on the magnitude or direction of the forces [66]. These differences are illustrated in Figure 2.2. The force densities, $\mathbf{t}$ and $\mathbf{t}'$ are expressed as

$$\mathbf{t} = \underline{\mathbf{T}}(\mathbf{x})\langle \mathbf{x}' - \mathbf{x} \rangle \quad \text{and} \quad \mathbf{t}' = \underline{\mathbf{T}}(\mathbf{x}')\langle \mathbf{x} - \mathbf{x}' \rangle, \tag{2.1}$$

extracted by the force states operating on the corresponding relative position vectors. The NOSB PD is conceptually more challenging to implement compared to the

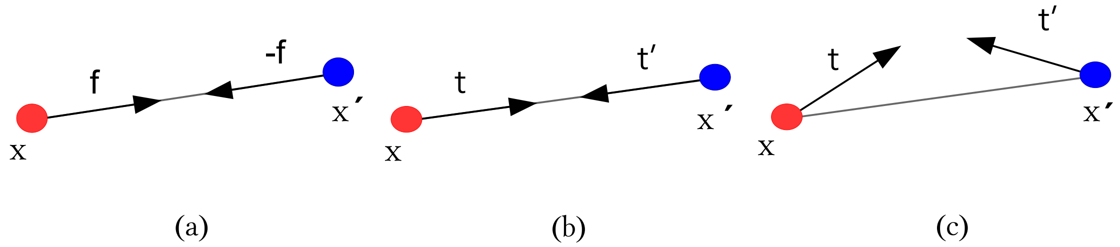

(a) (b) (c)

Figure 2.2: Illustration of the tractions in the PD bonds in (a) BB PD, (b) OSB PD and (c) NOSB PD.

BB PD. Nevertheless, it eliminates the restriction of fixed Poisson's ratios, enabling the modelling of more complex materials. The particle interactions are characterised in terms of force state rather than pairwise force functions [65, 108] due to the collective deformation of all bonds that are within the particle's domain. The NOSB PD approach leads to more realistic simulations as the forces in the bonds are arrived at by considering the stress and the deformation fields at each of the particles, which allows for modelling using general constitutive models as in [7, 53, 77, 108–124]. Numerous developments have been made using NOSB PD methods in the past few years, including a NOSB PD modelling procedure by Warren *et al* for analysing small strain crack propagation under quasi-static loading [108]. Based on a NOSB PD formulation, Foster [65] proposed the simulation of explicit dynamic impact tests of aluminium. The NOSB PD formulation was also used to model and investigate dynamic crack growth in an elastic-viscoplastic crystal [125] and thermo-visco-plastic deformation [126]. Fracture modelling was the focus of early research in PD, utilising simple constitutive models, as stated in [54]. NOSB PD, as a nonlocal meshless method, is not limited in the amount of deformation since there are no mesh regularity constraints to consider. However, the application of PD methods to large deformation problems has been relatively unexplored in the literature. With its unique capability in capturing failure, it can simulate crack propagation and damage processes including those in rock-like materials [127], thermoplastic fracture [113] and in anisotropic materials [117]. The PD method has also been widely used to solve quasi-static problems [75, 76, 108, 119, 128–131]. However, it is interesting to highlight that the majority of previous PD research has used explicit time-stepping formulations, and a drawback arises from the limitation on the time step size to ensure numerical stability. In the case of quasi-static loading, it becomes expensive to obtain solutions. This implies that it limits the critical, allowable time step size Δt_{cr}, which should not be exceeded in the analysis. The overall method efficiency is, therefore, dependent on the size of the critical time step. Two of the rare examples of non-explicit methods are as follows. An implicit NOSB PD formulation was presented in [77] for linearly elastic solids implemented within Emu, a PD code in development at Sandia National Laboratories, and another implicit implementation of NOSB PD was presented in [129] for crystal plasticity problems. However, the work in [77] was limited to the development and numerical implementation of a small strain linearly elastic model whereas, in reference [129], the computation of the tangent modulus was based on the crystal plasticity constitutive model. Since PD is a nonlocal theory, the construction of tangent stiffness in quasi-static or implicit dynamics analysis has less sparsity compared to the traditional finite element. Therefore Brothers *et al.* [130] compare the different methods used for calculating tangent-stiffness matrices using Peridigm software, open source PD software code developed by Sandia National Laboratory [132]. Based on the computational analyses that were done in [130], it can be concluded that for users of Peridigm, automatic differentiation was shown to have an advantage in terms of speed. Automatic differentiation is a computerised method for computing exact derivatives based on the chain-rule [133].

Zero-energy modes

NOSB PD allows a material model from standard local theory to model long-range forces with the inherent capabilities of a nonlocal PD formulation. However, in a uniform particle discretisation, the method suffers from instability due to zero-energy modes, as previously identified in the mathematical formulation of the PD theory [12, 77, 111, 115, 116, 118, 134–139]. In the presence of zero-energy modes, simulations exhibit oscillations in the deformation and stress fields. Zero-energy modes have been overcome in the classical Finite Element Method (FEM) by inserting artificial stiffness to increase stability [140]. In NOSB PD, these modes are caused by the missing role of the centre particle when approximating the deformation gradient tensor, and all correspondence materials fail this stability condition [12]. The presence of zero-energy modes affects the deformation, and therefore, various methods have been proposed in order to alleviate this problem. Breitenfeld *et al.* [77] introduced two methods to deal with this problem using supplementary forces. The first approach introduces an additional term as a function of relative displacement between particles in the bond whereas, in the second approach, the additional force state arising is calculated based on the average of the relative displacement states of all the particles in its horizon. However, these approaches require a penalty constant, and if the penalty value is too large, the supplementary force will dominate the solution [77] and thus lead to lower accuracy. Littlewood [125] developed an additional force term based on a penalty approach, where the penalty force was proportional to the difference between the actual and predicted deformed position of the particles and tends to drive particles toward smooth deformations. However, as with the previous approaches, if the penalty value is too large, the supplementary force will dominate the solution [77] and thus lead to lower accuracy. Littlewood [125] and Breitenfeld *et al.* [77] provided different forms of an additional term which contributes to the PD force vector-state, which represents the supplemental bond between particles. A stabilised displacement field approach introduced by Wu and Ren [111] eliminated the requirement of the coefficient calculation for the supplementary force in modelling the metal ductile failure. However, the oscillation problem still exists in the strain and stress fields [111], and it was shown that the damage contour is affected by the size of the horizon. These three methods show sensitivity to the discretisation scheme, and therefore, an optimum value of the spring coefficient in the supplementary force needs to be adjusted based on the discretisation scheme such as particle's spacing and nonlocal horizon size for each problem [77, 111, 125]. At the same time, Yaghoobi and Chorzepa proposed calculation of the deformation gradient based on higher-order polynomial approximation which is viable in enhancing the accuracy of the method with larger horizons [115]. Recently, Silling has introduced a stabilised "correspondence" material model which satisfies the stability condition [12]. Here an attempt has been made by Silling to eliminate the zero-energy modes by adding a term to the corresponding strain energy density [12], considering the root of the problem as a material rather than a numerical instability. This stabilised correspondence material model has not been studied in the context of the elimination of zero-energy modes for large deformation or implicit NOSB PD. In the literature, further approaches to control the zero-energy mode have been suggested [116, 118], which are generalisations of [12].

Imposition of boundary condition

The imposition of essential boundary conditions (BC) in PD is somewhat different than in the classical continuum theory. Since the PD equations of motion utilise integral equations, boundary conditions in PD are imposed over volumes. In this section, the available methods on how to imposed Dirichlet and Neumann boundary condition in PD are described. As a nonlocal theory, within which the integral form of the governing equation is evaluated in the nonlocal boundary region, the nonlocal Dirichlet boundary conditions in PD are imposed through a nonzero volume of fictitious boundary layers. As explained in [141], and based on the numerical experiments in [92], the extent of the nonzero volume of fictitious boundary layer, R_d, as illustrated in Figure 2.3 is suggested. The fictitious boundary layer is equivalent to the size of the horizon used, as proposed by Macek and Silling [92]. Displacement or rotation boundary conditions are imposed by assigning constraints to the particles in the fictitious surface layer of particles. This method is proposed to ensure that the imposed prescribed constraints are precisely reflected within the real material domain. The same method has been applied in [142, 143] for beam problems. An external load can be applied in the form of body force through a layer within the surface layer of the actual region, R_t as shown in Figure 2.3 [141]. The size of this layer is equivalent to the size of the particle spacing, Δx.

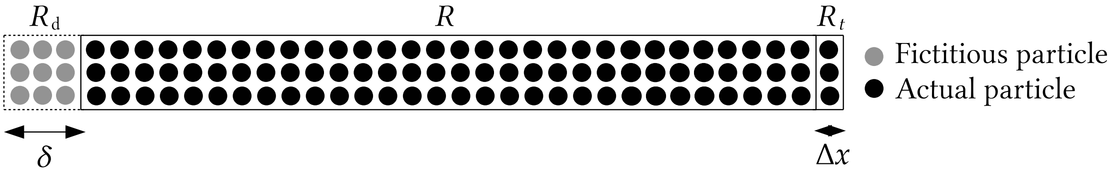

Figure 2.3: Application of boundary conditions in a peridynamics (PD) beam.

2.3 Bond-based peridynamics (BB PD) numerical implementation

At the beginning of a PD analysis, it is necessary to define the problem domain and divide it into a finite number of subdomains. The particles are placed at the centre of each subdomain, associated with a specific volume and the initial particle positions. In regard to choosing particle discretisation, it is not restricted to any particular discretisation arrangement. However, it is desirable for it to be of regular uniform spatial discretisation as this simplifies identifying the initial location and how much volume should be associated with each particle. The volume stays with the particle throughout the simulation, and each particle has its particular family members. In addition, the information of each particle family members (nearest-neighbour) needs to be stored.

In classical continuum mechanics, the equation of motion of any particle $\mathbf{x}$ derived from the conservation of linear momentum can be expressed as [144]

$$\rho(\mathbf{x})\ddot{\mathbf{u}}(\mathbf{x},t) = \nabla\boldsymbol{\sigma} + \mathbf{b}(\mathbf{x},t), \tag{2.2}$$

in which ρ represents the mass density in the deformed configuration at the particle $\mathbf{x}$ and $\ddot{\mathbf{u}}$ denotes the second-order derivatives of displacement $\mathbf{u}$ with respect to time. ∇ denotes the divergence of the Cauchy stress, $\boldsymbol{\sigma}$ and $\mathbf{b}$ is prescribed body force density field at time t. However, in Eq. (2.2), those spatial derivatives becomes undefined along discontinuities. In contrast, the original PD formulation uses an integral function of a force on a particle at $\mathbf{x}$ in the deformed configuration at time t to replace the divergence of stress term, written as [5]

$$\rho(\mathbf{x})\ddot{\mathbf{u}}(\mathbf{x},t) = \mathbf{L}(\mathbf{x}) + \mathbf{b}(\mathbf{x},t), \tag{2.3}$$

and

$$\mathbf{L}(\mathbf{x}_i) = \int_R \mathbf{f}[\mathbf{u}(\mathbf{x}',t) - \mathbf{u}(\mathbf{x},t), \mathbf{x}' - \mathbf{x}]dV_{\mathbf{x}'}. \tag{2.4}$$

$\mathbf{f}$ is the pairwise PD force function that the particle $\mathbf{x}'$ exerts on $\mathbf{x}$ with units of force per unit area, $V_{\mathbf{x}'}$ is the volume associated with particle $\mathbf{x}'$ and the integral is defined over a circular neighbourhood, R, of given radius, δ, centered at particle $\mathbf{x}$, as shown in Figure 2.4. This equation can be applied everywhere in the body, so no special assumptions are needed to deal with singularities using PD.

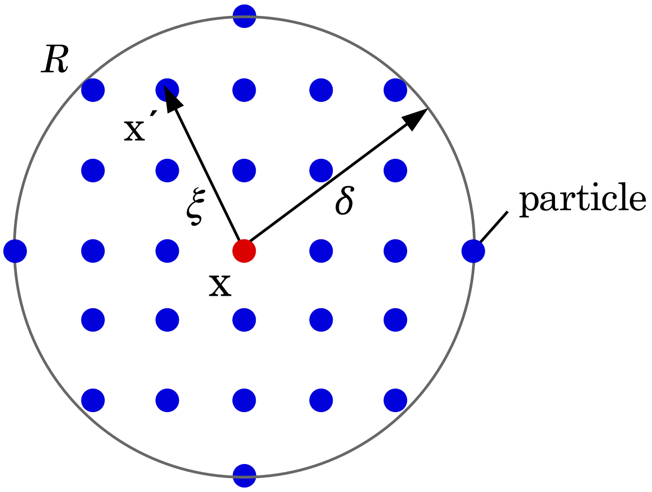

Figure 2.4: Particle $\mathbf{x}$ interacts with particle $\mathbf{x}'$ within a specified circular neighbourhood, R of radius δ, where ξ is the vector that links particle x with any particle in its horizon, x'.

The relative position vector of two particles is denoted by $\boldsymbol{\xi}$, such that

$$\boldsymbol{\xi} = \mathbf{x}' - \mathbf{x}. \tag{2.5}$$

It is assumed that the particles' displacements are respectively given by $\mathbf{u}$ and $\mathbf{u}'$, and the relative displacement vector $\boldsymbol{\eta}$ is given by

$$\boldsymbol{\eta} = \mathbf{u}'(\mathbf{x}', t) - \mathbf{u}(\mathbf{x}, t). \tag{2.6}$$

The relationship among the variables illustrated in Figure 2.5 where $||\boldsymbol{\xi}||$ and $||\boldsymbol{\xi}+\boldsymbol{\eta}||$ are the Euclidean norms of $\boldsymbol{\xi}$ and $\boldsymbol{\xi}+\boldsymbol{\eta}$, representing the initial and deformed bond length, respectively, between particle $\mathbf{x}$ and $\mathbf{x}'$. The integral term in Eq. (2.4) can be interpreted as the force per unit volume squared and after discretisation, the equation of motion is written as

$$\rho\ddot{\mathbf{u}}(\mathbf{x}, t) = \sum_{j=1}^{m} \mathbf{f}(\boldsymbol{\eta}, \boldsymbol{\xi})V_j + \mathbf{b}(\mathbf{x}, t), \quad \forall \mathbf{x} \in \Omega. \tag{2.7}$$

where j is a counter for the m particles in the horizon of particle i in the domain Ω and V_j is the volume of particle j in the deformed configuration. Silling and Askari proposed a Prototype Microelastic Brittle (PMB) model for isotropic materials [53]

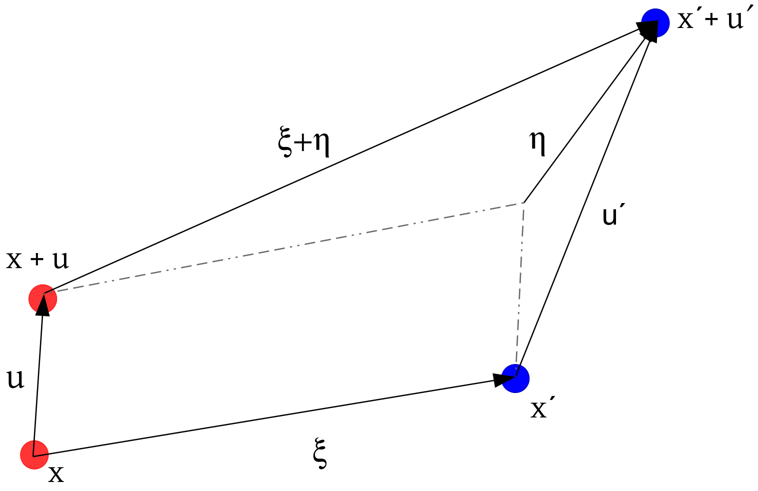

Figure 2.5: Reference, $\boldsymbol{\xi}$ and deformed, $\boldsymbol{\xi}+\boldsymbol{\eta}$ vector states.

where the pairwise force function depends only on the stretch between particles $\mathbf{x}$ and $\mathbf{x}'$, defined as [53]

$$\mathbf{f}(\boldsymbol{\eta},\boldsymbol{\xi}) = f(\boldsymbol{\eta},\boldsymbol{\xi})\frac{\boldsymbol{\eta}+\boldsymbol{\xi}}{\|\boldsymbol{\eta}+\boldsymbol{\xi}\|}. \tag{2.8}$$

A scalar δ is the radius assumed for each particle known as the horizon to determine the interacting range between the particles such that

$$\mathbf{f}(\boldsymbol{\eta},\boldsymbol{\xi}) = 0 \quad \text{if } \|\boldsymbol{\xi}\| > \delta. \tag{2.9}$$

Restricted to Newton's Third Law, the force function in Eq. (2.4) must satisfy the *linear admissibility condition* as stated in [5, 145], which assures the conservation of linear momentum. Therefore, Eq. (2.10) will be called the *linear admissibility condition* on $\mathbf{f}$. Newton's Third Law states that the force at particle $\mathbf{x}$ due to a particle at $\mathbf{x}'$ must be equal but opposite in direction to the force at particle $\mathbf{x}'$ due to a particle at $\mathbf{x}$. Therefore, Eq. (2.4) must satisfy

$$\mathbf{f}(-\boldsymbol{\eta},-\boldsymbol{\xi}) = -\mathbf{f}(\boldsymbol{\eta},\boldsymbol{\xi}). \tag{2.10}$$

In order to satisfy above mentioned assumption for the force function, each bond must be individual and not affected by the other bonds. Another restriction arises from the conservation of angular momentum, which states that the particles will only move with the presence of external forces, satisfying that

$$(\boldsymbol{\eta} + \boldsymbol{\xi}) \times \mathbf{f}(\boldsymbol{\eta}, \boldsymbol{\xi}) = 0, \tag{2.11}$$

where "×" is the cross product, and cross product of any parallel vectors equals to zero. Thus Eq. (2.11) indicates that the force between any two particles must be parallel to their relative deformation pairwise force function. The bond force, which is a scalar function, is

$$f(\boldsymbol{\eta}, \boldsymbol{\xi}) = cs(t, \boldsymbol{\eta}, \boldsymbol{\xi})\mu(t, \boldsymbol{\eta}, \boldsymbol{\xi}), \tag{2.12}$$

where s is the stretch in the bond

$$s(t, \boldsymbol{\eta}, \boldsymbol{\xi}) = \frac{\|\boldsymbol{\eta} + \boldsymbol{\xi}\| - \|\boldsymbol{\xi}\|}{\|\boldsymbol{\xi}\|}, \tag{2.13}$$

and c is the constant micromodulus. For an isotropic material, c can be determined by considering an infinite homogeneous body under isotropic expansion [53] in which case for 3D structures, it is given by

$$c = \frac{18k'}{\pi\delta^4}, \tag{2.14}$$

and for 2D problems, it is

$$c = \frac{12k'}{\pi h\delta^3}, \tag{2.15}$$

in which k' is

$$k' = \begin{cases} \frac{E}{2(1-\nu)} & \text{plane stress} \\ \frac{E}{2(1-\nu-2\nu^2)} & \text{plane strain.} \end{cases} \tag{2.16}$$

$\mu(t, \boldsymbol{\eta}, \boldsymbol{\xi})$ is a history-dependent scalar valued function, which controls the level of damage in the bond. This parameter will be discussed in more detail in Section 2.4. The following time integration can be used to obtain value of displacement, velocity and acceleration. Acceleration, $\ddot{\mathbf{u}}$ can be obtained by using this explicit simple equation given by

$$\ddot{\mathbf{u}}(\mathbf{x}, t) = \frac{\mathbf{L}(\mathbf{x}) + \mathbf{b}(\mathbf{x}, t)}{\rho}. \tag{2.17}$$

Thus, as suggested in [108], the acceleration can be calculated directly from Eq. (2.3). Using Eq. (2.17), velocities, $\dot{\mathbf{u}}$ are obtained through a forward difference scheme

$$\dot{\mathbf{u}}(\mathbf{x}, t + \Delta t) = \dot{\mathbf{u}}(\mathbf{x}, t) + \ddot{\mathbf{u}}(\mathbf{x}, t)\Delta t, \tag{2.18}$$

while the displacement, $\mathbf{u}$ is integrated with a backward difference approach as

$$\mathbf{u}(\mathbf{x}, t + \Delta t) = \mathbf{u}(\mathbf{x}, t) + \dot{\mathbf{u}}(\mathbf{x}, t + \Delta t)\Delta t. \tag{2.19}$$

The algorithm of explicit NOSB PD code implementation is presented in Figure 3.4.

lstp	1	2	$lstp_n$	FOR EACH Loadstep		
i	1	2	I_n	FOR EACH Particle		
j	1	2	$....m$	FOR EACH Neighbouring Particle		
$\boldsymbol{\xi}$				relative position	$\boldsymbol{\xi} = \mathbf{x}_j - \mathbf{x}_i$	(2.5)
$\boldsymbol{\eta}$				relative displacement	$\boldsymbol{\eta} = \mathbf{u}(\mathbf{x}_j, t) - \mathbf{u}(\mathbf{x}_i, t)$	(2.6)
s				bond stretch	$s(t, \boldsymbol{\eta}, \boldsymbol{\xi}) = \frac{\lVert\boldsymbol{\eta}+\boldsymbol{\xi}\rVert - \lVert\boldsymbol{\xi}\rVert}{\lVert\boldsymbol{\xi}\rVert}$	(2.13)
c				constant micromodulus	$c = \frac{12k'}{\pi h \delta^3}$	(2.15)
μ				history-dependent scalar valued function	$\mu(t, \boldsymbol{\eta}, \boldsymbol{\xi}) = \begin{cases} 1 & \text{if } d < d_c \\ 0 & \text{otherwise} \end{cases}$	(2.20)
f				bond force	$f(\boldsymbol{\eta}, \boldsymbol{\xi}) = cs(t, \boldsymbol{\eta}, \boldsymbol{\xi})\mu(t, \boldsymbol{\eta}, \boldsymbol{\xi})$	(2.12)
$\mathbf{f}$				pairwise force function	$\mathbf{f}(\boldsymbol{\eta}, \boldsymbol{\xi}) = f\,\frac{\boldsymbol{\eta}+\boldsymbol{\xi}}{\lVert\boldsymbol{\eta}+\boldsymbol{\xi}\rVert}$	(2.8)
				END FOR		
$\mathbf{L}$				summation of pairwise force function	$\mathbf{L}(\mathbf{x}_i) = \sum_{j=1}^{m} \mathbf{f}(\boldsymbol{\eta}, \boldsymbol{\xi}) V_j$	(2.4)
$\ddot{\mathbf{u}}$				acceleration	$\ddot{\mathbf{u}}(\mathbf{x}_i, t) = \mathbf{L}(\mathbf{x}_i) + \mathbf{b}(\mathbf{x}_i)/\rho(\mathbf{x}_i)$	(2.17)
$\dot{\mathbf{u}}$				velocity	$\dot{\mathbf{u}}(\mathbf{x}_i, t+\Delta t) = \dot{\mathbf{u}}(\mathbf{x}_i, t) + \ddot{\mathbf{u}}(\mathbf{x}_i, t)\Delta t$	(2.18)
$\mathbf{u}$				displacement	$\mathbf{u}(\mathbf{x}_i, t+\Delta t) = \mathbf{u}(\mathbf{x}_i, t) + \dot{\mathbf{u}}(\mathbf{x}_i, t+\Delta t)\Delta t$	(2.19)
				END FOR		

Figure 2.6: Bond-based peridynamics (BB PD) algorithm sequence for 2D problem where *lstp* denotes the loadstep, i denotes the particle number and j denotes the neighbouring particles.

2.4 Damage criteria

In PD, material damage is modelled through the elimination of interaction (bonds) among particles. Once broken bonds are eliminated, there is no force sustained in the bond and fracture is introduced through the failure of bonds. According to Silling *et al.* [53], no force can be sustained by the bond after its failure, which means it is failed forever. As a result, the load is redistributed among the remaining particles. In order to specify whether a bond interaction is active or terminated, a history-dependent scalar valued function, $\mu(t, \boldsymbol{\eta}, \boldsymbol{\xi})$ was introduced in [53] as

$$\mu(t, \boldsymbol{\eta}, \boldsymbol{\xi}) = \begin{cases} 1 & \text{if } d < d_c, \\ 0 & \text{otherwise.} \end{cases} \tag{2.20}$$

where d is the damage criteria value and d_c is the critical damage criteria value. Based on the function $\mu(t, \boldsymbol{\eta}, \boldsymbol{\xi})$, the damage index at a particle $\mathbf{x}$ can be quantified as [53]

$$\varphi(\mathbf{x}, t) = 1 - \frac{\int_R \mu(t, \boldsymbol{\eta}, \boldsymbol{\xi}) dV_{\mathbf{x}'}}{\int_R dV_{\mathbf{x}'}}. \tag{2.21}$$

The damage index ranges from 0 to 1. If the damage index of a particle is 0, all the interaction associated with the particle is intact while a damage index of 1 means that all the interactions associated with the particle have been eliminated [53]. Figure 2.7 (a) shows that a particle initially interacts with all particles in its horizon and thus, the damage index is zero. However, due to the creation of a fracture characterised by bond breakages, it is now assumed that half of the particle's interaction has been eliminated thus, resulting in a particle's damage index of 0.5, as shown in Figure 2.7 (b). PD damage criteria reflected in the equations of motion by removing the force density vectors between the particles by considering different damage criterion as critical bond stretch, deformation based failure, critical energy density, maximum principal stress and critical bond strain.

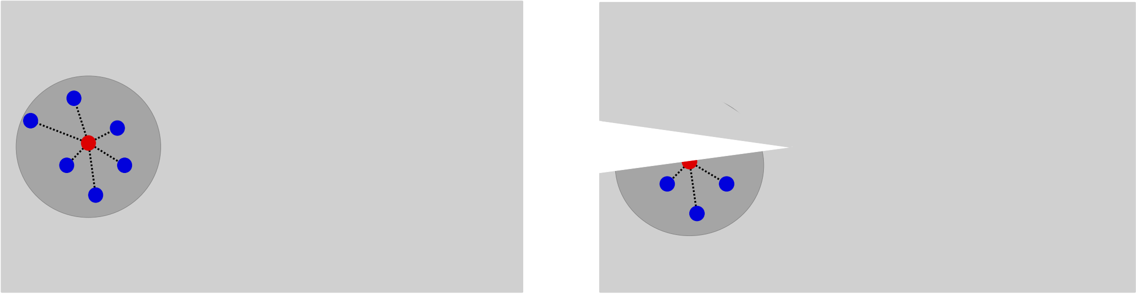

(a) (b)

Figure 2.7: Visualisation of the damage index: (a) all particle's interactions are intact and (b) half of the particle's interactions have been eliminated.

2.4.1 Critical bond stretch

The most basic damage criteria that are available in the literature are based on the critical bond stretch introduced in [53]. In terms of the critical bond stretch, it is assumed that when the bond between two particles, $\mathbf{x}$ and $\mathbf{x}'$ stretched in tension (or compression) and the stretch s, exceeds its critical stretch value, s_{cr}, bond breakage occurs. The stretch between particles $\mathbf{x}$ and $\mathbf{x}'$ is defined in (2.13). The work required to break a single bond is [53]

$$w_0\xi = \int_0^{s_{cr}} g(s)d\eta = \int_0^{s_{cr}} g(s)\xi ds, \quad \xi = ||\boldsymbol{\xi}||, \tag{2.22}$$

where g is a scalar-valued function given by $g(s) = cs$. The integration simplifies to

$$w_0(\xi) = \int_0^{s_{cr}} cs\xi ds = \frac{cs_c^2\xi}{2}. \tag{2.23}$$

Figure 2.8 shows the main variables used in (2.24). Therefore, the energy, G_0, required to break all the bonds per unit fracture area is

$$G_0 = \int_0^{\delta}\int_0^{2\pi}\int_z^{\delta}\int_0^{\cos^{-1} z/\xi} (\frac{cs_c^2\xi}{2})\xi^2 \sin\phi d\phi d\xi d\theta dz. \tag{2.24}$$

The integral shown in Eq. (2.24) represents the summation of the work required to break all the bonds connected to particle A and all of the particles B within its horizon, as shown in Figure 2.8. All particles along the dashed line $0 \leq z \leq \delta$ need to be considered and this yields to the first integral in Eq. (2.24). The second integral

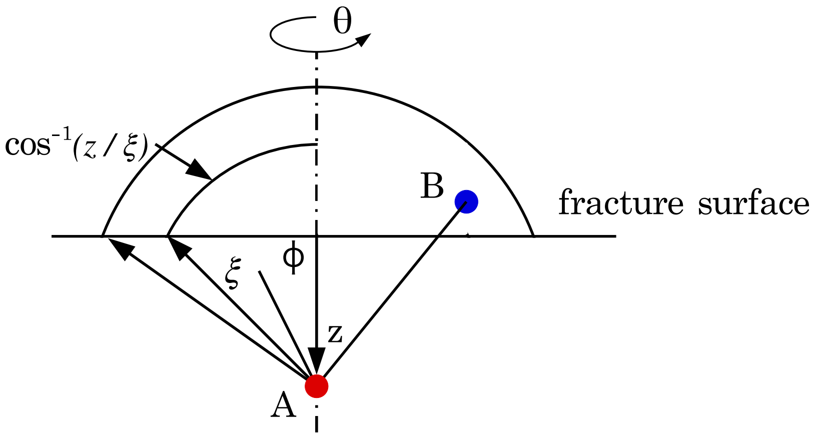

Figure 2.8: Evaluation of fracture energy (from Siling *et al.* [53]).

is the rotation with the azimuthal angle θ, the third integral along the dashed line, and the last integral along the circular segment with elevation angle ϕ. Solving Eq. (2.24) leads to

$$G_0 = \frac{\pi c s_c^2 \delta^5}{10}, \tag{2.25}$$

and rearranging (2.25) for critical bond stretch, s_{cr} leads to

$$s_{cr} = \sqrt{\frac{10 G_0}{\pi c \delta^5}}. \tag{2.26}$$

2.4.2 Deformation based failure

Warren *et al.* proposed two damage criteria using the classical definitions for the NOSB PD formulation since it incorporates classical continuum mechanics definitions [108]. The first criterion is based on the equivalent strain, $E_{eq}(\mathbf{x}, \mathbf{x}')$ obtained from the second invariant I_2' of the averaged deviatoric strain tensor $E'_{IJ} = E_{IJ}(\mathbf{x}, \mathbf{x}') - \frac{1}{3} E_{KK}(\mathbf{x}, \mathbf{x}')\delta_{IJ}$ and expressed as

$$\begin{aligned}E_{eq}(\mathbf{x},\mathbf{x}') = \sqrt{\frac{4}{3}I'_2} =& \sqrt{\frac{2}{3}E'_{IJ}(\mathbf{x},\mathbf{x}')E'_{IJ}(\mathbf{x},\mathbf{x}')} \\ =& \left\{\frac{2}{9}\Big[(E_{11}(\mathbf{x},\mathbf{x}') - E_{22}(\mathbf{x},\mathbf{x}'))^2 + (E_{22}(\mathbf{x},\mathbf{x}') - E_{33}(\mathbf{x},\mathbf{x}'))^2\right. \\ &+ (E_{11}(\mathbf{x},\mathbf{x}') - E_{33}(\mathbf{x},\mathbf{x}'))^2\Big] + \frac{4}{3}\big[(E_{12}(\mathbf{x},\mathbf{x}') + E_{13}(\mathbf{x},\mathbf{x}'))^2 \\ &\left.+ E_{23}(\mathbf{x},\mathbf{x}'))^2\big]\right\}^{\frac{1}{2}}. \qquad (2.27)\end{aligned}$$

where E_{IJ} is the average of the Lagrangian strain tensor between points, $\mathbf{x}$ and $\mathbf{x}'$ (the Lagrangian strain is approximately equal to the true strain for the case of small strain). The failure criterion based on the deformation for the bond is then expressed as

$$E_{eq}(\mathbf{x},\mathbf{x}') > E_{eq}^{critical}(\mathbf{x},\mathbf{x}'). \qquad (2.28)$$

The second method introduced in [108] uses the averaged value of the volumetric strain, $E_{vol}(\mathbf{x},\mathbf{x}')$ in the principal directions:

$$\begin{aligned}E_{vol}(\mathbf{x},\mathbf{x}') =& I_1 + I_2 + I_3 \\ &= E_{11}(\mathbf{x},\mathbf{x}') + E_{22}(\mathbf{x},\mathbf{x}') + E_{33}(\mathbf{x},\mathbf{x}') \\ &+ E_{11}(\mathbf{x},\mathbf{x}')E_{22}(\mathbf{x},\mathbf{x}') + E_{22}(\mathbf{x},\mathbf{x}')E_{33}(\mathbf{x},\mathbf{x}') \\ &+ E_{11}(\mathbf{x},\mathbf{x}')E_{33}(\mathbf{x},\mathbf{x}') + E_{11}(\mathbf{x},\mathbf{x}')E_{22}(\mathbf{x},\mathbf{x}')E_{33}(\mathbf{x},\mathbf{x}'), \qquad (2.29)\end{aligned}$$

while the second failure criterion then takes the form

$$E_{vol}(\mathbf{x},\mathbf{x}') > E_{vol}^{critical}(\mathbf{x},\mathbf{x}'). \qquad (2.30)$$

2.4.3 Critical energy density

A state-based peridynamics (SB PD) failure criterion based on energy density has been developed in [65] relating the critical energy density, w_0 in a bond to the fracture energy, G_0. Similar to the integration used in the stretch based criterion, the total strain energy of all the bonds, each with an energy density w_0, crossing the fracture plane is (see, [65]):

$$G_0 = \int_0^{\delta} \int_0^{2\pi} \int_z^{\delta} \int_0^{\cos^{-1} z/\xi} w_0 \xi^2 \sin\phi d\phi d\xi dz, \tag{2.31}$$

solving for w_0 gives

$$w_0 = \frac{4G_0}{\pi\delta^4}, \tag{2.32}$$

which relates the critical energy density to the fracture toughness. A bond energy density, w_{xi} is a function of the PD force-vector state, $\underline{\mathbf{T}}$ and and the displacement difference between the particles. w_{xi} can be expressed as

$$w_{xi} = \int_0^{\boldsymbol{\eta}} \Big\{ \underline{\mathbf{T}}\, [\mathbf{x}, t] \langle \mathbf{x}' - \mathbf{x} \rangle - \underline{\mathbf{T}}\, [\mathbf{x}', t] \langle \mathbf{x} - \mathbf{x}' \rangle \Big\} d\boldsymbol{\eta}, \tag{2.33}$$

The bond fails if $w_{xi} > w_0$.

2.4.4 Maximum principal stress

Cauchy stress tensors at two interacting particles $\mathbf{x}$ and $\mathbf{x}'$ can be respectively evaluated as $\boldsymbol{\sigma}_{\mathbf{x}}$ and $\boldsymbol{\sigma}_{\mathbf{x}'}$ [7]. Then, the Cauchy stress tensor on the virtual PD bond connecting particles $\mathbf{x}$ and $\mathbf{x}'$ can be obtained by using the mean value of stress at these two particles, $\boldsymbol{\sigma}_{\mathbf{xx}'} = (\boldsymbol{\sigma}_{\mathbf{x}} + \boldsymbol{\sigma}_{\mathbf{x}'})/2$. If the maximum principal stress between the particles reaches the uniaxial tensile strength of the material, f_t, the bond connecting the particles is considered broken. The Mohr-Coulomb criterion shown in Figure 2.9 is used to define the shear failure of the bond between particles. The shear failure criterion can be expressed as: The maximum shear stress in the bond between particle $\mathbf{x}$ and particle $\mathbf{x}'$, which can be expressed as:

$$\tau_{\mathbf{xx}'} = \frac{\sigma^1_{\mathbf{xx}'} - \sigma^3_{\mathbf{xx}'}}{2}, \tag{2.34}$$

and τ_{cr} is the critical shear stress, which is expressed as

$$\tau_{cr} = \left[\frac{C}{\tan\phi} + \frac{1}{2}(\sigma^1_{\mathbf{xx'}} + \sigma^3_{\mathbf{xx'}}) \right] \sin\phi. \tag{2.35}$$

where C is the cohesive strength, ϕ is the internal frictional angle, $\sigma^1_{\mathbf{xx'}}$ and $\sigma^3_{\mathbf{xx'}}$ are respectively the maximum principal stress and minimum principal stress of bond. When the stresses on the bond reach the Mohr-Coulomb criterion, the bond between the two interacting particles is broken, which results in shear failure. If the maximum shear stress between the particles, $\tau_{\mathbf{xx'}}$ exceeds the critical shear stress τ_{cr}, the bond connecting the particles is broken.

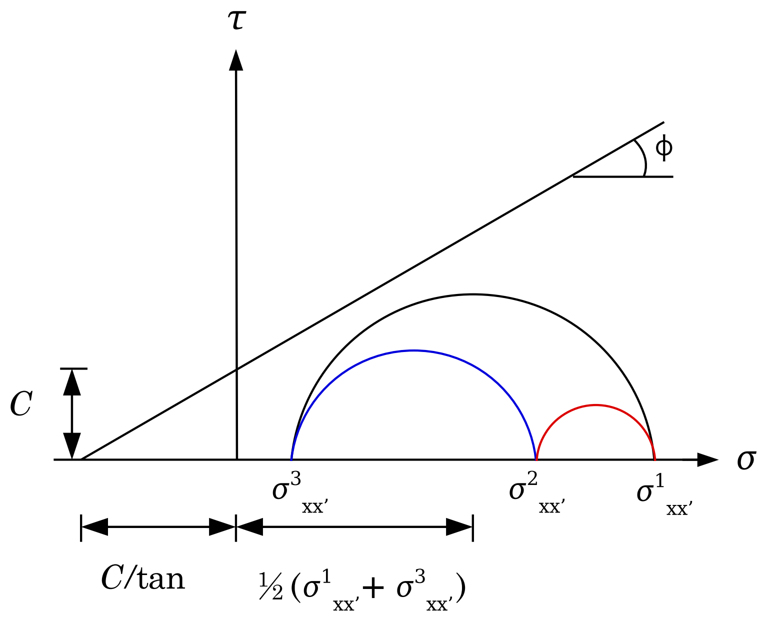

Figure 2.9: The Mohr-Coulomb failure criterion.

2.4.5 Critical bond strain

The damage rule based on the critical bond strain is based on the assumption that inelastic behaviour or failure is governed by a specified critical strain. Figure 2.10 (a) shows for mode I cracks, particles in S^+ and in S^- are under tension while for mode II cracks, shown in Figure 2.10 (b), particle in S^+ is under compression while particle in S^- is under tension. The reason is that a Mode I crack forms symmetric crack surfaces, while those in Mode II or Mode III are antisymmetric. As the shear deformation accounts for the shear damage, the damage rule should be at least related to the shear deformation [146]. Hence, [146] proposes a bond strain damage rule as

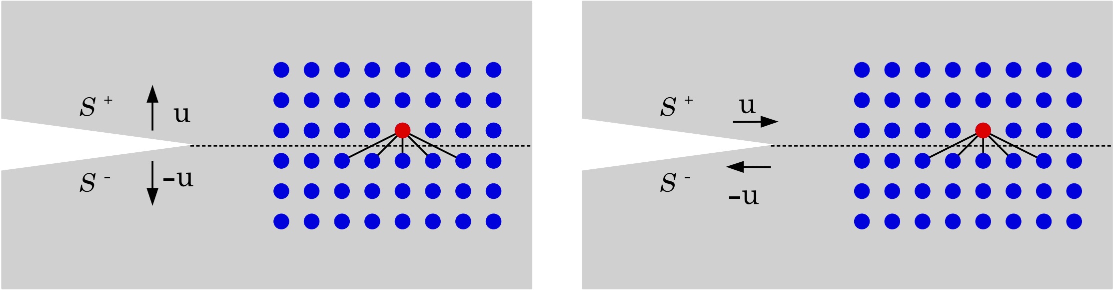

(a) Mode I: Opening (b) Mode II: In-plane shear

Figure 2.10: Mode I and mode II cracks (after Ren *et al.* [146])

$$\mu(\mathbf{x}, t, \boldsymbol{\xi}) = \begin{cases} 1 & \text{if } \varepsilon^d \geq \varepsilon^d_{max} \text{ and } (\theta_{\mathbf{x}} \geq 0 \text{ or } \theta_{\mathbf{x}'} \geq 0), \\ 0 & \text{otherwise.} \end{cases} \tag{2.36}$$

where $\varepsilon^d = ||\varepsilon^d||$ is deviatoric bond strain, $\theta_{\mathbf{x}}$ is the volume strain for particle $\mathbf{x}$. The damage happens when the deviatoric bond strain exceeds a critical value and at least one particle's volume strain is under tension. The anti-symmetric fracture surface in Mode II/III crack depends more on the deviatoric strain than the volume strain, therefore, the volume strain along the crack surface is assumed to be zero. The potential elastic energy for each bond is

$$e^d_{max} = \frac{3\mu}{m}(\boldsymbol{\xi})\boldsymbol{\eta}^d \cdot \boldsymbol{\eta}^d = \frac{3\mu}{m}(\varepsilon^d_{max})^2, \tag{2.37}$$

where $\omega(\boldsymbol{\xi}) = \xi^{-2}, m = \omega(\boldsymbol{\xi})\boldsymbol{\xi}_r \cdot \boldsymbol{\xi}_r dV = \frac{4\pi\delta^3}{3}$. Following the similar routine to [19], the work G_0 required to break all the bonds per unit fracture area is

$$G_0 = \int_0^{\delta}\int_0^{2\pi}\int_z^{\delta}\int_0^{\cos^{-1 z/\xi}} e^d_m ax\xi^2 \sin\phi d\phi d\xi d\theta dz, \tag{2.38}$$

$$= \frac{3\mu\phi\delta^4}{4m}(\varepsilon^d_{max})^2. \tag{2.39}$$

Then, the critical bond strain ε^d_{max} can be expressed as

$$\varepsilon^d_{max} = \frac{4}{3}\sqrt{\frac{G_0}{\mu\delta}}. \tag{2.40}$$

2.5 Numerical example of BB PD

The simplest damage criterion available in the PD literature is based on the critical bond stretch [147] as described above in Section 2.4.1. This damage criterion is used throughout the thesis and had been widely applied in BB PD, OSB PD and NOSB PD [116, 148]. In this section, the BB PD formulation described in Section 2.3 is used for a simple 2D problem of a linear elastic aluminium bar (similar to that presented in [108]). The bar domain at the beginning has a length, L of 0.254 m and a depth, d_0 of 0.012 m, as shown in Figure 2.11, fixed at one end and is subjected to initial velocity in the horizontal direction through an actual particle (not fictitious). The properties of the bar were Young's modulus of $E = 69$ GPa, Poisson's ratio of $\nu = 0.33$ and density of $\rho = 2710$ kg/m^3. The bar was uniformly discretised to form a 99 × 5 lattice of points. A time step size of $\Delta t = 5.0\times10^{-8}s$ was used in this problem [108]. A fictitious boundary layer was introduced outside the actual material domain at the boundary region where the size of the layer was equivalent to the horizon size, $\delta = 3.015\Delta x$ and displacement BC were imposed through the fictitious boundary layer. As can be seen, the bar was fixed at the fictitious boundary region in both directions. The initial conditions used in the problem were

$$\mathrm{u(x,0)} = 0 \quad \text{and} \quad \frac{\partial \mathrm{u(x,0)}}{\partial t} = \frac{\mathrm{100x}}{\mathrm{L}}, \tag{2.41}$$

where x is the spatial distance and the boundary conditions used were

$$\mathrm{u(x,}t) = 0 \quad \text{and} \quad \frac{\partial \mathrm{u(L,}t)}{\partial \mathrm{x}} = 0. \tag{2.42}$$

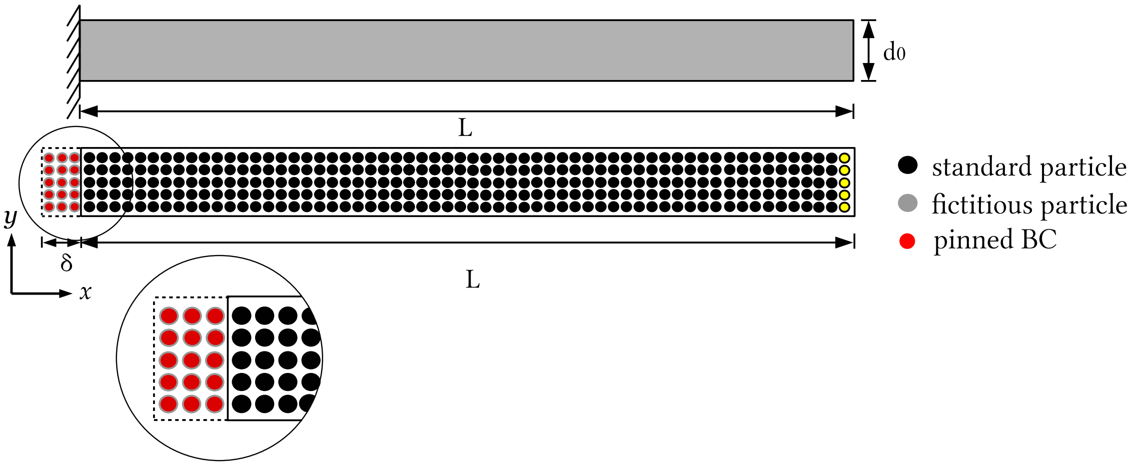

Figure 2.11: Illustration of the PD model of the aluminium bar.

Figures 3.7 and 2.13 shows the displacement and velocity of the bar at x = 0.254 m, 0.127 m and 0.051 m against the analytical solution available in [108]. It is observed that both figures show to be in a good agreement with the corresponding analytical solution while Figure 2.14 shows the stress-strain result obtained from the BB PD method and analytical solution [108] and as seen, they are indistinguishable. This suggests that the BB PD method employed provides good results.

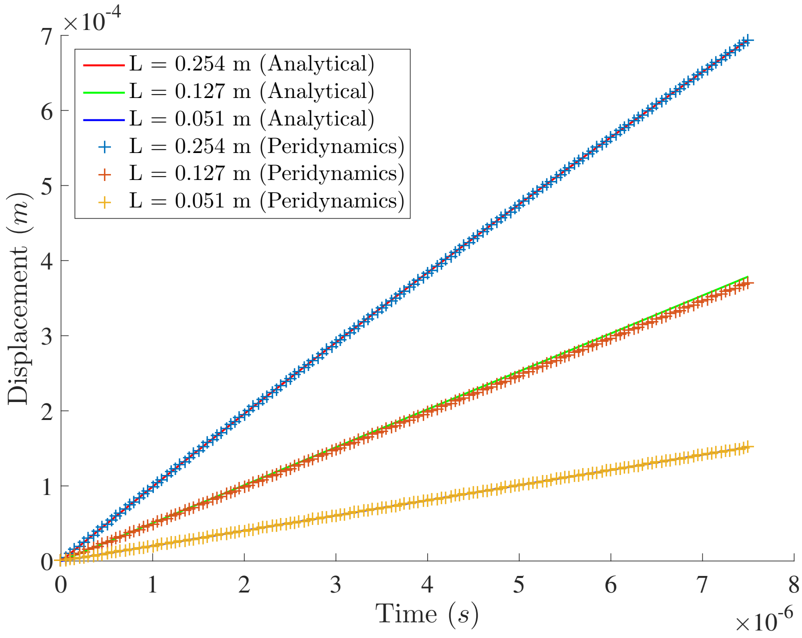

Figure 2.12: Aluminium bar: displacement at different locations in the bar using both analytical and BB PD method.

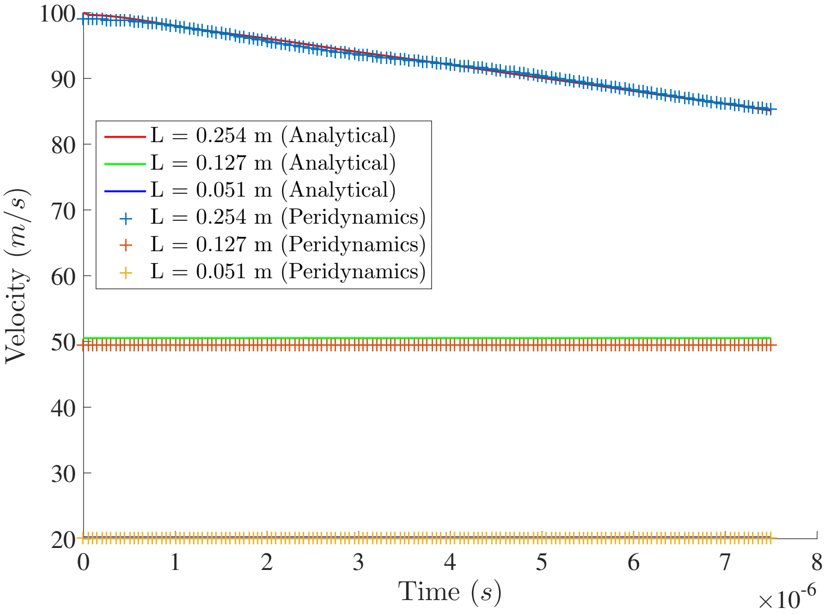

Figure 2.13: Aluminium bar: velocity at different locations in the bar using both analytical and BB PD method.

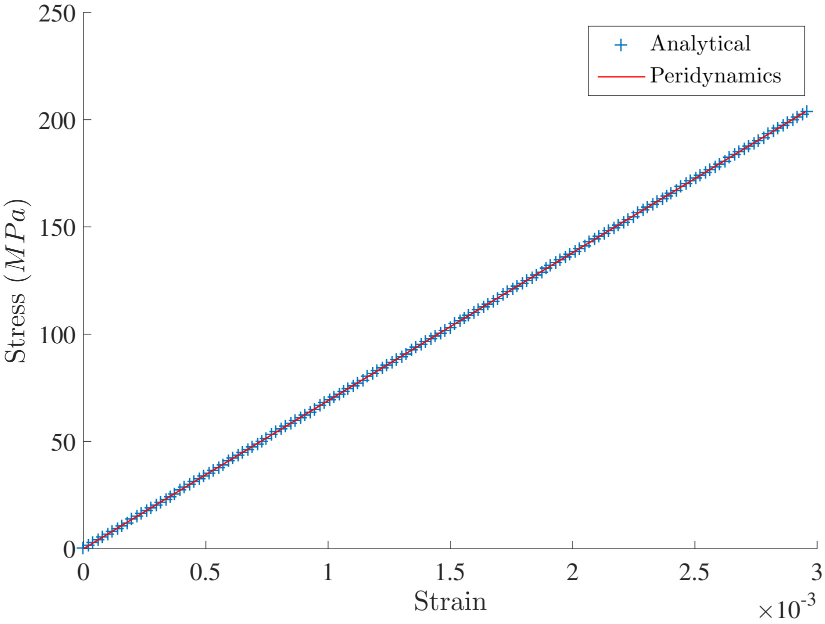

Figure 2.14: Aluminium bar: stress and strain at L = 127 mm.

2.6 Observations

In this chapter, the background of the PD has been discussed, including its current applications. The existence of spurious oscillations due to the zero-energy mode instabilities and various methods proposed in order to remove this problem have been highlighted from the literature. It has been shown that BB PD can be implemented easily, and it has been demonstrated that it can provide good results. However as mentioned earlier, BB PD scheme is restricted to fixed Poisson's ratios and a classical model can be solved in the frame of NOSB PD, by introducing the conception of state which corresponds with the conventional stress and strain tensors of classical continuum mechanics [66]. The BB PD formulation given in this chapter will be extended to a NOSB PD method in the next chapter. As the most common PD approaches utilise explicit time integration schemes and a drawback arises since it relies on a small time step size, it becomes expensive to obtain solutions. To combat this, the adaptive dynamic relaxation (ADR) method will be adopted to obtain the NOSB PD equilibrium solution in the next chapter.

Chapter 3

Explicit NOSB PD method for quasi-static analysis

In the previous chapter, the bond-based peridynamics (BB PD) formulation and a numerical example using this formulation were presented for a simple 2D linear elastic problem. However, as explained in Chapter 2, the BB PD scheme is restricted to constitutive models with fixed Poisson's ratios. The non-ordinary state-based peridynamics (NOSB PD) allows a constitutive model from the conventional theory of solid mechanics to be incorporated directly into a peridynamics (PD) model. However, development of the NOSB PD theory as an extension of BB PD are relatively few compared to the BB PD method. This chapter provides the essential background knowledge of NOSB PD, and begins with the NOSB PD formulation and numerical examples in Section 3.1. An Adaptive Dynamic Relaxation (ADR) method for PD will then be presented in Section 3.2. Numerical examples are demonstrated in Section 3.3, and finally, the chapter is concluded in Section 3.4.

3.1 Non-ordinary state-based peridynamics theory

Recall that in the BB PD, the forces, $\mathbf{f}$, between two particles ($\mathbf{x}$ and $\mathbf{x}'$) always have equal magnitude and opposite directions, thus conserving linear and angular momentum. On the other hand, in the OSB PD formulation, the forces in the bonds, $\mathbf{T}$ and $\mathbf{T}'$, are aligned in the direction of the bonds, as in the bond-based approach but do not need to have equal magnitudes as explained in Chapter 2, whereas in the NOSB PD formulation, there is no restriction on the magnitude and direction of forces [66].

3.1.1 Finite deformation mechanics

The deformation gradient is the fundamental quantity for measuring deformation in continuum mechanics. The deformation gradient characterises the deformation in the neighbourhood of a particle and is defined as

$$\mathbf{F} = \frac{\partial \mathbf{y}}{\partial \mathbf{x}}, \tag{3.1}$$

where $\mathbf{y}$ denotes a particle in the deformed configuration, while $\mathbf{x}$ denotes the same particle in the reference configuration. In accordance with the polar decomposition theorem, the deformation gradient allows the deformation from an initial state to a deformed configurations to be split into a sequence of stretch and rotation, as shown in Figure 3.1, that is

$$\mathbf{F} = \mathbf{R}\mathbf{U} = \mathbf{V}\mathbf{R}, \tag{3.2}$$

where $\mathbf{R}$ is an orthogonal tensor representing pure rotation, $\mathbf{U}$ and $\mathbf{V}$ are symmetric right and left stretch tensors, respectively. The right and left Cauchy-Green deformation tensors are defined as

$$\mathbf{C} = \mathbf{U}^2 = \mathbf{F}^T\mathbf{F} \;\text{ and }\; \mathbf{c} = \mathbf{V}^2 = \mathbf{F}\mathbf{F}^T. \tag{3.3}$$

In this thesis, logarithmic (Hencky) strain is used to measure the deformations of materials with the Hencky hyperelasticity assumption (a linear relationship between Kirchhoff stress and logarithmic strain). The Hencky strain is defined as

$$\boldsymbol{\epsilon} = \ln\big(\mathbf{c}\big), \tag{3.4}$$

and is expressed in engineering notation as

$$\boldsymbol{\epsilon}(2D) = \begin{bmatrix} \boldsymbol{\epsilon}_{xx} \\ \boldsymbol{\epsilon}_{yy} \\ 2\boldsymbol{\epsilon}_{xy} \end{bmatrix}. \tag{3.5}$$

The Kirchhoff stress is then given by

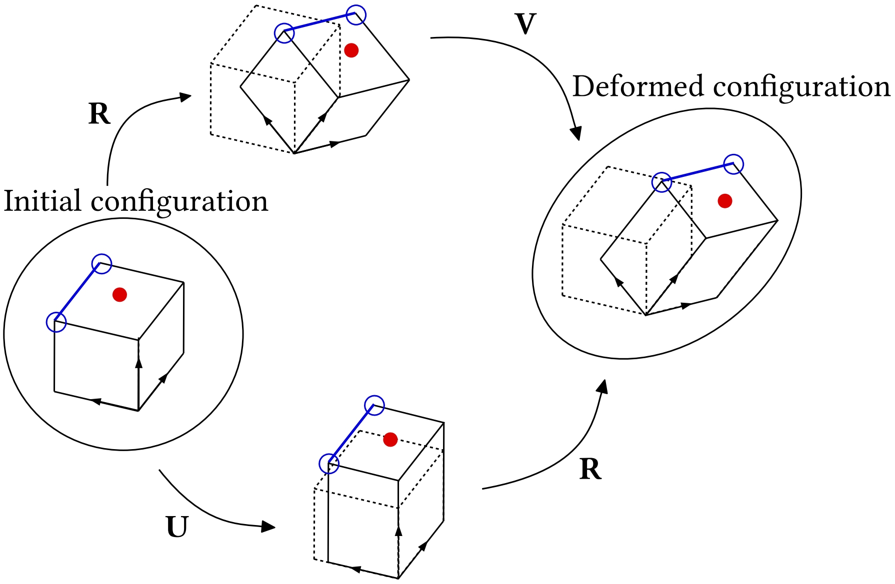

Figure 3.1: Illustration of the polar decomposition of deformation gradient.

$$\boldsymbol{\tau} = \mathbf{D_e}\boldsymbol{\epsilon}, \tag{3.6}$$

where $\mathbf{D_e}$ is the elastic stiffness matrix and for plane strain problems,

$$\mathbf{D_e} = \frac{E}{(1+\nu)(1-2\nu)} \begin{bmatrix} 1-\nu & \nu & 0 \\ \nu & 1-\nu & 0 \\ 0 & 0 & 1-2\nu \end{bmatrix}. \tag{3.7}$$

The Cauchy stress tensor can be expressed as

$$\boldsymbol{\sigma} = \frac{\boldsymbol{\tau}}{J}, \tag{3.8}$$

where the stress tensors are related by the volumetric ratio, J, between the deformed and reference configurations, given by the determinant of the deformation gradient

$$J = \det \mathbf{F}. \tag{3.9}$$

3.1.2 The equation of motion

Based on the principle of virtual work, the equation of motion of NOSB PD takes the following form [66]

$$\mathbf{L} + \mathbf{b} = \rho \ddot{\mathbf{u}}, \tag{3.10}$$

where the internal force vector at particle $\mathbf{x}$ is

$$\mathbf{L}[\mathbf{x}, t] = \int_R \Big\{ \underline{\mathbf{T}}\,[\mathbf{x}, t]\langle \mathbf{x}' - \mathbf{x} \rangle - \underline{\mathbf{T}}\,[\mathbf{x}', t]\langle \mathbf{x} - \mathbf{x}' \rangle \Big\} dV_{\mathbf{x}'}, \tag{3.11}$$

in which ρ represents the mass density in the reference configuration, $\ddot{\mathbf{u}}$ is the second-order time derivative of displacement $\mathbf{u}$ or acceleration, $\mathbf{b}$ is the body force at time t, and $\underline{\mathbf{T}}\,[\mathbf{x}, t]\langle \mathbf{x}' - \mathbf{x} \rangle$ is the force vector-state. The angle brackets $\langle\ \rangle$ denotes the vector mapped by the force vector-state originating at the particle in square brackets $[\ ]$. $\mathbf{L}[\mathbf{x}, t]$ depends not only on the deformation of all bonds connected to particle $\mathbf{x}$ but also on the deformation of all bonds connected to particle $\mathbf{x}'$. $V_{\mathbf{x}'}$ is the volume associated with particle $\mathbf{x}'$. A kinematic illustration of NOSB PD is shown in Figure 3.2 where R is a circular neighbourhood of given radius with δ centered at particle $\mathbf{x}$. The reference position vector state between two particles is denoted by $\boldsymbol{\xi} = \mathbf{x}' - \mathbf{x}$ and the relative displacement by $\boldsymbol{\eta} = \mathbf{u}' - \mathbf{u}$. Using those definitions, the deformation vector state, $\underline{\mathbf{Y}}$ denotes the deformed state of the bond where $\mathbf{y}$ and $\mathbf{y}'$ are shown after a displacement has been imposed on particles $\mathbf{x}$ and $\mathbf{x}'$ respectively. The specific vector states that are important in the PD concept are:

The relative position vector in undeformed configuration, denoted by

$$\bullet\text{reference position vector state} : \underline{\mathbf{X}}\langle \boldsymbol{\xi} \rangle = \boldsymbol{\xi} = \mathbf{x}_j - \mathbf{x}_i, \tag{3.12}$$

and the relative displacement is denoted by

$$\bullet\text{displacement vector state}: \underline{\mathbf{U}}[\mathbf{x},t]\langle\boldsymbol{\xi}\rangle = \boldsymbol{\eta} = \mathbf{u}(\mathbf{x}_j,t) - \mathbf{u}(\mathbf{x}_i,t). \tag{3.13}$$

The deformation vector state, $\underline{\mathbf{Y}}$ denotes the deformed form of initial bond vector, defined as

$$\bullet\text{deformation vector state}: \underline{\mathbf{Y}}[\mathbf{x},t]\langle\boldsymbol{\xi}\rangle = \boldsymbol{\xi} + \boldsymbol{\eta} = (\mathbf{x}_j + \mathbf{u}(\mathbf{x}_j,t)) - (\mathbf{x}_i + \mathbf{u}(\mathbf{x}_i,t)). \tag{3.14}$$

The equation of motion in the NOSB PD, Eq. (3.10) and the integral expression in Eq. (3.11) can be approximated with a finite sum as

$$\Big(\sum_{j=1}^{m} \underline{\mathbf{T}}\,[\mathbf{x}_i,t]\langle\mathbf{x}_j - \mathbf{x}_i\rangle - \underline{\mathbf{T}}\,[\mathbf{x}_j,t]\langle\mathbf{x}_i - \mathbf{x}_j\rangle\Big)V_j + \mathbf{b}(\mathbf{x}_i,t) = \rho(\mathbf{x}_i)\ddot{\mathbf{u}}(\mathbf{x}_i,t), \tag{3.15}$$

where j is a counter for the m particles in the horizon of particle i and V_j is the volume of particle j in reference configuration. The PD force-vector state of the bond vector $\boldsymbol{\xi}$ can be obtained from the first Piola-Kirchhoff stress tensor as [108]

$$\underline{\mathbf{T}}\,[\mathbf{x},t]\langle\mathbf{x}' - \mathbf{x}\rangle = \omega\langle\boldsymbol{\xi}\rangle\mathbf{P}^T\mathbf{B}\,\boldsymbol{\xi}, \tag{3.16}$$

where the first Piola-Kirchhoff stress, $\mathbf{P}$, for each particle $\mathbf{x}$ can be obtained from the Cauchy stress, $\boldsymbol{\sigma}$, and the deformation gradient, $\mathbf{F}$, as

$$\mathbf{P} = J\boldsymbol{\sigma}\mathbf{F}^{-T}. \tag{3.17}$$

The nonlocal PD deformation gradient is expressed as

$$\mathbf{F} = \left(\int_R \omega\langle\boldsymbol{\xi}\rangle(\underline{\mathbf{Y}}(\boldsymbol{\xi}) \otimes \boldsymbol{\xi})dV_{\boldsymbol{\xi}}\right)\mathbf{B}^{-1}, \tag{3.18}$$

where $\mathbf{B}$ is the nonlocal shape tensor and is dependent on the orientation of the bonds attached to the point of interest in the reference configuration

$$\mathbf{B} = \int_R \omega\langle\boldsymbol{\xi}\rangle(\boldsymbol{\xi}\otimes\boldsymbol{\xi})dV_{\boldsymbol{\xi}}, \tag{3.19}$$

where $\otimes$ denotes the dyadic product of two vectors.

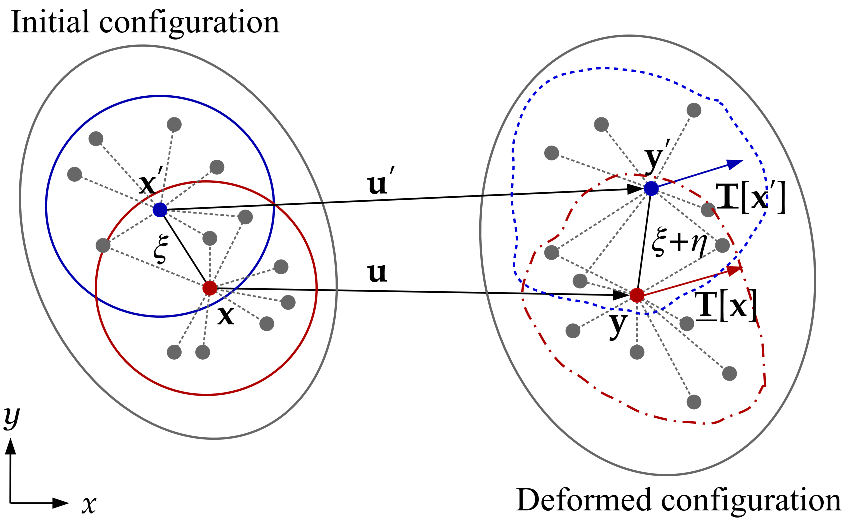

Figure 3.2: Kinematic illustration of NOSB PD in 2D.

In (3.16),(3.17) and (3.19), $\omega\langle\boldsymbol{\xi}\rangle$ is a dimensionless non-negative weighting function of radius δ in the reference frame, that defines the horizon in which the nonlocal interactions take place. In this work, consistent with [108], a constant weighting function is adopted, that is

$$\omega\langle\boldsymbol{\xi}\rangle = \begin{cases} 1 & \text{if } \boldsymbol{\xi} \leq \delta, \\ 0 & \text{if } \boldsymbol{\xi} > \delta. \end{cases} \tag{3.20}$$

For a discrete system, the shape tensor in Eq. (3.19) at particle i can be expressed as a Riemann sum in matrix form as

$$\mathbf{B} = \begin{bmatrix} \sum_{j=1}^{m} \omega\langle\boldsymbol{\xi}\rangle(\xi_x\xi_x)V_j & \sum_{j=1}^{m} \omega\langle\boldsymbol{\xi}\rangle(\xi_x\xi_y)V_j \\ \sum_{j=1}^{m} \omega\langle\boldsymbol{\xi}\rangle(\xi_y\xi_x)V_j & \sum_{j=1}^{m} \omega\langle\boldsymbol{\xi}\rangle(\xi_y\xi_y)V_j \end{bmatrix}, \tag{3.21}$$

and the nonlocal deformation gradient in Eq. (3.18) as

$$\mathbf{F} = \begin{bmatrix} \sum_{j=1}^{m} \omega\langle\boldsymbol{\xi}\rangle(\underline{Y}(\xi_x)\xi_x)V_j & \sum_{j=1}^{m} \omega\langle\boldsymbol{\xi}\rangle(\underline{Y}(\xi_x)\xi_y)V_j \\ \sum_{j=1}^{m} \omega\langle\boldsymbol{\xi}\rangle(\underline{Y}(\xi_y)\xi_x)V_j & \sum_{j=1}^{m} \omega\langle\boldsymbol{\xi}\rangle(\underline{Y}(\xi_y)\xi_y)V_j \end{bmatrix} \mathbf{B}^{-1}, \tag{3.22}$$

where $\mathbf{B}(\mathbf{x})$ referred to the non-local shape tensor, $\otimes$ denotes the dyadic product of two vectors and $\omega\langle\boldsymbol{\xi}\rangle$ is a dimensionless non-negative weighting function, that ensures the horizon in which the force relationship between particles is nonzero and all particles inside the horizon of $\mathbf{x}'$ have influence on $\mathbf{x}$ [77]. The weighting function depends only on the magnitude of $\boldsymbol{\xi}$. Various forms of weighting functions have been investigated in [149] for simple problems, and it was concluded in this thesis that a cubic weighting function was consistently the best choice to guarantee convergence with the varying horizon sizes and leads to lower errors for the NOSB PD as the behaviour of particles closer to $\mathbf{x}$ are more dominant those more distant. In this work, the constant weighting function is taken to be unity [108]

$$\omega\langle\boldsymbol{\xi}\rangle = \begin{cases} 1 & \text{if } \boldsymbol{\xi} \leq \delta, \\ 0 & \text{if } \boldsymbol{\xi} > \delta. \end{cases} \tag{3.23}$$

As suggested in Warren *et al.* [108], PD set of equations are solved using an explicit central difference time integration method to obtain values of displacement, velocity and acceleration as discussed by Taylor and Flanagan [150]. Acceleration, $\ddot{\mathbf{u}}$ can be obtained by using

$$\ddot{\mathbf{u}}(\mathbf{x}_i, t) = \frac{\mathbf{L}(\mathbf{x}_i, t) + \mathbf{b}(\mathbf{x}_i, t)}{\rho(\mathbf{x}_i)}. \tag{3.24}$$

Using Eq. (3.24), velocities, $\dot{\mathbf{u}}$ are obtained through a forward difference scheme, while the displacement, $\mathbf{u}$ is integrated with a backward difference approach as

$$\dot{\mathbf{u}}(\mathbf{x}_i, t + \Delta t) = \dot{\mathbf{u}}(\mathbf{x}_i, t) + \ddot{\mathbf{u}}(\mathbf{x}_i, t)\Delta t, \tag{3.25}$$

$$\mathbf{u}(\mathbf{x}_i, t + \Delta t) = \mathbf{u}(\mathbf{x}_i, t) + \dot{\mathbf{u}}(\mathbf{x}_i, t + \Delta t)\Delta t. \tag{3.26}$$

An estimate of the stable time increment can be taken as $\Delta t = \delta/c'$ where $c' \approx \sqrt{(\lambda + 2\mu)/\rho}$ is the dilatational wave speed and λ and μ are the Lamé elastic constants of the material [108]. The algorithm of explicit NOSBPD code implementation is presented in Figure 3.3.

lstp	1	2	$lstp_n$	FOR EACH Loadstep		
i	1	2	I_n	FOR EACH Particle		
j	1	2	$....m$	FOR EACH Neighbouring Particle		
$\boldsymbol{\xi}$				relative position	$\boldsymbol{\xi} = \mathbf{x}_j - \mathbf{x}_i$	(2.5)
$\boldsymbol{\eta}$				relative displacement	$\boldsymbol{\eta} = \mathbf{u}(\mathbf{x}_j, t) - \mathbf{u}(\mathbf{x}_i, t)$	(2.6)
$\mathbf{B}$				shape tensor	$\mathbf{B}(\mathbf{x}_i) = \left[\sum_{j=1}^{m} \omega\langle\boldsymbol{\xi}\rangle(\xi) \otimes \xi)V_j\right]$	(3.19)
$\mathbf{F}$				deformation gradient	$\mathbf{F}(\mathbf{x}_i) = \left[\sum_{j=1}^{m} \omega\langle\boldsymbol{\xi}\rangle(\underline{Y}(\xi) \otimes \xi)\right] V_j$	(3.18)
				END FOR		
$\mathbf{c}$				left Cauchy Green strain	$\mathbf{b}^e(\mathbf{x}_i) = \mathbf{F}(\mathbf{x}_i)\mathbf{F}(\mathbf{x}_i)^T$	
$\boldsymbol{\epsilon}$				logarithmic strain	$\boldsymbol{\epsilon}(\mathbf{x}_i) = \frac{1}{2}\log(\mathbf{b}^e)$	(3.4)
$\boldsymbol{\tau}$				Kirchhoff stress	$\boldsymbol{\tau}(\mathbf{x}_i) = \mathbf{D}_{\mathrm{e}}\boldsymbol{\epsilon}(\mathbf{x}_i)$	(3.6)
$\mathbf{P}$				first Piola Kirchhoff stress	$\mathbf{P}(\mathbf{x}_i) = \boldsymbol{\tau}(\mathbf{x}_i)\mathbf{F}(\mathbf{x}_i)^{-T}$	(3.17)
$\underline{\mathbf{T}}$				force-vector state	$\underline{\mathbf{T}}(\mathbf{x}_i) = \omega\langle\boldsymbol{\xi}\rangle\mathbf{P}(\mathbf{x}_i)^{-T}\mathbf{B}\,\boldsymbol{\xi}$	(3.16)
j	1	2	$....m$	FOR EACH Neighbouring Particle		
$\mathbf{L}$				particle internal force	$\mathbf{L}(\mathbf{x}_i) = \sum_{j=1}^{m}(\underline{\mathbf{T}}\,[\mathbf{x}_i, t] - \underline{\mathbf{T}}\,[\mathbf{x}_j, t])V_j$	(3.11)
				END FOR		
$\ddot{\mathbf{u}}$				acceleration	$\ddot{\mathbf{u}}(\mathbf{x}_i, t) = \frac{\mathbf{L}(\mathbf{x}_i,t)+\mathbf{b}(\mathbf{x}_i,t)}{\rho(\mathbf{x}_i)}$	(2.17)
$\dot{\mathbf{u}}$				velocity	$\dot{\mathbf{u}}(\mathbf{x}_i, t+\Delta t) = \dot{\mathbf{u}}(\mathbf{x}_i, t) + \ddot{\mathbf{u}}(\mathbf{x}_i, t)\Delta t$	(2.18)
$\mathbf{u}$				displacement	$\mathbf{u}(\mathbf{x}_i, t+\Delta t) = \mathbf{u}(\mathbf{x}_i, t) + \dot{\mathbf{u}}(\mathbf{x}_i, t+\Delta t)\Delta t$	(2.19)
				END FOR		

Figure 3.3: Explicit Non-ordinary state-based peridynamics (NOSB PD) algorithm sequence for 2D problem where *lstp* denotes the loadstep, i denotes the particle number and j denotes the neighbouring particles.

3.2 Adaptive Dynamic Relaxation (ADR)

The PD equation can also be used to solve quasi-static or static problems. The governing equation for quasi-static analysis is obtained by setting the acceleration term in Eq. (3.15) to zero, i.e.

$$\Big(\sum_{j=1}^{m} \underline{\mathbf{T}}\,[\mathbf{x}_i, t]\langle \mathbf{x}_j - \mathbf{x}_i\rangle - \underline{\mathbf{T}}\,[\mathbf{x}_j, t]\langle \mathbf{x}_i - \mathbf{x}_j\rangle\Big)V_j + \mathbf{b}(\mathbf{x}_i, t) = 0. \tag{3.27}$$

Substituting Eq. (3.16) into Eq. (3.27), the quasi-static equations of motion in NOSB PD can be expressed as

$$\Big(\sum_{j=1}^{m} \omega_i\langle\boldsymbol{\xi}\rangle\mathbf{P}(\mathbf{x}_i)^T\mathbf{B}(\mathbf{x}_i)\,\boldsymbol{\xi}_i - \omega_j\langle\boldsymbol{\xi}\rangle\mathbf{P}(\mathbf{x}_j)^T\mathbf{B}(\mathbf{x}_j)\,\boldsymbol{\xi}_j\Big)V_j + \mathbf{b}(\mathbf{x}_i, t) = 0. \tag{3.28}$$

However, in explicit solvers, the nature of explicit time integration requires small time steps and it becomes expensive to obtain solutions under static or quasi-static conditions [76, 151]. The use of an adaptive dynamic relaxation (ADR) technique then [152] becomes attractive for non-linear problems requiring large numbers of degrees of freedom. As explained in [76], the dynamic relaxation method is based on the fact that the static solution is the steady-state part of the transient response. The main idea of this method is to introduce artificial damping to the system, so that a steady-state solution can be reached as quickly as possible. However, it is not always possible to determine the most effective damping coefficient to be used for every time step and because of this, [153] proposed the way to calculate damping coefficient by calculating adaptively every time step. The method has been successfully applied in [76] to determine the failure of a simple structure. Based on the dynamic relaxation method, the PD equation in Eq.(2.4), can be modified as in [154] by introducing fictitious diagonal density matrix and damping terms as

$$\boldsymbol{\Lambda}\ddot{\mathbf{D}}(\mathbf{X}, t) + c_d\Lambda\dot{\mathbf{U}}(\mathbf{X}, t) = \mathbf{L}(\mathbf{D}, \mathbf{X}) + \mathbf{b}(\mathbf{X}) \tag{3.29}$$

where $\boldsymbol{\Lambda}$ is the fictitious diagonal density matrix and c_d is the damping coefficient whose values are determine by Gerschgorin's theorem [153]. The vectors $\mathbf{X}$ and $\mathbf{D}$

contain the initial position and displacement of the particles, respectively, and they can be expressed as

$$\mathbf{X}^T = \{\mathbf{x}, \mathbf{x}_2, ..., \mathbf{x}_{In}\} \tag{3.30}$$

and

$$\mathbf{D}^T = \{\mathbf{d}(\mathbf{x}_1, t), \mathbf{d}(\mathbf{x}_2, t), ..., \mathbf{d}(\mathbf{x}_{In}, t)\}, \tag{3.31}$$

where I_n is the total number of particles. By utilising central-difference explicit integration, velocities for the next time step can be obtained as

$$\dot{\mathbf{u}}^{n+1/2} = \Big[(2 - c_d \Delta t)\mathbf{d}^{n-1/2} + 2\Delta t \Lambda^{-1}(\mathbf{L} + \mathbf{b})^n]/\Big[2 + c_d \Delta t\Big], \tag{3.32}$$

where n indicates the nth iteration, and Δt is the time step size. However, the above expression cannot be used to start the integration due to the unknown velocity field at $t^{-1/2}$ but the process can be started by using

$$\dot{\mathbf{u}}^{1/2} = \Delta t \mathbf{\Lambda}^{-1}(\mathbf{L} + \mathbf{b})^0/2. \tag{3.33}$$

The updated displacements are given by

$$\mathbf{d}^{n+1} = \mathbf{U}^n + \Delta t \dot{\mathbf{u}}^{n+1/2}. \tag{3.34}$$

The density matrix $\mathbf{\Lambda}$, damping coefficient c_d and time step size do not have to be physically meaningful quantities, as mentioned in [153]. The key thing here is that the t is not a real meaure of time and the Δt is just a measure of your progression through the algorithm. A time step size of ($\Delta t = 1$) is a convenient choice to obtain faster convergence according to [76]. Thus they can be chosen to obtain faster convergence. The most common method to choose density matrix is based on

Gerschgorin's theorem, which can be written as [153]

$$\mathbf{\Lambda}^{-1} = \frac{1}{4}\Delta t^2 \sum_j |k_{ij}|, \tag{3.35}$$

where i is the corresponding particle and j is the particle connected to the corresponding particle i and k_{ij} calculated as [1]

$$k_{ij} = 5\pi\delta^2 bc, \tag{3.36}$$

where bc is the bond constant expressed as

$$bc = \frac{18K}{\pi\delta^4}, \tag{3.37}$$

where K is the bulk modulus and δ is the radius of PD horizon. The damping coefficient c_d is expressed as

$${c_d}^n = 2\sqrt{((\mathbf{U}^n)^T\mathbf{K}^n\mathbf{U}^n)/((\mathbf{U}^n)^T\mathbf{U}^n)}, \tag{3.38}$$

where $\mathbf{K}^n$ is the diagonal stiffness matrix and the ith component can be given by

$$K_{ii}^n = -((\mathbf{L}+\mathbf{b})_i^n/\mathbf{\Lambda}^{-1} - (\mathbf{L}+\mathbf{b})_i^{n-1}/\mathbf{\Lambda}^{-1})/(\Delta t\dot{\mathbf{U}}_i^{n-1/2}). \tag{3.39}$$

The algorithm of explicit NOSBPD code implementation with ADR is presented in Figure 3.4.

lstp	1	2	$lstp_n$	FOR EACH Loadstep		
i	1	2	I_n	FOR EACH Particle		
$\mathbf{\Lambda}^{-1}$				density matrix	$\mathbf{\Lambda}^{-1} = \frac{1}{4}\Delta t^2 \sum_j \lvert k_{ij} \rvert$	(3.35)
j	1	2	$....m$	FOR EACH Neighbouring Particle		
$\mathbf{B}$				shape tensor	$\mathbf{B}(\mathbf{x}_i) = \left[\sum_{j=1}^{m} \omega\langle\boldsymbol{\xi}\rangle(\xi) \otimes \xi)V_j\right]$	(3.19)
$\mathbf{F}$				deformation gradient	$\mathbf{F}(\mathbf{x}_i) = \left[\sum_{j=1}^{m} \omega\langle\boldsymbol{\xi}\rangle(\underline{Y}(\xi) \otimes \xi)\right] V_j$	(3.18)
				END FOR		
$\mathbf{b}^e$				left Cauchy Green strain	$\mathbf{b}^e(\mathbf{x}_i) = \mathbf{F}(\mathbf{x}_i)\mathbf{F}(\mathbf{x}_i)^T$	
$\boldsymbol{\epsilon}$				logarithmic strain	$\boldsymbol{\epsilon}(\mathbf{x}_i) = \frac{1}{2}\log(\mathbf{b}^e)$	(3.4)
$\boldsymbol{\tau}$				Kirchhoff stress	$\boldsymbol{\tau}(\mathbf{x}_i) = \mathbf{D}^e\boldsymbol{\epsilon}(\mathbf{x}_i)$	(3.6)
$\mathbf{P}$				first Piola Kirchhoff stress	$\mathbf{P}(\mathbf{x}_i) = \boldsymbol{\tau}(\mathbf{x}_i)\mathbf{F}(\mathbf{x}_i)^{-T}$	(3.17)
$\underline{\mathbf{T}}$				force-vector state	$\underline{\mathbf{T}}(\mathbf{x}_i) = \omega\langle\boldsymbol{\xi}\rangle\mathbf{P}(\mathbf{x}_i)^{-T}\mathbf{B}\,\boldsymbol{\xi}$	(3.16)
j	1	2	$....m$	FOR EACH Neighbouring Particle		
$\mathbf{L}$				particle internal force	$\mathbf{L}(\mathbf{x}_i) = \sum_{j=1}^{m}(\underline{\mathbf{T}}\,[\mathbf{x}_i, t] - \underline{\mathbf{T}}\,[\mathbf{x}_j, t])V_j$	(3.11)
				END FOR		
K_{ii}^n				diagonal stiffness matrix	$\frac{K_{ii}^n = -((\mathbf{L}+\mathbf{b})^{n}{}_i^n / \mathbf{\Lambda}^{-1} - (\mathbf{L}+\mathbf{b})_i^{n-1} / \mathbf{\Lambda}^{-1})}{(\Delta t \dot{\mathbf{U}}_i^{n-1/2})}$	(3.39)
${c_d}^n$				damping coefficient	${c_d}^n = 2\sqrt{((\mathbf{U}^n)^T\mathbf{K}^n\mathbf{U}^n)/((\mathbf{U}^n)^T\mathbf{U}^n)}$	(3.38)
$\dot{\mathbf{u}}^{1/2}$				velocity at $t^{1/2}$ (first time step)	$\dot{\mathbf{u}}^{1/2} = \Delta t\mathbf{\Lambda}^{-1}(\mathbf{L}+\mathbf{b})^0/2$	(3.33)
$\dot{\mathbf{u}}^{n+1/2}$				velocity for the next step	$\frac{\dot{\mathbf{u}}^{n+1/2} = \left[(2-c_d\Delta t)\mathbf{u}^{n-1/2} + 2\Delta t\mathbf{\Lambda}^{-1}(\mathbf{L}+\mathbf{b})^n\right]}{\left[2+c_d\Delta t\right]}$	(3.32)
u^{n+1}				displacement	$\mathbf{u}^{n+1} = \mathbf{u}^n + \Delta t\dot{\mathbf{u}}^{n+1/2}.$	(3.34)
				END FOR		

Figure 3.4: Explicit Non-ordinary state-based peridynamics (NOSB PD) algorithm sequence for 2D problem with Adaptive Dynamic Relaxation (ADR) where *lstp* denotes the loadstep, i denotes the particle number and j denotes the neighbouring particles.

3.3 Numerical examples

The NOSB PD formulation described in Section 3.1 was used for the same problem (2D problem of a linear elastic aluminium bar) as presented in Section 2.3. The bar initially had a length, L of 0.254 m and a depth, d_0 of 0.012 m as shown in Figure 2.11, fixed at one end and subjected to initial velocity in horizontal direction through an actual particle. The properties of the bar were Young's modulus of $E = 69$ GPa, Poisson's ratio of $\nu = 0.33$ and density of $\rho = 2710$ kg/m^3. The bar was uniformly discretised to form a 99 × 5 lattice of points. A time step size of $\Delta t = 5.0\times10^{-8}s$ was used in this problem [108].

Figures 3.5 and 3.6 shows the displacement and velocity of the bar at x = 0.254 m, 0.127 m and 0.051 m against the analytical solution available in [108]. The numerical results are in good agreement with the corresponding analytical solution. This suggests that the NOSB PD method is efficient to simulate this simple 2D bar problem. However, the oscillations exist in the PD solutions, as shown in Figure 3.6 and one possible cause may arise from the presence of the zero-energy modes in the NOSB PD, as already highlighted in Section 2.2.2.

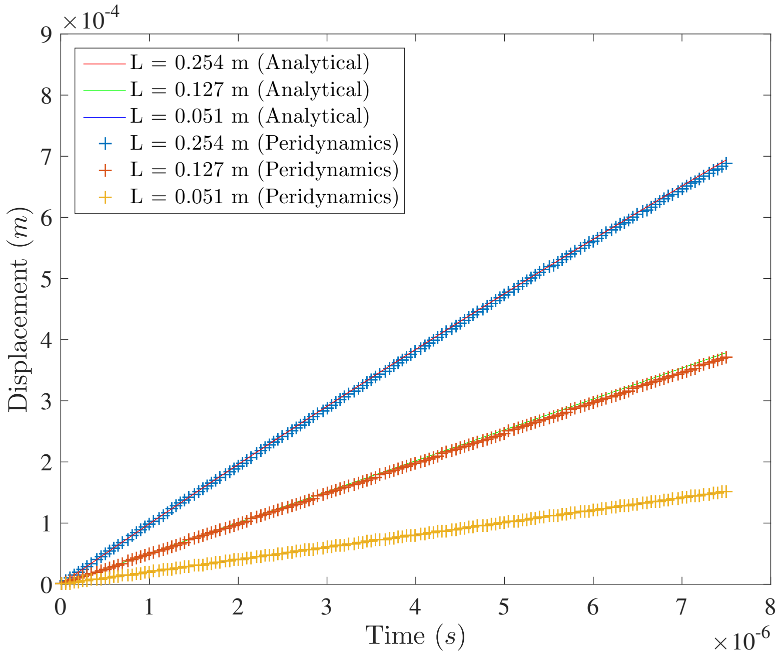

Figure 3.5: Aluminium bar: displacement at different location in the bar using both analytical and NOSB PD method.

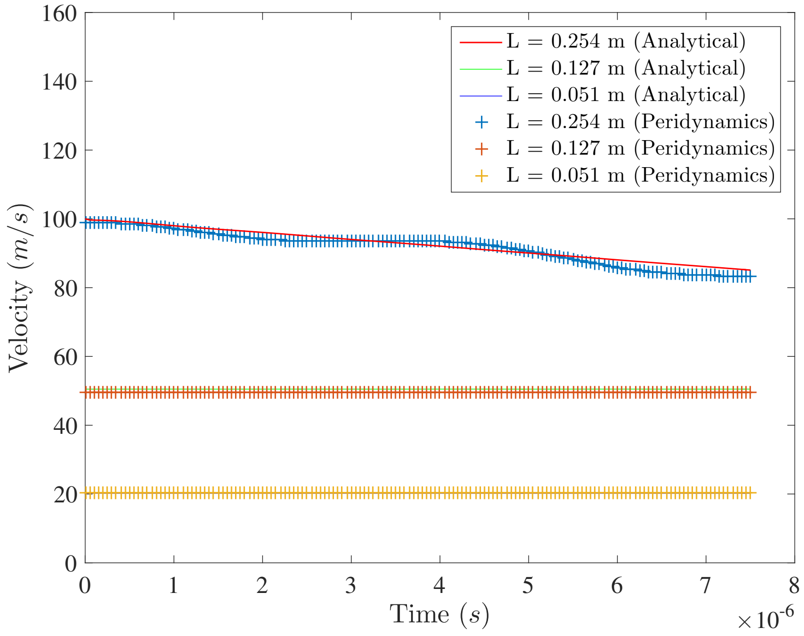

Figure 3.6: Aluminium bar: velocity at a different location in the bar using both analytical and NOSB PD method.

3.3.1 Plate under uniaxial tension

The NOSB PD formulation with ADR was used for a 2D problem of an elastostatic plate under uniaxial tension. The plate was of a size of 1 m × 0.5 m, as illustrated in Figure 3.7. The applied tension was introduced in the form of a body force per density of 2×10^{10} N/m^2 in one boundary layer region at both left and right of the plate in the horizontal direction. The properties of the plate were a Young's modulus of E = 200 GPa, a Poisson's ratio of $\nu = 0.33$ with a density of $\rho = 7850$ kg/m^3. The plate is discretised into 1250, 5000, 20000 and 80000 discrete PD particles to form 50 × 25 particles, 100 × 50, 200 × 100 and 400 × 200 lattices, respectively with the horizon , $\delta = 3.015\Delta x$. Time steps of $\Delta t = 1\ s$ were used for this analysis.

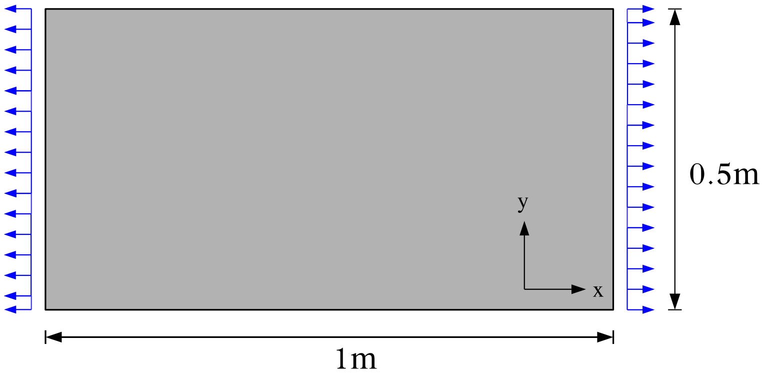

Figure 3.7: Geometry of a plate under uniaxial tension

In NOSB formulations, the presence of zero-energy modes due to the weak coupling of particle $\mathbf{x}$ to particles $\mathbf{x}'$ in its horizon causes stability issues [77]. These zero-energy modes were removed in this case by introducing a new force state, $\underline{\mathrm{T}}_{\mathrm{z}}\langle\boldsymbol{\xi}\rangle$ in addition to the present force state in (3.16) as proposed by Breitenfeld *et al.* [77] as

$$\underline{\mathbf{T}}\langle\boldsymbol{\xi}\rangle = \omega(|\boldsymbol{\xi}|)[\sigma^0(\mathbf{F})]^T \cdot \mathbf{B} \cdot \boldsymbol{\xi} + \underline{\mathbf{T}}_{\mathrm{z}}\langle\boldsymbol{\xi}\rangle. \tag{3.40}$$

A new force state, $\underline{\mathrm{T}}_{\mathrm{z}}\langle\boldsymbol{\xi}\rangle$ introduced with an additional linear springs of C_1 between a particle x and all the particles $\mathbf{x}'$ belonging to particle x horizon. The additional force state is one of the easiest to implement, given by [77]

$$\underline{\mathbf{T}}_{\mathrm{z}}\langle\boldsymbol{\xi}\rangle = C_1\omega(|\boldsymbol{\xi}|)(\mathbf{u}(\mathbf{x}') - \mathbf{u}(\mathbf{x})). \tag{3.41}$$

Figure 3.8 shows the convergence of displacement component in x and y direction of the plate at the length of $x = 0.255$ m and $y = 0.125$ m as time step increases with the number of particles 50 × 25 without the zero-energy mode control while Figure 4.7 shows the same result but with the zero-energy mode controlled. The result shown in Figure 3.8 illustrates the convergence in x direction but in the opposite direction as the actual result.

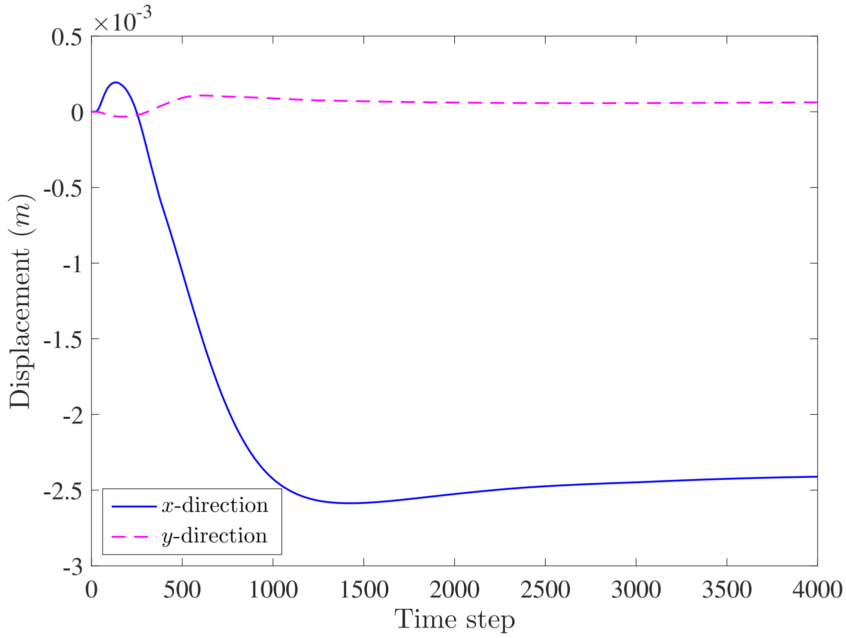

Figure 3.8: Plate under unixial tension: displacement in x and y direction using NOSB PD method without zero-energy mode controlled.

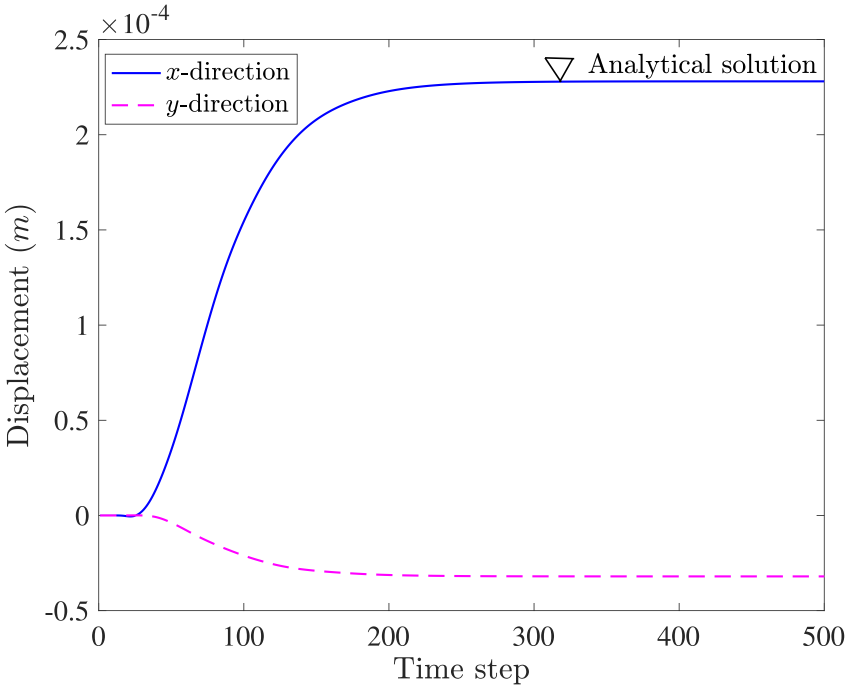

Figure 3.9: Plate under unixial tension: displacement in x and y direction using NOSB PD method with zero-energy mode controlled.

Figure 3.10 and Figure 3.11 shows the displacement variations along the center lines: $u_x(y = 0)$, $u_y(x = 0)$ compared with the analytical solution with 50 $\times$ 25 particles. There are slight differences of x and y displacements at the end of the plate due to the lower stiffness of particles near the boundary.

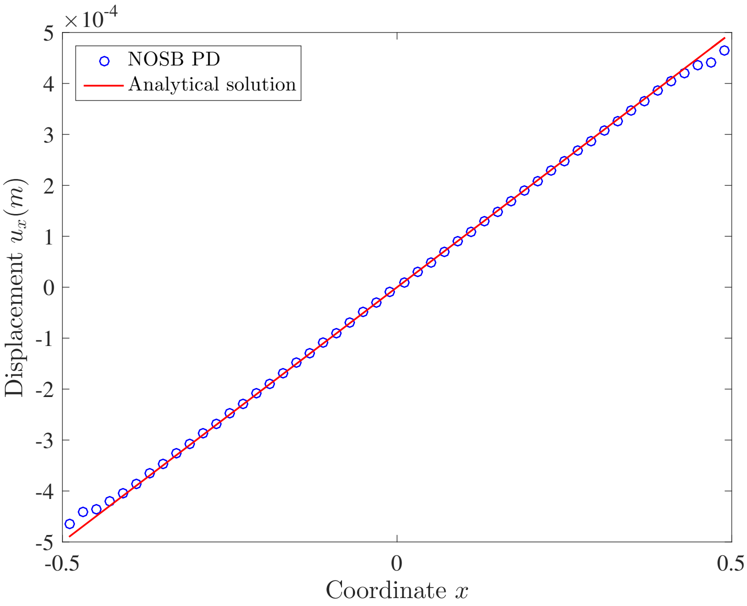

Figure 3.10: Plate under unixial tension: displacement variations in x direction along the center lines

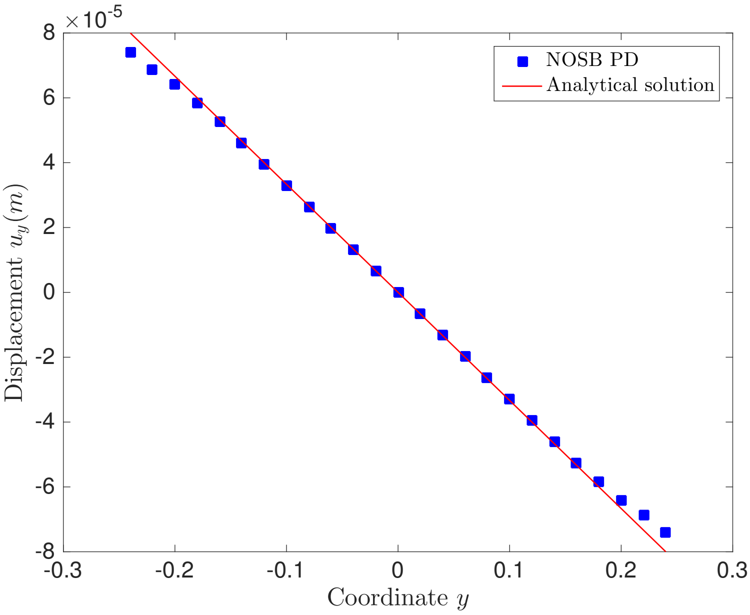

Figure 3.11: Plate under unixial tension: displacement variations in y direction along the center lines

The same problem was analysed using finer discretisations, which are 100 × 50, 200 × 100 and 400 × 200 particles. Figure 3.12 and Figure 3.13 shows that the result was more accurate when finer discretisations were used .

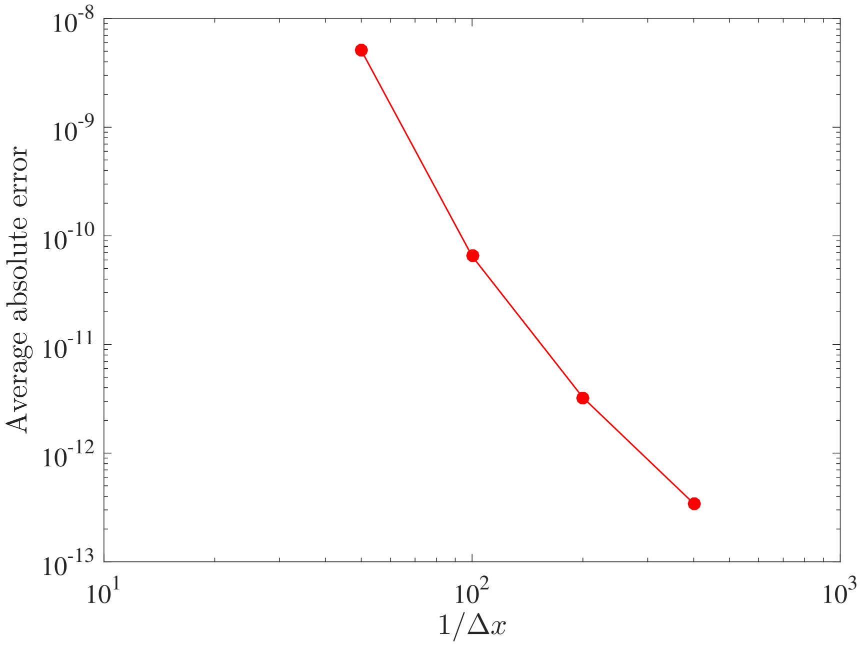

Figure 3.12: Plate under unixial tension: absolute error

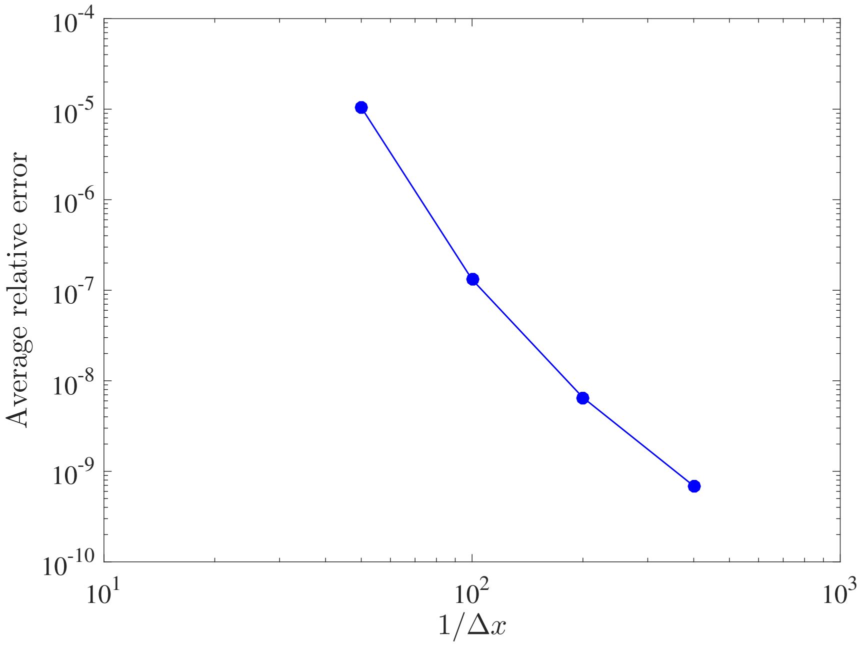

Figure 3.13: Plate under unixial tension: relative error

The same analysis was performed using a various time-step sizes. It was found that in dynamic relaxation, choice of time step size can cause some oscillations in the displacement in both x and y directions and takes larger time steps to reach the steady-state condition. Therefore, time step size of 1 ($\Delta t = 1$) and 10 ($\Delta t = 10$) both are convenient choice which converge faster.

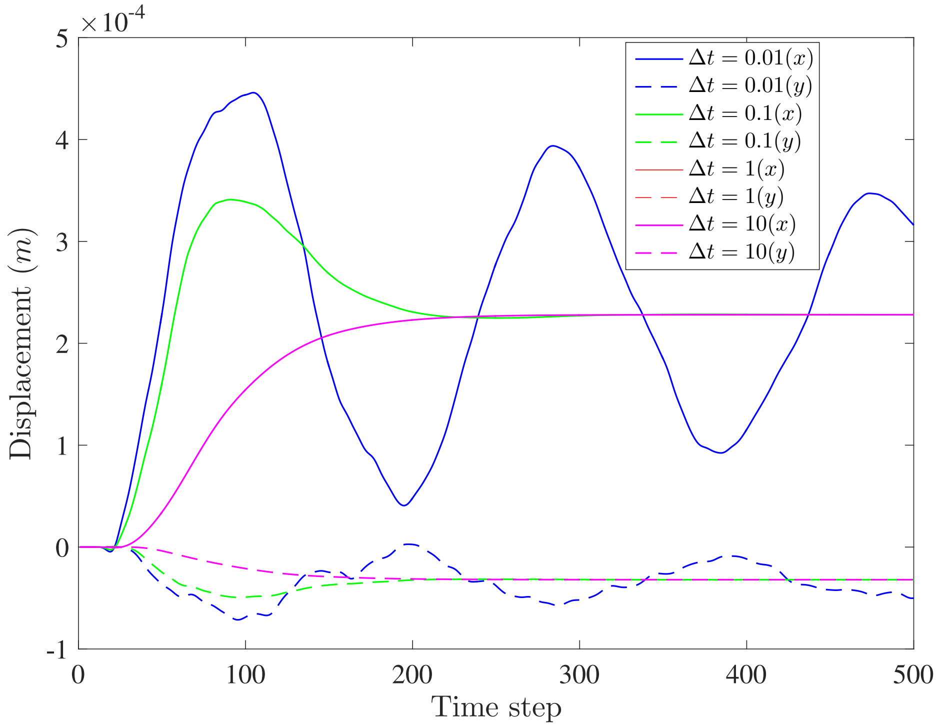

Figure 3.14: Displacement in x and y direction in the plate using NOSB PD method with zero-energy mode controlled and different time step size.

3.3.2 Tensile simulation of a plate with a circular hole under quasi-static loading

The final example in this chapter is a plate with a circular hole at the centre, as shown in Figure 3.15. The plate had a length of 50 mm, a width of 50 mm and the diameter of the hole was 10 mm, as shown in Figure 3.15. The material properties of the plate were $E = 192$ GPa and $\nu = 0.33$. The plate was uniformly discretised into 2,500 particles, with the grid spacing of $\Delta x = 1.0$ mm and the horizon size of $\delta = 3.015\Delta x$ was chosen. The plate was subjected to a slow rate of stretch along its horizontal edges (on the fictitious particles), representing quasi-static loading. The top and bottom ends of the plate were under a tensile load and were loaded in displacement control for 1000 time steps using the explicit time-stepping scheme with the ADR. Plane state of strain was assumed, and the loading speed was set at 2.7541×10^{-7} mm/s with a time step size of $\Delta t = 1\ s$. Additionally, the same problem was implemented using the BB PD in an explicit time scheme with ADR for comparison.

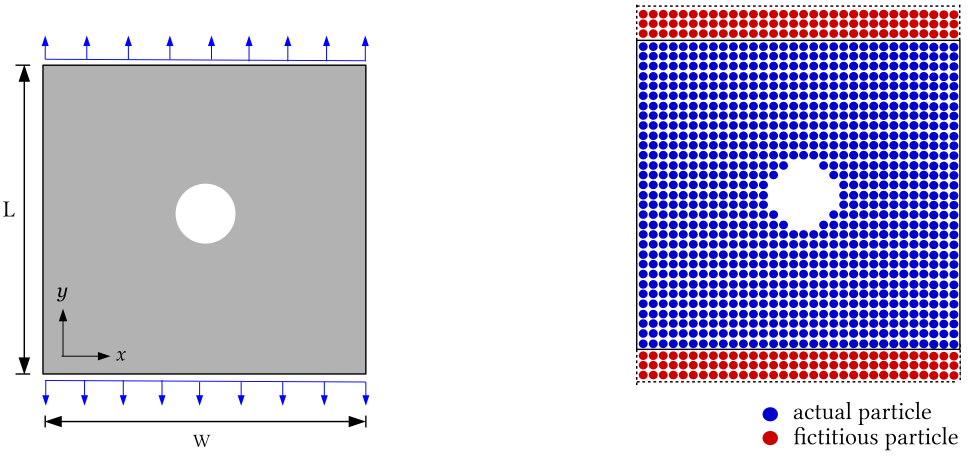

(a) Plate with a circular hole (b) Discrete model

Figure 3.15: Plate with a circular hole subjected to quasi-static loading

The stress concentration due to the applied loading was plotted in the absence of failure with NOSB PD, as shown in Figure 3.16. The stress concentration with and without zero-energy modes controlled was also compared. In the non-ordinary state-based formulation, zero-energy modes are associated to the weak coupling of particle $\mathbf{x}$ to particles $\mathbf{x}'$ in its horizon and thus results in oscillations in the deformation and stress fields and causes stability issues [77] and this can be clearly seen from Figure 3.16 (b).

Damage was then incorporated into the linear elastic model to study the influence of zero-energy modes on the damage and failure process of the material. The presence of zero-energy modes affects the failure pattern, and therefore various control methods have been proposed to alleviate this problem as discussed above. [77, 125] both developed methods to suppress zero-energy modes and significantly reduce the undesired oscillation. In this example, a penalty force was introduced in addition to the present force state in Eq. (3.16) to eliminate the zero-energy mode instability thus avoiding a spurious solution using PD [77].

The critical stretch failure criterion is adopted, with critical stretch $s_c = 0.02$.

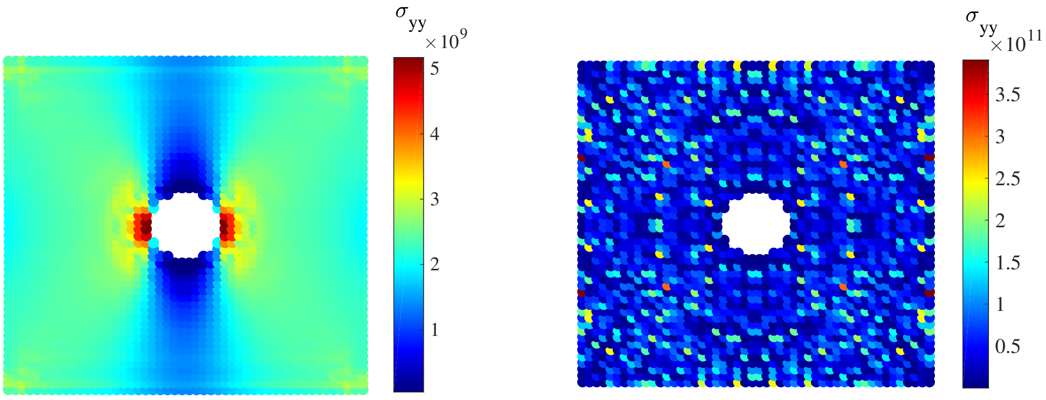

(a) Plate with hole: with zero-energy modes control (NOSB PD)

(b) Plate with hole: without zero-energy modes control (NOSB PD)

Figure 3.16: Plate with hole: stress concentration (NOSB PD).

Since material damage in PD is introduced through bond breakage between pairs of particles as explained in Section 2.4, the broken bonds will eventually lead to softening material response since failure bonds cannot sustain any load. The failure mode and damage evolution of the plate with and without zero-energy modes, control are plotted in Figures 3.17 and Figure 3.18. The presence of the zero-energy modes result in fictitious solutions that are not physically explained corrupt the approximated deformation solution field and caused a relatively large damage region in the plate, as illustrated in Figures 3.17 (b) and 3.18 (b), respectively. The deformation and damage evolution in NOSB PD with the zero-energy modes controlled, as shown in Figures 3.17 (a) and 3.18 (a) agrees well with the result of BB PD in Figure 3.19. Although there is no pre-existing crack in the plate, failure in this problem would initiate in the form of a crack at the tensile stress concentration sites. As shown in Figure 3.18 (a), the predicted damage also initiates in the stress concentration sites. Due to the low value of applied velocity along the boundary, representative of quasi-static loading, the cracks propagate towards the external vertical boundaries.

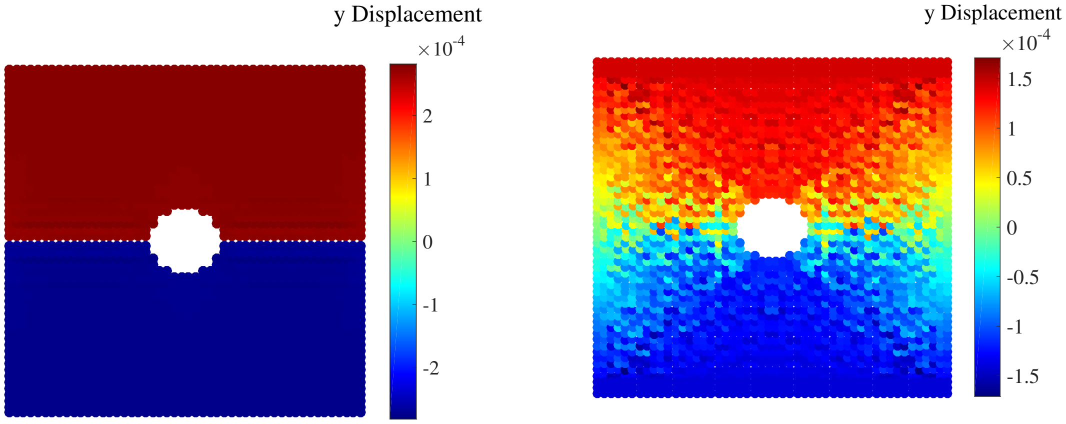

(a) Plate with hole: with zero-energy modes control (NOSB PD)

(b) Plate with hole: without zero-energy modes control (NOSB PD)

Figure 3.17: Plate with hole: deformation (NOSB PD).

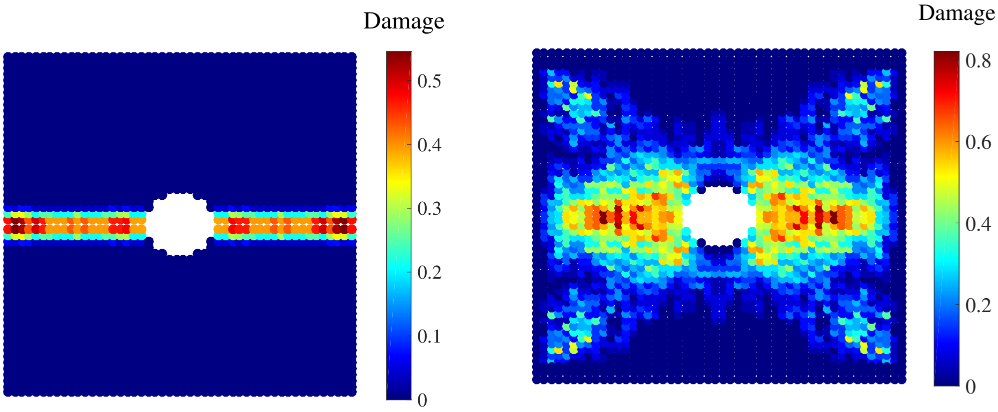

(a) Plate with hole: with zero-energy modes control (NOSB PD)

(b) Plate with hole: without zero-energy modes control (NOSB PD)

Figure 3.18: Plate with hole: damage contour (NOSB PD).

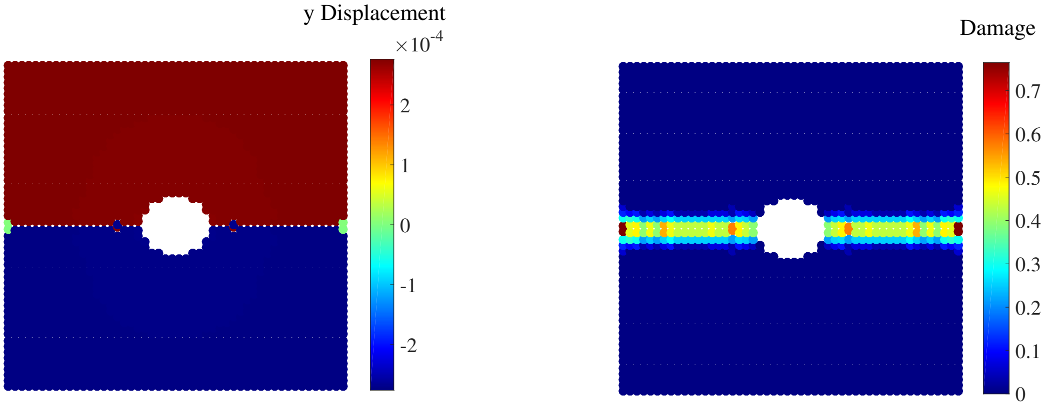

(a) Plate with hole: deformation (BB PD) (b) Plate with hole: damage contour (BB PD)

Figure 3.19: Plate with hole: deformation and damage contour (BB PD).

3.4 Observations

In this chapter, a brief review and the basic theory of NOSB PD framework for the analysis in the explicit scheme have been presented. The numerical framework and implementation procedures of the NOSB PD were discussed, and explicit implementation of the NOSBPD is adopted in this chapter. ADR with different time step sizes is investigated. An example demonstrates that the quasi-static problem showed good agreement with the analytical solution with ADR and zero-energy mode controlled. The method was then implemented correctly with a numerical example showing reasonable agreement with the analytical solution and convergence with the increasing number of degrees of freedom. The implementation of BB PD and NOSB PD with the introduction of bond failure has been validated using the numerical example of a plate with a circular hole. The approach developed over this, and the previous chapter has been shown to model damage without a pre-existing crack. The next chapter will introduce the NOSB PD implicit methods and validate the implementation of NOSB PD using numerical examples.

Chapter 4

Implicit NOSB PD with numerically generated tangent stiffness

In the previous chapter, explicit non-ordinary state-based peridynamics (NOSB PD) approaches have been presented and it has been shown that bond-based peridynamics (BB PD) and NOSB PD demonstrated good agreement with a problem that has an analytical solution, convergence with increasing particles discretisation and possessed attractive features in modelling damage. Problems with both small and large deformations are investigated in this thesis, but in this chapter, an implicit approach for NOSB PD based on numerically constructed tangent stiffnesses under static equilibrium condition with small and large deformation is presented. This chapter provides the numerical implementation procedure in Section 4.2. Simple particle deformation fields are investigated, and the accuracy is assessed in Section 4.3, and finally, the chapter review is drawn in Section 4.4.

4.1 Non-linear solution procedure

In this section, a detailed implementation of a geometrically non-linear implicit NOSB PD method is provided. A full Newton-Raphson (NR) method is utilised in this chapter in order to solve the non-linear system of equations. In order to advance the nonlinear analysis, the imposed loads here are applied in increments (or pseudo-time) steps and within each increment, force equilibrium is sought between internal resisting forces and external forces, resulting in the following expression that needs to be satisfied

$$\mathbf{f}^{int}(\mathbf{u}) - \mathbf{f}^{ext} = 0, \tag{4.1}$$

where $\mathbf{f}^{int}$ is the internal force and $\mathbf{f}^{ext}$ is the external force, where from Eq. (3.28)

$$\mathbf{f}^{int} = \Big(\sum_{j=1}^{m} \omega_i \langle \boldsymbol{\xi} \rangle \mathbf{P}(\mathbf{x}_i)^T \mathbf{B}(\mathbf{x}_i)\, \boldsymbol{\xi}_i - \omega_j \langle \boldsymbol{\xi} \rangle \mathbf{P}(\mathbf{x}_j)^T \mathbf{B}(\mathbf{x}_j)\, \boldsymbol{\xi}_j \Big) V_j \quad \text{and} \quad \mathbf{f}^{ext} = -\mathbf{b}(\mathbf{x}_i, t). \tag{4.2}$$

The solution of this non-linear system of equations can be obtained from repeatedly solving a linear system

$$\mathbf{K} \Delta \mathbf{u}_{l+1} = \mathbf{f}_l^{oobf}, \tag{4.3}$$

where $l{+}1$ represent the current equilibrium iteration within the NR procedure, $\mathbf{f}^{oobf} = \mathbf{f}^{ext} - \mathbf{f}^{int}$ is the global residual or out-of-balance force vector for the current displacements and $\mathbf{K}$ is the Jacobian matrix and can be expressed as

$$\mathbf{K} = \frac{\partial \mathbf{f}^{int}}{\partial \mathbf{u}} = \begin{bmatrix} \frac{\partial \mathbf{f}_1^{int}}{\partial u_1} & \frac{\partial \mathbf{f}_1^{int}}{\partial u_2} & \cdots & \frac{\partial \mathbf{f}_1^{int}}{\partial u_{ndof}} \\ \frac{\partial \mathbf{f}_2^{int}}{\partial u_1} & \frac{\partial \mathbf{f}_2^{int}}{\partial u_2} & \cdots & \frac{\partial \mathbf{f}_2^{int}}{\partial u_{ndof}} \\ \vdots & \vdots & \ddots & \vdots \\ \frac{\partial \mathbf{f}_{ndof}^{int}}{\partial u_1} & \frac{\partial \mathbf{f}_{ndof}^{int}}{\partial u_2} & \cdots & \frac{\partial \mathbf{f}_{ndof}^{int}}{\partial u_{ndof}} \end{bmatrix}, \tag{4.4}$$

with $ndof$ the total number of degrees of freedom in the system. The out-of-balance-force needs to be evaluated in order to verify if the system is in equilibrium. The current displacement is given by the summation of the incremental in displacements within the current loadstep and the displacement from the previously converged state (the displacement at the start of the load step), that is

$$\mathbf{u}_{n+1} = \mathbf{u}_n + \sum_{l=1}^{n_{\text{NRit}}} \triangle \mathbf{u}_l, \tag{4.5}$$

where $n{+}1$ represents the current loadstep and n_{NRit} is the total number of NR iterations. The NR procedure is performed until the convergence criterion is attained, such that

$$\frac{|\mathbf{f}^{oobf}|}{|\mathbf{f}^{ext}|} \leq tol, \tag{4.6}$$

where tol is the prescribed relative error tolerance (1×10^{-10} is used in this chapter and the rest of the thesis). The analysis proceeds with the next loadstep once the NR process obtains a converged solution to within the specified tolerance. The algorithm is outlined in Figure 4.1.

$lstp$	1	2	....lstp	FOR EACH Loadstep	
$\mathbf{f}^{ext}_{n+1}$				set the external force	
$NRit$	1	2	....NRit	WHILE $\vert\mathbf{f}^{oobf}_{n+1}\vert/\vert\mathbf{f}^{ext}_{n+1}\vert> tol$	(4.6)
$\Delta\mathbf{u}_{l+1}$				$\Delta\mathbf{u}_{l+1}$=$\mathbf{f}^{oobf}_{l}$ $\mathbf{K}$	(4.3)
$\mathbf{u}_{l+1}$				$\mathbf{u}_{l+1}$= $\mathbf{u}_{l}$ + $\Delta\mathbf{u}_{l+1}$	(4.5)
i	1	2	i	FOR EACH particle	
				NOSB PD with large deformation algorithm sequence	Figure 3.4
				END FOR	
$\mathbf{f}^{int}$				internal force	
$[K]$				global stiffness	
$\mathbf{f}^{oobf}_{l+1}$				$\mathbf{f}^{oobf}_{l+1}$=$\mathbf{f}^{ext}_{n+1}$-$\mathbf{f}^{int}_{l+1}$	(4.1)
				END WHILE	
$(.)_n$				set $\vert\mathbf{f}^{oobf}_{n+1}\vert/\vert\mathbf{f}^{ext}_{n+1}\vert$ equal to converged values	
				END FOR	

Figure 4.1: Implicit algorithm sequence.

4.2 Numerically generated stiffness matrix

In this chapter, the stiffness matrix is constructed via numerical approaches as follows

$$\mathbf{K} = \sum_{i}^{I_n} \sum_{j=1}^{m} \sum_{k}^{ndof} \left(\omega_i(|\boldsymbol{\xi}|) \frac{\partial \underline{\mathbf{T}}[\mathbf{x}_i]}{\partial \mathbf{u}_k} \right) - \left(\omega_j(|\boldsymbol{\xi}|) \frac{\partial \underline{\mathbf{T}}[\mathbf{x}_j]}{\partial \mathbf{u}_k} \right), \tag{4.7}$$

which can be expressed in matrix form as

$$\mathbf{K} = \begin{bmatrix} \frac{\sum_{j=1}^{m} \left(\omega_1(|\boldsymbol{\xi}|) \partial \underline{\mathbf{T}}[\mathbf{x}_1] \right) - \left(\omega_j(|\boldsymbol{\xi}|) \partial \underline{\mathbf{T}}[\mathbf{x}_j] \right)}{\partial u_1} & \cdots & \frac{\sum_{j=1}^{m} \left(\omega_1(|\boldsymbol{\xi}|) \partial \underline{\mathbf{T}}[\mathbf{x}_1] \right) - \left(\omega_j(|\boldsymbol{\xi}|) \partial \underline{\mathbf{T}}[\mathbf{x}_j] \right)}{\partial u_{ndof}} \\ \vdots & \ddots & \vdots \\ \frac{\sum_{j=1}^{m} \left(\omega_{I_n}(|\boldsymbol{\xi}|) \partial \underline{\mathbf{T}}[\mathbf{x}_{I_n}] \right) - \left(\omega_j(|\boldsymbol{\xi}|) \partial \underline{\mathbf{T}}[\mathbf{x}_j] \right)}{\partial u_1} & \cdots & \frac{\sum_{j=1}^{m} \left(\omega_{I_n}(|\boldsymbol{\xi}|) \partial \underline{\mathbf{T}}[\mathbf{x}_{I_n}] \right) - \left(\omega_j(|\boldsymbol{\xi}|) \partial \underline{\mathbf{T}}[\mathbf{x}_j] \right)}{\partial u_{ndof}} \end{bmatrix}. \tag{4.8}$$

Note that only the particles related to particle $\mathbf{x}_i$ and $\mathbf{x}_j$ contribute to the row of the overall stiffness corresponding to particle $\mathbf{x}_i$. For this reason, the matrix sparsity depends on the horizon size, δ. I_n is the total number of particles and therefore, for a 2D problem, the global matrix size is $2I_n \times 2I_n$. The stiffness matrix can be written as:

$$\mathbf{K}(\mathbf{x}) = \sum_{i=1}^{m} \left(\frac{\partial \underline{\mathbf{T}}\,[\mathbf{x}]\langle \mathbf{x}'_i - \mathbf{x} \rangle}{\partial \mathbf{u}} - \frac{\partial \underline{\mathbf{T}}\,[\mathbf{x}'_i]\langle \mathbf{x} - \mathbf{x}'_i \rangle}{\partial \mathbf{u}} \right) V_{\mathbf{x}'_i}, \tag{4.9}$$

where m is the number of neighbour particles of $\mathbf{x}$ and $V\mathbf{x}'_i$ is the volume occupied by each neighbour particle. The stiffness of a particle is influenced by its neighbours and the neighbours of the neighbour via the non-local nature of the method. Differencing formulas for tangent-stiffness matrix evaluation can be written as

$$\mathbf{K} = \frac{\partial \mathbf{L}}{\partial \mathbf{u}} = \begin{bmatrix} \frac{\partial \mathbf{L}_1}{\partial u_1} & \frac{\partial \mathbf{L}_1}{\partial u_2} & \cdots & \frac{\partial \mathbf{L}_1}{\partial u_{ndof}} \\ \frac{\partial \mathbf{L}_2}{\partial u_1} & \frac{\partial \mathbf{L}_2}{\partial u_2} & \cdots & \frac{\partial \mathbf{L}_2}{\partial u_{ndof}} \\ \vdots & \vdots & \ddots & \vdots \\ \frac{\partial \mathbf{L}_{ndof}}{\partial u_1} & \frac{\partial \mathbf{L}_{ndof}}{\partial u_2} & \cdots & \frac{\partial \mathbf{L}_{ndof}}{\partial u_{ndof}} \end{bmatrix}, \tag{4.10}$$

where from Eq. (3.28)

$$\mathbf{L} = \Big(\sum_{j=1}^{m} \omega_i \langle \boldsymbol{\xi} \rangle \mathbf{P}(\mathbf{x}_i)^T \mathbf{B}(\mathbf{x}_i)\, \boldsymbol{\xi}_i - \omega_j \langle \boldsymbol{\xi} \rangle \mathbf{P}(\mathbf{x}_j)^T \mathbf{B}(\mathbf{x}_j)\, \boldsymbol{\xi}_j\Big) V_j. \tag{4.11}$$

Note that $\mathbf{L}$=$\mathbf{f}^{int}$ in Eq. (4.2). Methods used to construct the tangent stiffness matrix include both analytical and numerical approaches and one method to calculate the tangent stiffness matrix numerically is by using a forward-difference scheme. The numerically constructed tangent stiffness is approximated in this chapter using

$$K_{ij} \simeq \frac{\mathbf{L}_i(\mathbf{u} + h\hat{\mathbf{e}}_j) - \mathbf{L}_i(\mathbf{u})}{h}, \tag{4.12}$$

where K_{ij} is the tangent-stiffness matrix entry at row i and column j. The first of the two terms in the numerator are the L_i evaluated in the current deformed configuration, $\mathbf{u}$, plus a small perturbation h in the direction $(\hat{e}_l)_j$ where $(\hat{e}_l)_j$ represents a unit-vector of j^{th} degree-of-freedom given by

$$(\hat{e}_l)_j = 1 \;\text{ if }\; l = j \quad \text{and} \quad (\hat{e}_l)_j = 0 \;\text{ if }\; l \neq j, \tag{4.13}$$

where l is the j^{th} component and to the fact that when h tends to 0 and without vanishing, the quotient on the right hand side provides a good approximation of the derivative, thus $h = 1 \times 10^{-7}\Delta x$ was used in this thesis after trial and error. For the second term in the numerator, $\mathbf{L}_i$, is evaluated in the current configuration. The NOSB PD algorithm sequence is shown in Figure 4.2.

lstp	1	2	$lstp_n$	FOR EACH Loadstep		
$\mathbf{f}_{n+1}^{ext}$				set the external force		
$\Delta\mathbf{u}$				$\Delta\mathbf{u}$ =$\mathbf{f}$ $\mathbf{K}^{-1}$		(4.3)
i	1	2	I_n	FOR EACH Particle		
j	1	2	$....m$	FOR EACH Neighbouring Particle		
$\boldsymbol{\xi}$				relative position	$\boldsymbol{\xi} = \mathbf{x}_j - \mathbf{x}_i$	(2.5)
$\boldsymbol{\eta}$				relative displacement	$\boldsymbol{\eta} = \mathbf{u}(\mathbf{x}_j, t) - \mathbf{u}(\mathbf{x}_i, t)$	(2.6)
$\mathbf{B}$				shape tensor	$\mathbf{B}(\mathbf{x}_i) = \left[\sum_{j=1}^{m} \omega\langle\boldsymbol{\xi}\rangle(\xi) \otimes \xi)V_j\right]$	(3.19)
$\mathbf{F}$				deformation gradient	$\mathbf{F}(\mathbf{x}_i) = \left[\sum_{j=1}^{m} \omega\langle\boldsymbol{\xi}\rangle(\underline{Y}(\xi) \otimes \xi)\right] V_j$	(3.18)
				END FOR		
$\mathbf{b}^e$				elastic left Cauchy Green strain	$\mathbf{b}^e(\mathbf{x}_i) = \mathbf{F}(\mathbf{x}_i)\mathbf{F}(\mathbf{x}_i)^T$	
$\boldsymbol{\epsilon}$				logarithmic elastic strain	$\boldsymbol{\epsilon}(\mathbf{x}_i) = \frac{1}{2}\log(\mathbf{b}^e)$	(3.4)
$\boldsymbol{\sigma}$				Cauchy stress	$\boldsymbol{\sigma}(\mathbf{x}_i) = D^e\boldsymbol{\epsilon}(\mathbf{x}_i)$	(3.6)
$\mathbf{P}$				first Piola Kirchhoff stress	$\mathbf{P}(\mathbf{x}_i) = \det\mathbf{F}(\mathbf{x})\boldsymbol{\sigma}(\mathbf{x})(\mathbf{F}(\mathbf{x})^{-1})^{\mathrm{T}}$	(3.17)
$\underline{\mathbf{T}}$				force-vector state	$\underline{\mathbf{T}}(\mathbf{x}_i) = \omega\langle\boldsymbol{\xi}\rangle\mathbf{P}(\mathbf{x}_i)^{-T}\mathbf{B}\,\boldsymbol{\xi}$	(3.16)
j	1	2	$....m$	FOR EACH Neighbouring Particle		
$\mathbf{L}$				particle internal force	$\mathbf{L}(\mathbf{x}_i) = \sum_{j=1}^{m}(\underline{\mathbf{T}}\,[\mathbf{x}_i, t] - \underline{\mathbf{T}}\,[\mathbf{x}_j, t])V_j$	(3.11)
				END FOR		
k	1	2	$....ndof$	FOR EACH Degree-of-freedom		
$\mathbf{K}$			stiffness		$\mathrm{K}_{ij} \simeq \frac{\mathbf{L}_i(\mathbf{u}+h\hat{\mathbf{e}}_j)-\mathbf{L}_i(\mathbf{u})}{h}$,	(4.12)
				END FOR		
				END FOR		

Figure 4.2: Non-ordinary state-based peridynamics (NOSB PD) algorithm sequence for 2D problem where *lstp* denotes the loadstep, i denotes the particle number and j denotes the neighbouring particles.

4.3 Simple deformation field investigation

Before continuing with the numerical examples of the large deformation problems in Section 4.4, it is useful to investigate some simple particle deformation fields. In this section, a series of numerical examples with simple deformation are presented, to verify the implicit NOSB PD model with large deformation problem. Additionally, all examples are under plane strain with elastic material.

4.3.1 Hydrostatic compression

Figure 4.3 shows a 2D linear elastic unit square domain under hydrostatic compression. The mid axis of the square is subjected to roller boundary condition (BC), and a prescribed displacement is imposed perpendicular to all edges. In order to implement a roller boundary condition and impose a prescribed displacement, a fictitious boundary layer was introduced outside the actual material domain at the boundary region where the size of the layer was equivalent to the horizon size and displacement boundary conditions (BC) were imposed through the fictitious boundary layer. The square plate modelled as had an initial length of $l_0 = 1$ m, as shown in Figure 4.3 and the material model was isotropic linear elasticity with Young's modulus of $E = 1.2$ MPa, and a Poisson's ratio of $\nu = 0.2$. The plate was uniformly discretised into four different particle discretisations; 100 particles (arranged in a 10 × 10 regular grid), 400 particles (arranged in a 20 × 20 regular grid), 1600 particles (arranged in a 40 × 40 regular grid) and 3600 (arranged in a 80 × 80 regular grid) particles with horizon size of $\delta = 1.015\Delta x$ to minimises the effects of zero-energy modes.

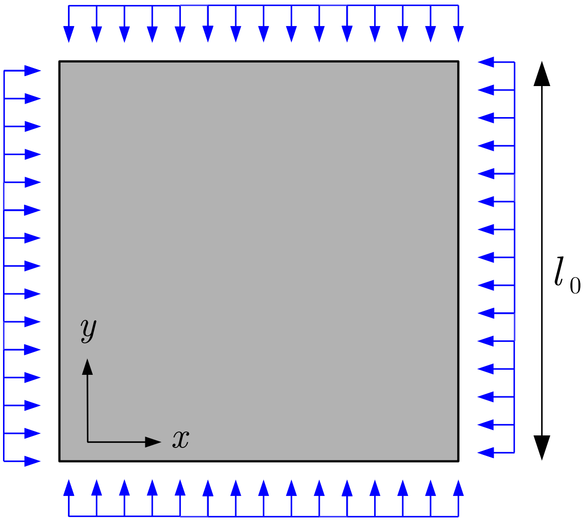

Figure 4.3: Square hydrostatic compression: Initial configuration.

The deformation gradient and logarithmic strain for this deformation are given by

$$[\mathbf{F}] = \begin{bmatrix} l/l_0 & 0 \\ 0 & l/l_0 \end{bmatrix} \quad , \quad [\boldsymbol{\epsilon}] = \begin{bmatrix} \ln(l/l_0) & 0 \\ 0 & \ln(l/l_0) \end{bmatrix} \tag{4.14}$$

where l_0 and l are the original and current square lengths plotted against the analytical values above in Figures 4.4 and 4.5, the strain and deformation gradient for particles arranged in a 80 × 80 regular grid. Figure 4.6 illustrates a larger relative error of displacement as the particle spacing becomes larger and as expected, increasing the number of particles minimise the displacement error.

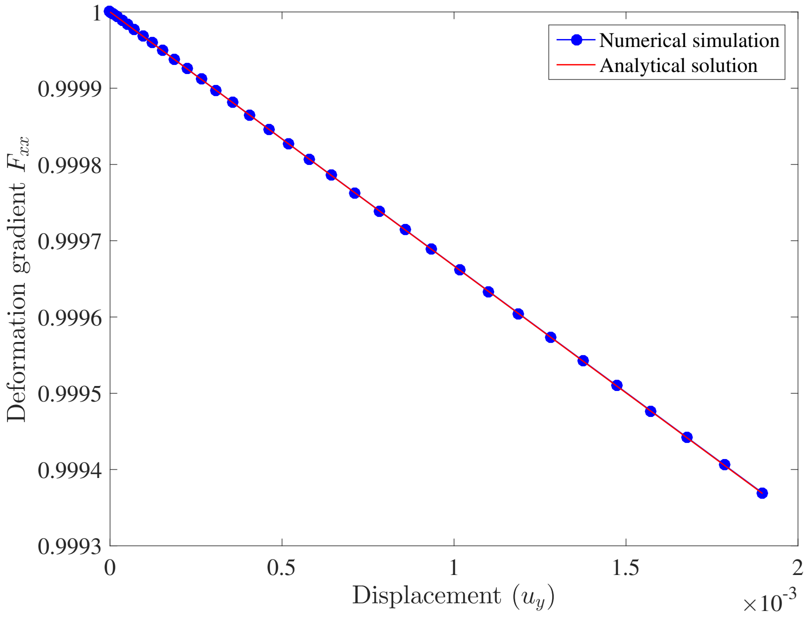

Figure 4.4: Square hydrostatic compression: deformation gradient

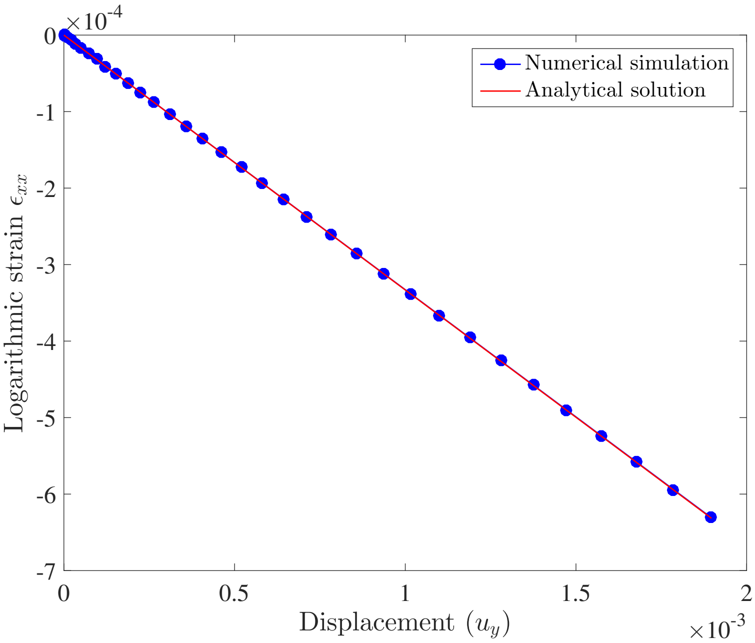

Figure 4.5: Square hydrostatic compression: logarithmic strain

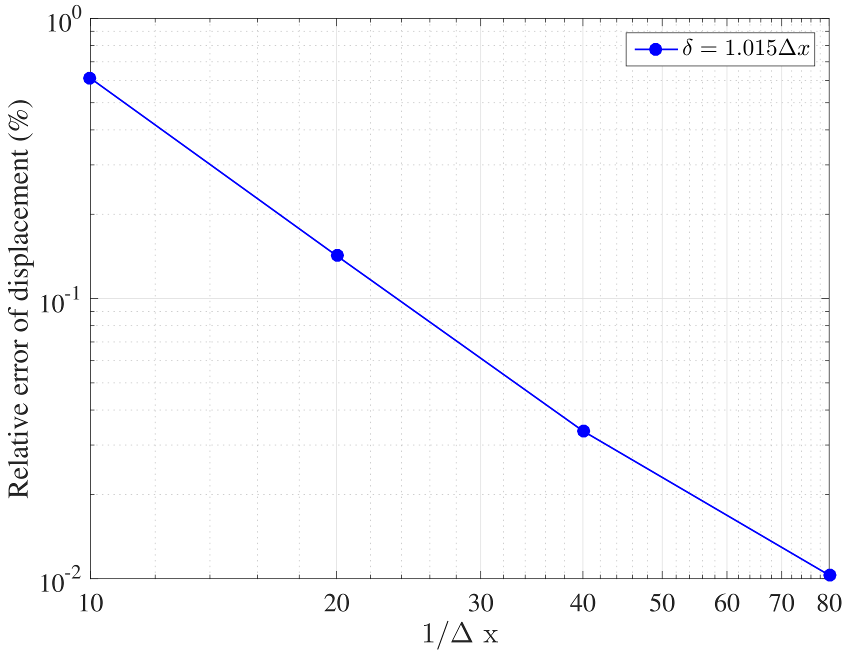

Figure 4.6: One-dimensional compression: convergence with $\delta = 1.015\Delta x$.

4.3.2 Elastic plate under uniaxial tension

This is a 2D problem of an elastic plate under uniaxial tension. The plate with a size of 1 m × 0.5 m was established, as illustrated in Figure 4.7. An applied traction was introduced in the form of a body force of $2 \times 10^{10}\,\mathrm{N/m^3}$ in one boundary layer region at both the left and right of the plate in the horizontal direction. The properties of the plate are Young's modulus of E = 200 GPa, a Poisson's ratio of $\nu = 0.33$ with a density of $\rho = 7850$ kg/m^3. The plate is discretised into discrete peridynamics 1250 particles with $\delta = 1.015\Delta\mathbf{x}$. The smallest possible horizon size was used in this example to reduce the effect of the zero-energy modes, as explained in Chapter 3.

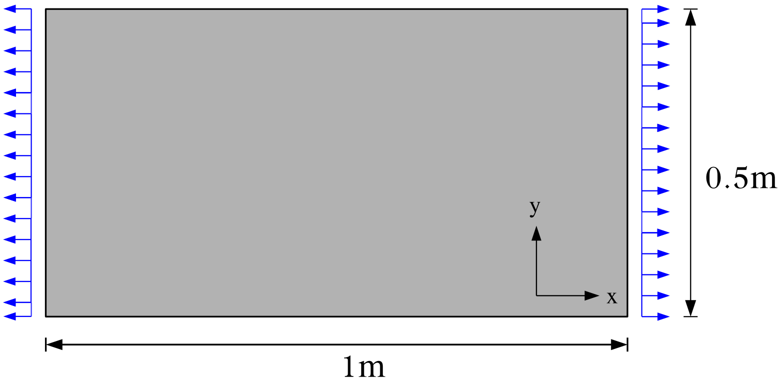

Figure 4.7: Geometry of a plate under uniaxial tension

Figure 4.8 shows the displacement variations along the centre lines: $u_x(y = 0)$ compared with the analytical solution, with 50 × 25 particles. There are slight differences of x displacements at the end of the plate due to the lower stiffness of particles near the boundary.

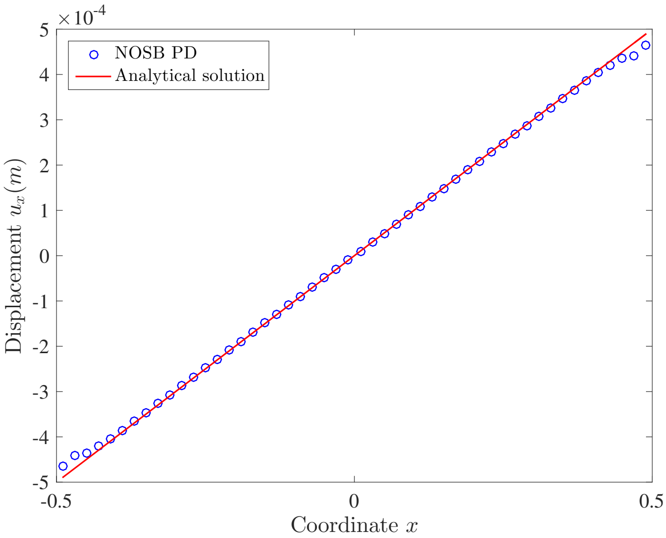

Figure 4.8: Plate under uniaxial tension: displacement variations in x direction along the centre lines

4.4 Numerical Examples

In this section, three more challenging numerical examples are presented which involve large deformations. A plate with under simple shear deformation is first analysed by NOSB PD, followed by the cantilever beam subjected to vertical load on its end. Then, the predicted normalised displacement of a simply supported slender beam is compared with the available analytical data.

4.4.1 Simple shear

A 2D square plate was modelled under simple shear deformation, using implicit NOSB PD with numerically constructed tangent stiffness in order to validate the large deformation formulation. The problem domain at the beginning had a height of 1 m and width of 1 m, Young's modulus of $E = 1.2 \times 10^3$ MPa and Poisson's ratio of $\nu = 0.2$. The initial and deformed configuration can be seen in Figure 4.9. The plate was uniformly discretised into 100 (arranged in 10 × 10 regular grid) particles with a horizon size, $\delta = 3.015\Delta x$. The response of the plate is modelled subjected to the displacement imposed over 40 loadsteps, horizontally parallel to the top edge and each horizontal layer. The vertical movement along the bottom and top edges were prevented and horizontal movement restrained along the bottom edge. The top face sheared distance is 7.38 m and the results of the simulation for the particle located in the middle of the plate (average of the four particles located nearest to the centre of the plate) are shown in Figures 4.10, 4.11 and 4.12. It can be seen that the deformation gradient, Cauchy stress and logarithmic strain agree well with the analytical solution. The deformation gradient and logarithmic strain, as shown are

$$[\mathbf{F}] = \begin{bmatrix} 1 & \Delta l \\ 0 & 1 \end{bmatrix} \quad \text{and} \quad [\boldsymbol{\epsilon}] = \ln \begin{bmatrix} 1 + (\Delta l)^2 & \Delta l \\ \Delta l & 1 \end{bmatrix}, \tag{4.15}$$

Where Δl is the top face sheared distance. The performance of the methods is measured by discrepancy between the numerical results and the analytical solutions. For example, the relative error is the absolute error divided by the magnitude of the analytical solutions, and those are computed as

$$R_{\sigma_i} = \frac{|(\sigma_i^n - \sigma_i^a)|}{|\sigma_i^a|}, \tag{4.16}$$

where σ_i^n and σ_i^a are the numerical and analytical stresses. The relative error from the implicit method is shown in Table 4.1. It can be seen that implicit time integration gives good accuracy. Those stress and strain errors seem large compared to the deformation gradient in xy direction because of the small displacement in y direction at the particles, which should be zero.

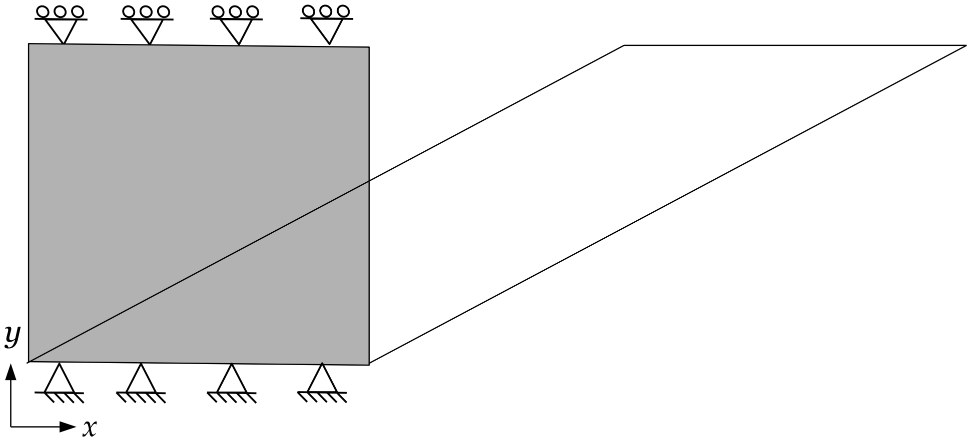

Figure 4.9: Simple shear problem showing initial (grey) and deformed (white) position.

Table 4.1: Deformation gradient, logarithmic strain and Cauchy stress relative error at the centre particle.

Value	F_{xy}	ϵ_{xx}	ϵ_{xy}	σ_{xx}	σ_{xy}
Error (%)	2.41×10^{-14}	1.17×10^{-3}	1.43×10^{-3}	2.54×10^{-2}	1.10×10^{-1}

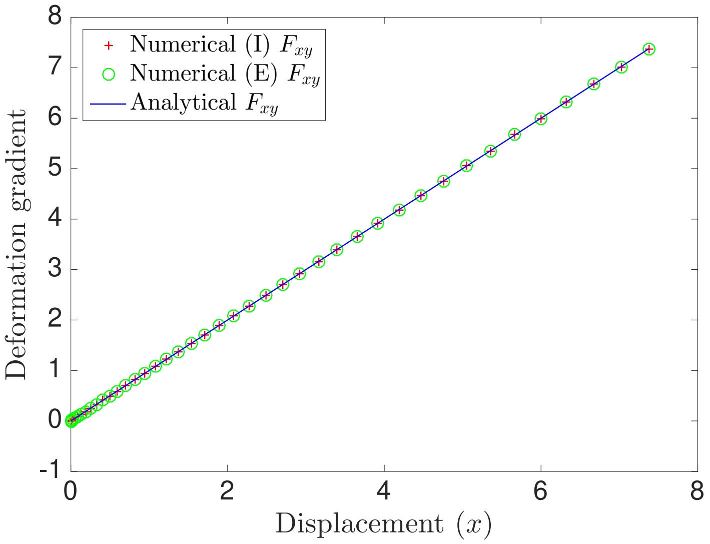

Figure 4.10: Deformation gradient.

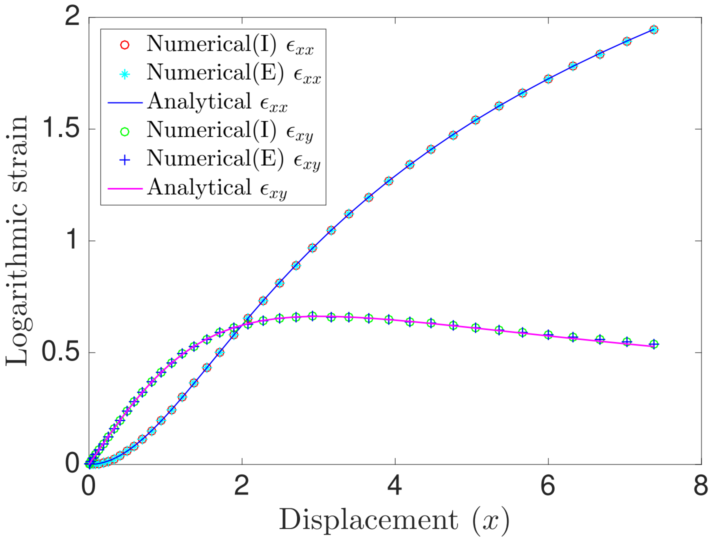

Figure 4.11: Logarithmic strain.

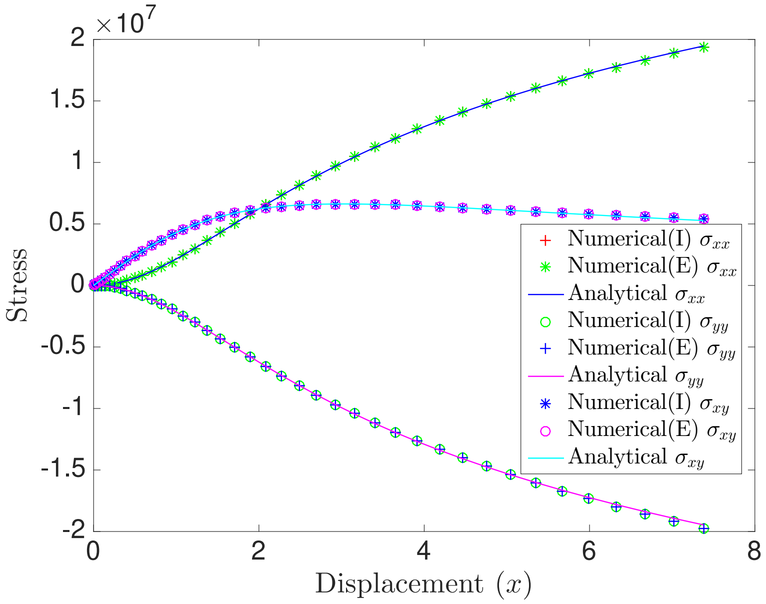

Figure 4.12: Cauchy stress.

4.4.2 Cantilever beam

The second example is an elastic cantilever beam, fixed at its root and subjected to a vertical mid-height particle load on its free end. Both explicit and implicit PD methods are used so that comparisons of performance can be made. The beam had a length of 10 m, depth 1 m, and was uniformly discretised into three different particles discretisations. Three different values of horizon radius were used, $\delta = 1.015\Delta x$,

$\delta = 2.015\Delta x$ and $\delta = 3.015\Delta x$. The material properties were Young's modulus of $E = 12$ MPa and Poisson's ratio of $\nu = 0.2$. In order to implement a clamped boundary condition, as explained in [141], a fictitious boundary layer was introduced outside the actual material domain at the boundary region where the size of the layer was equivalent to the horizon size and displacement boundary conditions were imposed through the fictitious boundary layer. The beam was fixed at the fictitious boundary region at the mid axis in both directions and roller boundary conditions applied to other particles along the left-hand fictitious region, allowing the structure to move only in the y-direction as shown in Figure 4.13. A vertical load of 100 kN was applied in 10 loadsteps using the implicit method and tolerance of 1×10^{-10} was used on the global normalised out-of-balance force. The loads were applied through an actual particle on the right-hand region at the mid axis, as shown in Figure 4.13. In the explicit method, a vertical load, in the form of body force of $b = p/A_{\mathbf{x}}\Delta x$, where $A_{\mathbf{x}}$ is the particle area, was applied over a number of iteration steps to reach a steady-state solution, with a stopping criterion based on the static residual (balance of external and internal forces) and precision of 10^{-6} as shown in Figure 4.14. Figure 4.15 depicts the load-displacement response for both horizontal (h) and vertical (v) displacements and the corresponding analytical solution (A) from [155] with three different numbers of particle used, and $\delta = 1.015\Delta x$. Note that both the vertical and horizontal normalised displacement with finer particle discretisations is larger than with coarser particle discretisations and converges towards the analytical solution. The final deformed configurations for three different particle refinements are shown in Figure 4.16, demonstrating that finer discretisations with $\delta = 1.015\Delta x$ yield results closer to the analytical solution.

The total calculation time and displacement relative error of the actual end particle on the right-hand region at the mid axis with different particle discretisations and fixed horizon size using the explicit and implicit methods, with numerically generated tangent stiffness are shown in Table 4.2 and 4.3. It can be seen from Table 4.2 that the total calculation time can be reduced up to 5 times for the implicit with numerically generated tangent stiffness compared to the explicit method with adaptive dynamic relaxation for a total number of particles of 63. The calculation time

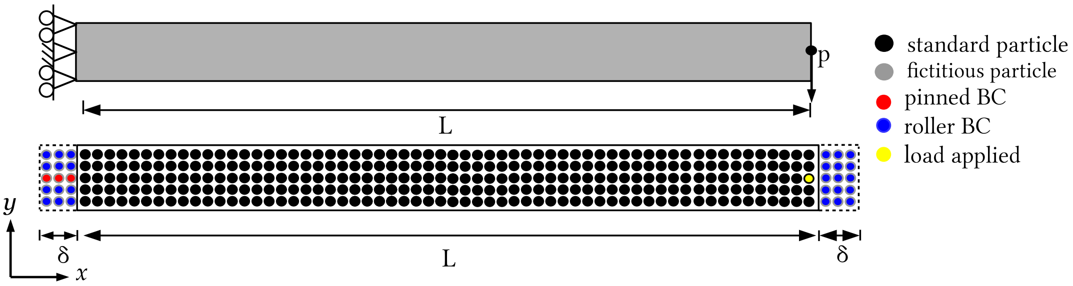

Figure 4.13: Cantilever beam subjected to vertical mid-side load.

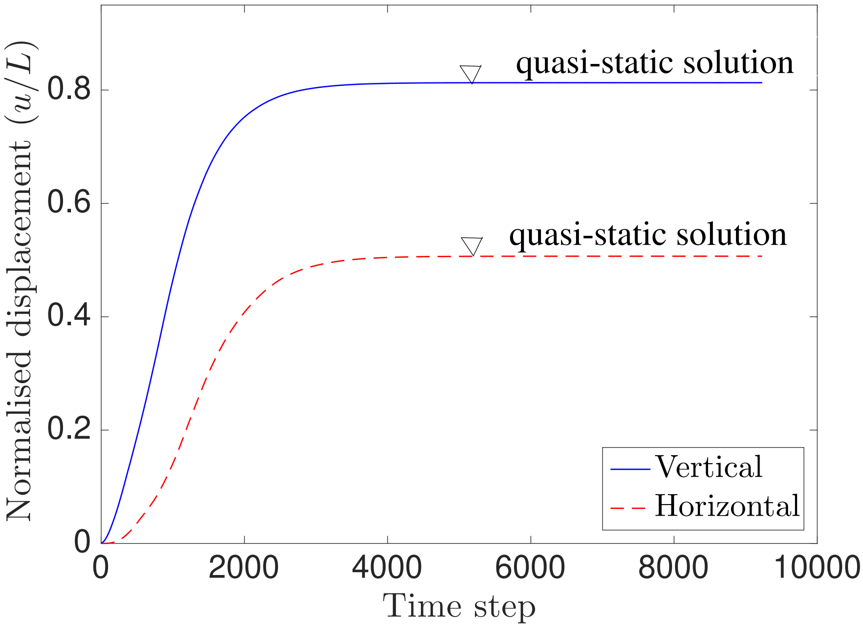

Figure 4.14: steady state solution for p=100 kN, $\delta = 1.015\Delta x$, 427 particles.

decreases when finer particle discretisations are used, where the total calculation time only reduced up to 2 times for the implicit method with numerically generated tangent stiffness compared to the explicit method with adaptive dynamic relaxation for the 427 particles. This shows that, as the accuracy increases, the solution cost for the implicit procedure increases more steeply than for the explicit procedure and at the same time, the implicit NOSB PD minimise the computational expense compared to the explicit NOSB PD. The displacement error up to three decimal places as shown in Table 4.3, where it can be clearly seen that the error was the same for all those methods and at the same time was reduced with the finer particle

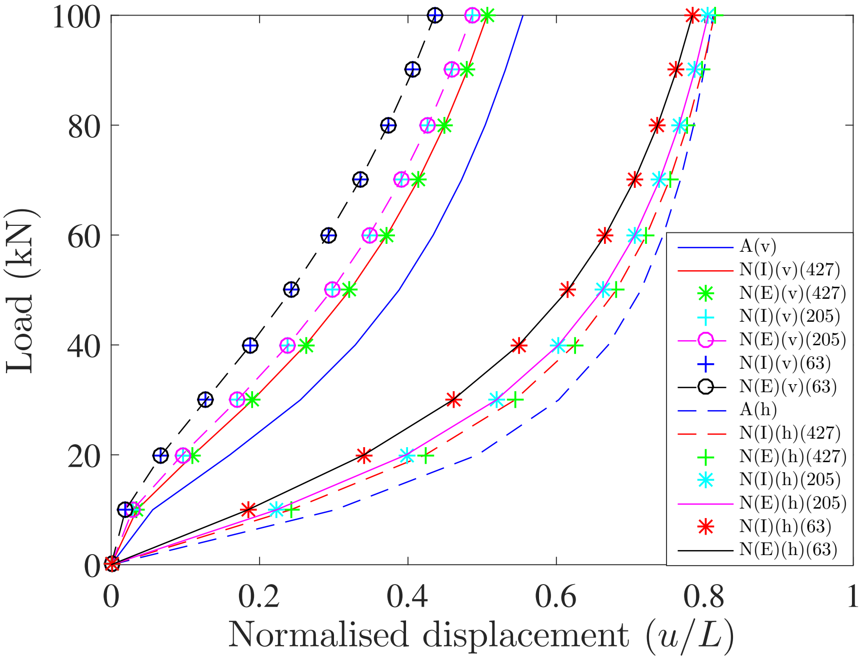

Figure 4.15: Normalised displacement.

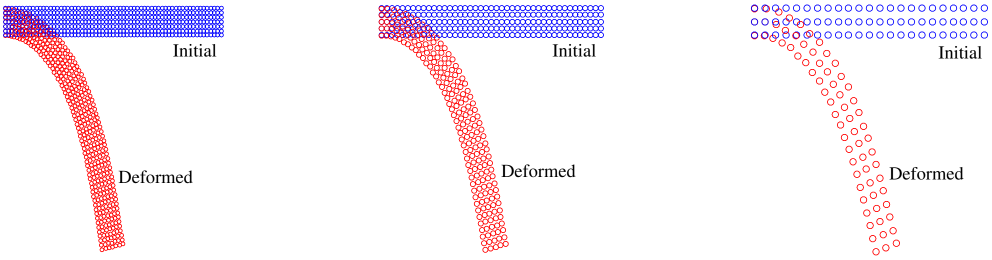

(a) Number of particles = 427 (b) Number of particles = 205 (c) Number of particles = 63

Figure 4.16: Initial and deformed (final) configuration for different particle discretisations with $\delta = 1.015\Delta x$.

discretisation. This was because the stopping criterion based on the static residual for explicit time step and tolerance for the implicit time step were prescribed at 1×10^{-6} a displacement relative error and 1×10^{-10} respectively.

The total calculation time and displacement relative error of the actual end particle on the right hand region at the mid axis with different horizon sizes, for the same particle discretisation (427) using the explicit and implicit methods with numerically generated tangent stiffness are shown in Table 4.4 and 4.5. It can be seen from Table 4.4 that the total calculation time can be reduced up to 3 times

Table 4.2: Calculation time with different particle discretisations for 10 loadsteps.

Number of particles	Total calculation time (minutes)	
	Explicit	Implicit
63	1.58×10^{1}	3.12×10^{0}
205	1.03×10^{2}	3.19×10^{1}
427	2.90×10^{2}	1.39×10^{2}

Table 4.3: Displacement relative error at the midpoint of the free end with different particle discretisations.

Number of particles	Displacement relative error (%)	
	Explicit	Implicit
63	3.418×10^{0}	3.418×10^{0}
205	8.015×10^{-1}	8.015×10^{-1}
427	2.466×10^{-1}	2.466×10^{-1}

for the implicit approach compared to the explicit method with adaptive dynamic relaxation for the horizon size, $\delta = 1.015\Delta x$. This calculation time ratio decreased when the larger horizon size was used. It can be seen from Table 4.5 that for this cantilever beam problem, finer discretisation with smaller horizon size is more stable and gives a smaller error. The use of horizon size, $\delta = 2.015\Delta x$ and $\delta = 3.015\Delta x$ however seems to be unstable for this problem and the reason is still unclear at the moment. Stress contour plots for the 427 particles analysis and $\delta = 1.015\Delta x$ corresponding to the external load of of 100 kN are shown in Figure 4.17 and the convergence for the final 5 load steps of the Newton Raphson process for the same analysis is given in Table 4.6 indicating it to be near quadratic as expected indicating a correct implementation.

Table 4.4: Calculation time with different horizon sizes for 10 loadsteps.

Horizon size	Total calculation time (minutes)	
	Explicit	Implicit
$\delta = 1.015\Delta x$	1.03×10^{2}	3.19×10^{1}
$\delta = 2.015\Delta x$	9.93×10^{1}	6.85×10^{1}
$\delta = 3.015\Delta x$	1.63×10^{2}	1.51×10^{2}

Table 4.5: Displacement relative error at the midpoint of the free end with different horizon sizes.

Horizon size	Displacement relative error (%)	
	Explicit	Implicit
$\delta = 1.015\Delta x$	8.015×10^{-1}	8.015×10^{-1}
$\delta = 2.015\Delta x$	1.402×10^{1}	1.402×10^{1}
$\delta = 3.015\Delta x$	9.827×10^{1}	9.827×10^{1}

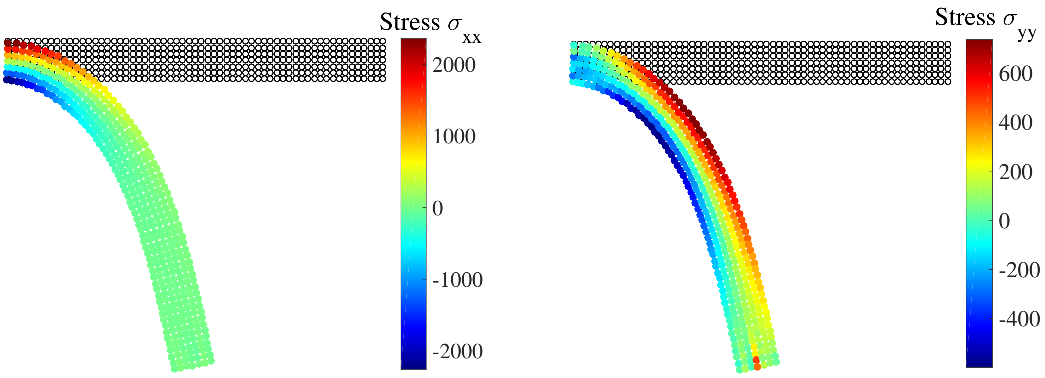

(a) σ_{xx} (b) σ_{yy}

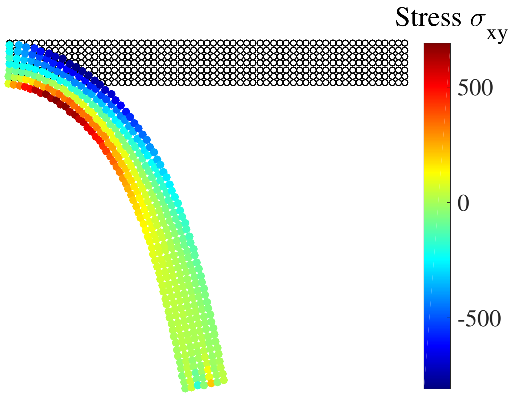

(c) σ_{xy}

Figure 4.17: Stress contour corresponding to the external load for p = 100 kN, $\delta = 1.015\Delta x$, 427 particles (a) σ_{xx}, (b) σ_{yy} and (c) σ_{xy} for the cantilever beam

Table 4.6: Newton Raphson residuals showing near-quadratic convergence ($tol = 1 \times 10^{-10}$).

Step	6	7	8	9	10
Iteration 1	3.16×10^{-1}	1.80×10^{-1}	1.09×10^{-1}	7.01×10^{-2}	4.72×10^{-2}
Iteration 2	1.80×10^{-3}	6.73×10^{-4}	3.97×10^{-4}	2.72×10^{-4}	1.85×10^{-4}
Iteration 3	1.60×10^{-3}	4.29×10^{-4}	1.12×10^{-4}	2.96×10^{-5}	8.09×10^{-6}
Iteration 4	6.65×10^{-8}	4.38×10^{-9}	2.30×10^{-10}	3.23×10^{-11}	4.55×10^{-12}
Iteration 5	4.34×10^{-12}	2.19×10^{-13}	1.96×10^{-13}	-	-

4.4.3 Simply-supported slender beam

A beam with the same material and geometric properties as the clamped elastic beam but having simply-supported ends was analysed using the same particle discretisations, but with appropriately modified boundary conditions at the support. As in the previous example of the clamped slender beam, a fictitious boundary layer, equivalent to the size of the horizon size was introduced outside the actual material domain at the boundary region, and displacement boundary conditions were imposed through the fictitious boundary layer. For the simply-supported beam, only one particle at the left-hand fictitious region of the middle surface is prevented from having in-plane displacement, and the edges must be free to rotate as shown in Figure 4.18. The problem was analysed using a loading increment of 27.6 kPa, applied in 10 loadsteps to a maximum loading of 276 kPa. Due to symmetry, only half of the beam was analysed and uniformly discretised into three difference particle discretisation with different horizon sizes, δ.

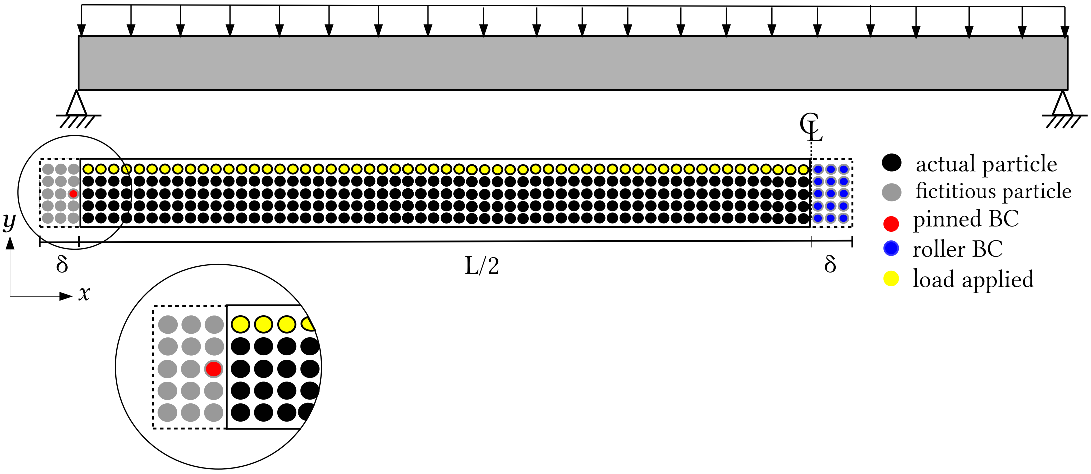

Figure 4.18: Simply-supported slender beam subjected to uniform transverse pressure.

The total calculation time for various particle numbers and horizon sizes are shown in Table 4.7. It was shown that the calculation time increases when the finer discretisation was used and at the same time, by using a larger horizon size, the computational time was also significantly larger. Finally, in Figure 4.19, the maximum normalised vertical displacement of the material is compared against the analytical result of the same problem for different particle discretisations with three different horizon sizes. It can be clearly seen that by changing the particle discretisation, the normalised vertical displacement converges towards the analytical value. However, when the horizon size was two and three times larger than the particle spacing, the vertical displacements do not converge to the actual solution with the 1057 particles. To address this, a modification on how the boundary condition was imposed would be necessary to approximate simply-supports with finer discretisation when preventing only one particle at the left-hand fictitious region of the middle surface from having in-plane displacement is not enough adequately to model the simply-supported boundary condition. Additional constraints would be necessary to implement the simply-supported condition as stated in [156]; however, the best way to model it is still unclear at the moment.

Table 4.7: Calculation time for 10 loadsteps and displacement relative error with different particle discretisations and different horizon sizes for the simply-supported slender beam.

Number of particles	δ	Total time (minutes)	Displacement relative error (%)
153	$1.015\Delta x$	3.38×10^0	3.715×10^0
	$2.015\Delta x$	1.14×10^1	6.018×10^0
	$3.015\Delta x$	2.417×10^1	1.873×10^1
505	$1.015\Delta x$	4.70×10^1	1.047×10^{-1}
	$2.015\Delta x$	1.13×10^2	4.516×10^0
	$3.015\Delta x$	2.63×10^2	1.12×10^1
1057	$1.015\Delta x$	2.09×10^2	1.085×10^0
	$2.015\Delta x$	3.10×10^2	5.185×10^1
	$3.015\Delta x$	6.83×10^2	1.461×10^2

The stress contour, σ_{xx} corresponding to the external load for p = 276 kN, $\delta = 1.015\Delta x$ and 1057 particles for the simply-supported slender beam was shown in Figure 4.20.

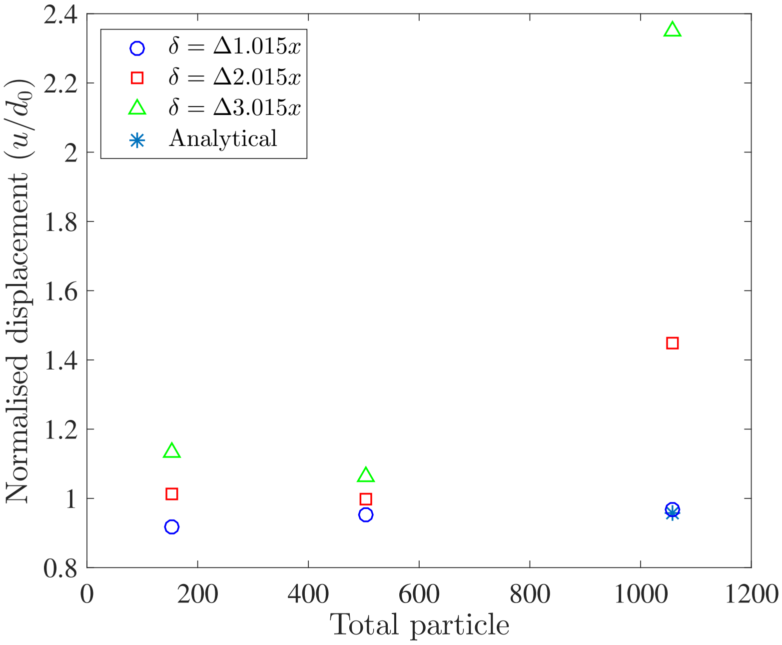

Figure 4.19: Physical convergence of verticle displacement with changing particle density and horizon sizes for simply-supported slender beam.

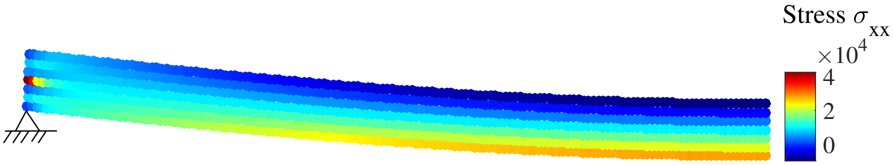

Figure 4.20: Stress contour, σ_{xx} corresponding to the external load for p = 276 kN, $\delta = 1.015\Delta x$, 1057 particles for the simply-supported slender beam

4.5 Observations

In this chapter, the development of NOSB PD with an implicit pseudo time integration scheme has been introduced. The global stiffness matrix based on the numerical expression of the equation of motion of NOSB PD was also explained. The method was then demonstrated with numerical examples to validate the effectiveness of this approach where analytical results exist, and it has been demonstrated that it can provide good results. Results from these examples show for a given particle spacing; a smaller horizon size shows greater accuracy with no control on the zero-energy modes. A comparison of implicit and explicit approaches for peridynamics in solid mechanics focusing on quasi-static problems with large deformations has been presented for the first time using the non-ordinary state-based framework. Both implicit and explicit methods predict the same response. However, implicit time integration with numerically generated tangent stiffness allows, compared to the techniques based on explicit dynamic relaxation, a reduced computational time. In the next chapter, the stabilised NOSB PD approach based on the analytically constructed tangent stiffness will be introduced.

Chapter 5

Implicit stabilised NOSB PD for large deformation analysis

In the previous chapter, the non-ordinary state-based peridynamics (NOSB PD) approaches based on a numerically constructed tangent for the simple 2D problem were presented. Although implicit methods are more complicated and challenging to implement, the advantages of the implicit method suggested include an allowance of much larger load steps, hence giving benefit in terms of its computational runtime especially for large deformation problems, in comparison to those based on explicit dynamic relaxation. However, due to the high computational time and high memory requirement to find the numerically tangent stiffness matrices, in this chapter, an implicit approach of NOSB PD for quasi-static problems with large deformation mechanics is presented with an analytically constructed tangent stiffness using a so-called correspondence material to address stability issues.

Recently, Silling has introduced a stabilised "correspondence" material model which satisfies the stability condition [12]. This stabilised correspondence material model has not been studied in the context of the elimination of zero-energy modes for large deformation or implicit NOSB PD, as described below. The layout of the chapter is as follows: Section 5.1 details the numerical implementation of developing the Jacobian matrices of the NOSB PD with a correspondence continuum models for both the unstabilised and stabilised versions [12]. Furthermore, the numerical examples are demonstrated in Section 5.2, and the accuracy is assessed with the inclusion of different stabilisation parameters, and finally, the chapter review is drawn in Section 5.3.

5.1 Non-linear solution procedure

In this section, a detailed implementation of a geometrically non-linear implicit NOSB PD method is provided. A full Newton-Raphson (NR) method is utilised in this chapter in order to solve the non-linear system of equations and update the Jacobian matrix at each iteration. The Jacobian matrix is recomputed at each iteration, thus enabling convergence at a higher rate than other alternatives [157].

5.1.1 Jacobian matrix

The Jacobian matrix or so-called tangent stiffness matrix can be constructed via analytical and numerical approaches. Eqs. 4.7 and 4.8 are here reproduced for the reader's convenience. It is possible to express the Jacobian matrix as follows

$$\mathbf{K} = \sum_{i}^{I_n} \sum_{j=1}^{m} \sum_{k}^{ndof} \left(\omega_i(|\boldsymbol{\xi}|) \frac{\partial \underline{\mathbf{T}}[\mathbf{x}_i]}{\partial \mathbf{u}_k} \right) - \left(\omega_j(|\boldsymbol{\xi}|) \frac{\partial \underline{\mathbf{T}}[\mathbf{x}_j]}{\partial \mathbf{u}_k} \right), \tag{5.1}$$

which can be expressed in matrix form as

$$\mathbf{K} = \begin{bmatrix} \frac{\sum_{j=1}^{m} \left(\omega_1(|\boldsymbol{\xi}|) \partial \underline{\mathbf{T}}[\mathbf{x}_1] \right) - \left(\omega_j(|\boldsymbol{\xi}|) \partial \underline{\mathbf{T}}[\mathbf{x}_j] \right)}{\partial u_1} & \cdots & \frac{\sum_{j=1}^{m} \left(\omega_1(|\boldsymbol{\xi}|) \partial \underline{\mathbf{T}}[\mathbf{x}_1] \right) - \left(\omega_j(|\boldsymbol{\xi}|) \partial \underline{\mathbf{T}}[\mathbf{x}_j] \right)}{\partial u_{ndof}} \\ \vdots & \ddots & \vdots \\ \frac{\sum_{j=1}^{m} \left(\omega_{I_n}(|\boldsymbol{\xi}|) \partial \underline{\mathbf{T}}[\mathbf{x}_{I_n}] \right) - \left(\omega_j(|\boldsymbol{\xi}|) \partial \underline{\mathbf{T}}[\mathbf{x}_j] \right)}{\partial u_1} & \cdots & \frac{\sum_{j=1}^{m} \left(\omega_{I_n}(|\boldsymbol{\xi}|) \partial \underline{\mathbf{T}}[\mathbf{x}_{I_n}] \right) - \left(\omega_j(|\boldsymbol{\xi}|) \partial \underline{\mathbf{T}}[\mathbf{x}_j] \right)}{\partial u_{ndof}} \end{bmatrix}. \tag{5.2}$$

Substituting Eq. (3.16) into Eq. (4.7), it is possible to write the Jacobian as

$$\mathbf{K} = \sum_{i}^{I_n} \sum_{j=1}^{m} \sum_{k}^{ndof} \left(\omega_i(|\boldsymbol{\xi}|) \frac{\partial \mathbf{P}_i}{\partial \mathbf{F}_i} \frac{\partial \mathbf{F}_i}{\partial \mathbf{u}_k} \mathbf{B}_i \left(\mathbf{x}_j - \mathbf{x}_i \right) \right) - \left(\omega_j(|\boldsymbol{\xi}|) \frac{\partial \mathbf{P}_j}{\partial \mathbf{F}_j} \frac{\partial \mathbf{F}_j}{\partial \mathbf{u}_k} \, \mathbf{B}_j \left(\mathbf{x}_i - \mathbf{x}_j \right) \right) V_j. \tag{5.3}$$

Note that the stiffness of a particle depends on all of the particles that the particle is connected to and those that the connected particles are connected to. In (5.3), the derivative of the first Piola-Kirchhoff stress with respect to the deformation gradient can be written as

$$\begin{aligned}\mathbf{A} &= \frac{\partial \mathbf{P}}{\partial \mathbf{F}} \\ &= \frac{\partial \boldsymbol{\tau}}{\partial \mathbf{F}}\mathbf{F}^{-T} + \boldsymbol{\tau}\frac{\partial \mathbf{F}^{-T}}{\partial \mathbf{F}},\end{aligned} \tag{5.4}$$

where **A** denotes the material tangent modulus, often referred to as the first elasticity tensor for materials with an elastic constitutive law. For the sake of brevity, the complete derivation of **A** is not included here (see Appendix A for the full derivation). Combining the derivative of the Kirchhoff stress with respect to the elastic logarithmic strain tensor, **Q**, the stiffness matrix for isotropic linear elasticity, $\mathbf{D}^e$ and the derivative of the Cauchy-Green strain with respect to the deformation gradient, **N**, the following equation for the spatial tangent stiffness matrix, **M** in the first term of the right-hand side of Eq.(5.4) is obtained where

$$\mathbf{M} = \mathbf{Q}\mathbf{D}^e\mathbf{N}, \tag{5.5}$$

$$\mathbf{Q} = \frac{\partial \boldsymbol{\epsilon}}{\partial \mathbf{c}} = \frac{1}{2}\frac{\partial ln(\mathbf{c})}{\partial \mathbf{c}}, \tag{5.6}$$

and

$$\mathbf{N} = \frac{\partial \mathbf{c}}{\partial \mathbf{F}}. \tag{5.7}$$

Turning the focus to the formulation of the derivative of the deformation gradient with respect to the displacement in Eq.(5.3),

$$\mathbf{H} = \frac{\partial \mathbf{F}}{\partial \mathbf{u}_k} = \begin{bmatrix} \sum_{j=1}^{m} \omega\langle\boldsymbol{\xi}\rangle(\frac{\partial \underline{Y}(\xi_x)}{\partial \mathbf{u}_k})\xi_x V_j & \sum_{j=1}^{m} \omega\langle\boldsymbol{\xi}\rangle(\frac{\partial \underline{Y}(\xi_x)}{\partial \mathbf{u}_k})\xi_y V_j \\ \sum_{j=1}^{m} \omega\langle\boldsymbol{\xi}\rangle(\frac{\partial \underline{Y}(\xi_y)}{\partial \mathbf{u}_k})\xi_x V_j & \sum_{j=1}^{m} \omega\langle\boldsymbol{\xi}\rangle(\frac{\partial \underline{Y}(\xi_y)}{\partial \mathbf{u}_k})\xi_y V_j \end{bmatrix}\mathbf{B}^{-1}. \tag{5.8}$$

Substituting Eq.(5.8) and Eq.(5.4) into Eq.(4.7) leads to the construction of the global tangent stiffness as shown in Figure 5.1.

5.1.2 Stabilised NOSB PD

So-called correspondence material models allow a material model from standard local theory to model long-range forces with the inherent capabilities of nonlocal PD formulation. However, in a uniform particle discretisation, correspondence models suffer from instability due to zero-energy modes. In the context of the NOSB PD formulation, spurious zero-energy modes are attributed to the weak couplings between particles within a horizon and this causes stability issues which have been reported in [77, 111, 115, 134]. In the presence of zero-energy modes, simulations exhibit oscillations in the deformation and stress fields. This is caused by the missing role of the centre particle when approximating the deformation gradient tensor, and all correspondence materials fail this stability condition [12]. In order to understand its origin, imagine a particle $\mathbf{x}$ with a circular horizon R which is subject to displacement as shown in Figure 5.2, resulting in an additional vector $\mathbf{u}$ while the displacement of other particles are kept constant, the new deformation vector-state is

$$\underline{\mathbf{Y}}_{\mathrm{z}}\langle\boldsymbol{\xi}\rangle = \underline{\mathbf{Y}}\langle\boldsymbol{\xi}\rangle - \mathbf{u}. \tag{5.9}$$

The new deformation gradient $\mathbf{F}_{\mathrm{z}}(\mathbf{x})$ is calculated based on Eq. (3.18) as

$$\mathbf{F}_{\mathrm{z}}(\mathbf{x}) = \mathbf{F}(\mathbf{x}) - \mathbf{u} \otimes \left(\int_R \omega\langle\boldsymbol{\xi}\rangle\boldsymbol{\xi} dV_{\boldsymbol{\xi}} \right) \mathbf{B}(\mathbf{x})^{-1}. \tag{5.10}$$

i	1	2	I_n	FOR EACH Particle		
j	1	2	$....m$	FOR EACH Neighbouring Particle		
$\mathbf{L}$				particle internal force	$\mathbf{L}(\mathbf{x}_i) = \sum_{j=1}^{m}(\underline{\mathbf{T}}\left[\mathbf{x}_i, t\right] - \underline{\mathbf{T}}\left[\mathbf{x}_j, t\right])V_j$	(3.11)
				END FOR		
$\mathbf{Q}$				derivative of logarithmic elastic strain with respect to the left Cauchy-Green strain	$\mathbf{Q}(\mathbf{x}_i) = \frac{1}{2}\frac{\partial \ln \mathbf{c}(\mathbf{x}_i)}{\partial \mathbf{c}(\mathbf{x}_i)}$	(A.1.3)
$\mathbf{N}$				derivative of Cauchy-Green strain with respect to the deformation gradient	$\mathbf{N}(\mathbf{x}_i) = \frac{\partial \mathbf{c}(\mathbf{x}_i)}{\partial \mathbf{F}(\mathbf{x}_i)}$	(A.1.5)
$\mathbf{M}$				spatial tangent stiffness matrix	$\mathbf{M}(\mathbf{x}_i) = \mathbf{D}^e\mathbf{Q}(\mathbf{x}_i)\mathbf{N}(\mathbf{x}_i)$	(A.1.2)
$\mathbf{A}$				derivative of Piola Kirchhoff with respect to the deformation gradient	$\mathbf{A}(\mathbf{x}_i) = \frac{\partial(\tau \mathbf{F}^{-T}(\mathbf{x}_i))}{\partial \mathbf{F}(\mathbf{x}_i)}$	(5.4)
$\mathbf{H}$				derivative of deformation gradient with respect to the displacement	$\mathbf{H}(\mathbf{x}_i) = \sum_{j=1}^{m} \omega\langle\boldsymbol{\xi}\rangle\left(\frac{\partial \underline{Y}(\boldsymbol{\xi})}{\partial u} \otimes \boldsymbol{\xi}\right)V_j$	(5.3)
k	1	2	$....ndof$	FOR EACH Degree-of-freedom		
$\mathbf{K}$					$\mathbf{K} = \sum_{k}^{ndof}\left(\omega_i(\lvert\boldsymbol{\xi}\rvert)\frac{\partial \underline{\mathbf{T}}[\mathbf{x}_i]}{\partial \mathbf{u}_k}\right) - \left(\omega_j\langle\boldsymbol{\xi}\rangle\frac{\partial \underline{\mathbf{T}}[\mathbf{x}_j]}{\partial \mathbf{u}_k}\right)$	(4.7)
				END FOR		
				END FOR		

Figure 5.1: NOSB PD large deformation algorithm sequence where i denotes the particle number, j denotes the neighbouring particles and k denotes the degree of freedom number.

With the assumption of a circular neighbourhood, R, and a regular lattice of particles, the integration term on the right-hand side of Eq. (5.10) will vanish, and thus $\mathbf{F}_z(\mathbf{x}) = \mathbf{F}(\mathbf{x})$. This shows that the additional displacement of particle $\mathbf{x}$ does not change the deformation gradient or the associated force-vector state. Various methods have been proposed in order to alleviate this problem.

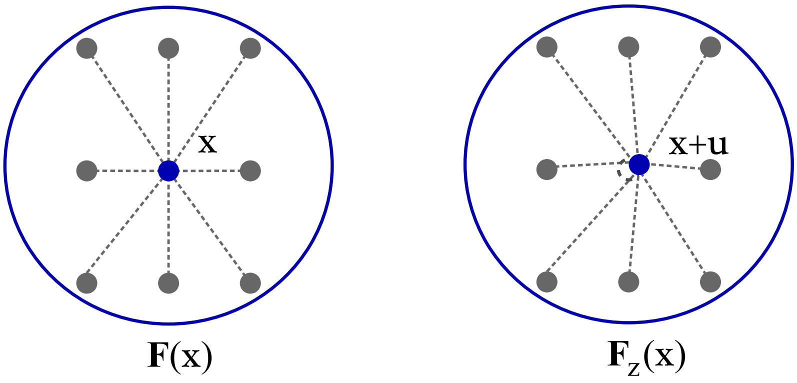

Figure 5.2: An illustration of zero-energy modes where $\mathbf{F}(\mathbf{x}) = \mathbf{F_z}(\mathbf{x})$.

Note that recent contributions have included initial attempts to alleviate zero-energy modes (refer to Section 2.2.2). Recently, an attempt has been made by Silling [12] to eliminate the zero-energy modes by adding a term to the corresponding strain energy density. This approach considers the root of the problem as a material instability, rather than a numerical instability[12]. In this approach the force vector-state is given by

$$\underline{\mathbf{T}}\langle\boldsymbol{\xi}\rangle = \omega(|\boldsymbol{\xi}|)[\sigma^0(\mathbf{F})]^T \cdot \mathbf{B}(\mathbf{x}) \cdot \boldsymbol{\xi} + \underline{\mathbf{T}}_z\langle\boldsymbol{\xi}\rangle. \tag{5.11}$$

The additional stabilisation term added to the PD force vector defined as

$$\underline{\mathbf{T}}_z\langle\boldsymbol{\xi}\rangle = \frac{GC}{\omega_0}\underline{\mathbf{z}}(\boldsymbol{\xi}), \tag{5.12}$$

in which G is a stabilisation parameter whose value will be explored in the numerical examples. It should be noted that parameter, G should be a constant positive number of the order of 1 [12] and C is the nominal micromodulus, stated in [120] as

$$C = \frac{12k'}{\pi h \delta^4}, \tag{5.13}$$

for 2D problems in which k' is

$$k' = \begin{cases} \frac{E}{2(1-\nu)} & \text{plane stress} \\ \frac{E}{2(1-\nu-2\nu^2)} & \text{plane strain.} \end{cases} \tag{5.14}$$

For the 2D case, h is the out-of-plane thickness and ω_0 is the integration of the weighting function in the neighbourhood

$$\omega_0 = \int_R \omega(|\boldsymbol{\xi}|) dV_j, \tag{5.15}$$

where V_j is the volume of neighbouring particles in the reference configuration. The remaining term, $\underline{\mathbf{z}}(\boldsymbol{\xi})$ is defined in [12] as

$$\underline{\mathbf{z}}(\boldsymbol{\xi}) = \underline{\mathbf{Y}}(\boldsymbol{\xi}) - \mathbf{F}\boldsymbol{\xi}, \tag{5.16}$$

which represents the state of deformation that deviates from the uniform deformation of the neighbouring particles. It can be seen that the approximate deformation gradient disappears, when the non-uniform part is included in its approximation of a deformation state [12]

$$\begin{aligned} \left(\int_R \omega(|\boldsymbol{\xi}|) \underline{\mathbf{z}}(\boldsymbol{\xi}) \otimes \boldsymbol{\xi} dV_{\boldsymbol{\xi}} \right) \mathbf{B}^{-1} &= \left(\int_R \omega(|\boldsymbol{\xi}|) \underline{\mathbf{Y}}(\boldsymbol{\xi}) - \mathbf{F}\boldsymbol{\xi}(\boldsymbol{\xi}) \otimes \boldsymbol{\xi} dV_{\boldsymbol{\xi}} \right) \mathbf{B}^{-1} \\ &= \left(\int_R \omega(|\boldsymbol{\xi}|) \underline{\mathbf{Y}}(\boldsymbol{\xi}) \otimes \boldsymbol{\xi} dV_{\boldsymbol{\xi}} \right) \mathbf{B}^{-1} \\ &- \mathbf{F} \left(\int_R \omega(|\boldsymbol{\xi}|) \, \boldsymbol{\xi} \otimes \boldsymbol{\xi} dV_{\boldsymbol{\xi}} \right) \mathbf{B}^{-1} \\ &= \mathbf{F} - \mathbf{F}\mathbf{B}\mathbf{B}^{-1} \\ &= 0. \end{aligned} \tag{5.17}$$

In this chapter, this stabilised correspondence material model is used in the numerical examples to alleviate the zero-energy mode problem. With the additional stabilisation term added to the internal force, the new Jacobian can be expressed as [158]

$$\mathbf{K} = \sum_{i}^{I_n} \sum_{j=1}^{m} \sum_{k}^{ndof} \left(\omega_i(|\boldsymbol{\xi}|) \frac{\partial \underline{\mathbf{T}}[\mathbf{x}_i, t]}{\partial \mathbf{u}_k} + \frac{GC}{\omega_0} \left(\frac{\partial \underline{\mathbf{Y}}\langle \mathbf{x}_j - \mathbf{x}_i \rangle}{\partial \mathbf{u}_k} - \frac{\partial \mathbf{F}(\mathbf{x}_i)}{\partial \mathbf{u}_k} (\mathbf{x}_j - \mathbf{x}_i) \right) \right) - \\ \left(\omega_j(|\boldsymbol{\xi}|) \frac{\partial \underline{\mathbf{T}}[\mathbf{x}_j, t]}{\partial \mathbf{u}_k} + \frac{GC}{\omega_0} \left(\frac{\partial \underline{\mathbf{Y}}\langle \mathbf{x}_i - \mathbf{x}_j \rangle}{\partial \mathbf{u}_k} - \frac{\partial \mathbf{F}(\mathbf{x}_j)}{\partial \mathbf{u}_k} (\mathbf{x}_i - \mathbf{x}_j) \right) \right). \tag{5.18}$$

5.2 Numerical Examples

Four examples are presented here to demonstrate the proposed stabilised implicit NOSB PD formulation. The first example comprises a square plate under hydrostatic extension and is used to demonstrate the effect of the stabilisation parameter, G. The second and third examples apply the stabilised model to clamped and simply-supported beams respectively, and the last example models the very large deformation of a cantilever beam subjected to a vertical load at its free end. These latter examples are used to demonstrate the effect of the stabilisation parameter, G with different particle spacing and horizon size.

5.2.1 Hydrostatic extension

The first example is a 2D square plate under hydrostatic extension. In the analysis a plane strain condition is assumed in the third direction. The square plate had an initial length of $l_0 = 1$m, shown in Figure 5.3 (a) and was fixed at the middle particle. The material model was isotropic linear elasticity with a Young's modulus of $E = 1.2$ MPa, and a Poisson's ratio of $\nu = 0.2$. The plate was uniformly discretised into 625 particles (arranged in a 25 × 25 regular grid) with horizon size of $\delta = 1.015\Delta x$, $\delta = 2.015\Delta x$ and $\delta = 3.015\Delta x$. A total traction of 5000 kN/m^2 was applied at each side of the plate in a single loadstep as shown in Figure 5.4. The final configuration is shown in Figure 5.3 (b) for the case of $\delta = 2.015\Delta x$ and $G = 1$, clearly demonstrating large deformation (red and blue represent the initial and final configurations, respectively). The analytical deformation gradient and logarithmic strain for this problem are

$$[\mathbf{F}] = \begin{bmatrix} l/l_0 & 0 \\ 0 & l/l_0 \end{bmatrix} \quad \text{and} \quad [\boldsymbol{\epsilon}] = \ln \begin{bmatrix} l/l_0 & 0 \\ 0 & l/l_0 \end{bmatrix}. \tag{5.19}$$

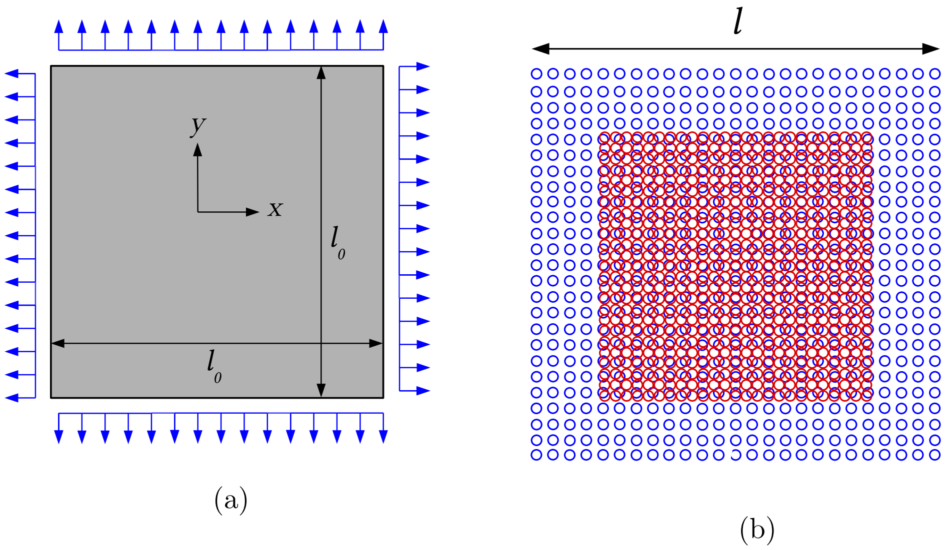

(a)

(b)

Figure 5.3: Hydrostatic extension: (a) problem definition and (b) initial (red) and final (blue) configurations with $\delta = 2.015\Delta x$ and $G = 1$.

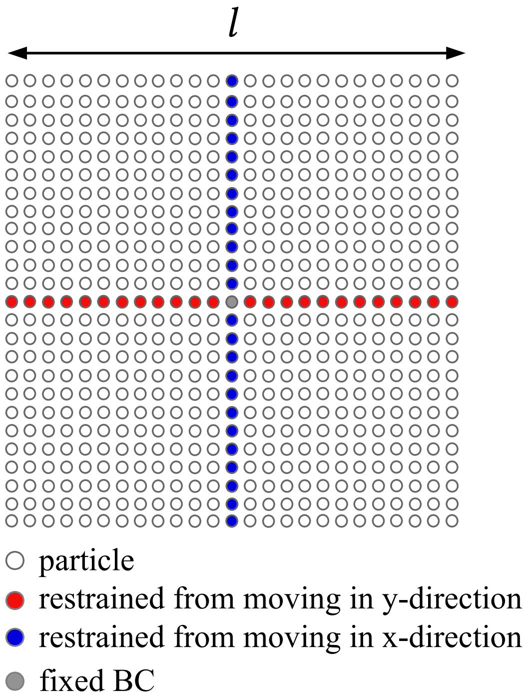

Figure 5.4: Hydrostatic expansion: displacement BC.

From the analytical solution given in Eq. (5.19), the displacement normal to each side of the plate was calculated to be 0.30667 m (the deformed length of the plate at the end of the analysis should be $l = 1.61334$ m). The displacement error, e_u is calculated as

$$e_u = \frac{1}{V} \sum_{i}^{I_n} \left(\frac{|\mathbf{u}_p - \mathbf{u}|}{|\mathbf{u}|} V_i \right), \tag{5.20}$$

where $\mathbf{u}$ is the displacement calculated from the analytical solution. Figure 5.5 shows the dependence of the displacement error based on G for different horizon sizes, δ and normalised particle spacing $\Delta x/\mathrm{L}$. It is clear that the PD solution's error decreases with increasing G values, achieving a minimum error before it rises for higher coefficient values, where the solution is controlled by the correction time. The larger horizon size increases the effects of the zero-energy modes in that a larger stabilisation parameter is needed to minimise the error. For $\delta = 1.015\Delta x$, the G values only need to be as large as 0.01 in order to obtain the minimum error. In addition, the results shown in Figure 5.5 illustrate a larger relative error of displacement as the particle spacing becomes larger. For $\delta = 3.015\Delta x$ with $\Delta x/\mathrm{L} =$

0.04, the error of displacement are evident, indicating the necessity of zero-energy modes control.

Figure 5.6 shows the convergence rate for simulations, which varies between 0.43 and 0.91 depending on the number of particles and the horizon size. It can be clearly seen that varying the number of particles and horizon sizes has an impact on the path to the solutions to this problem.

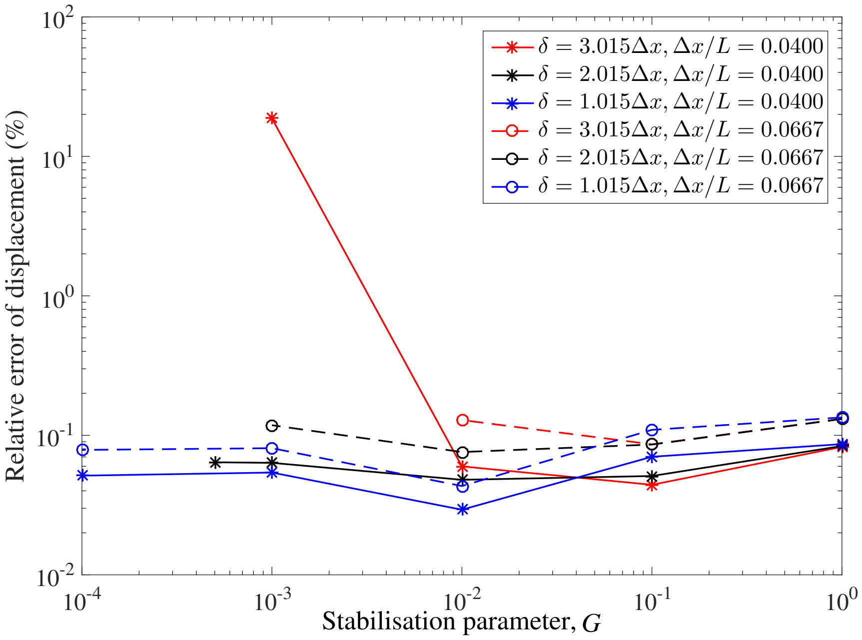

Figure 5.5: Hydrostatic expansion: relative displacement error with G for different δ and Δx/L .

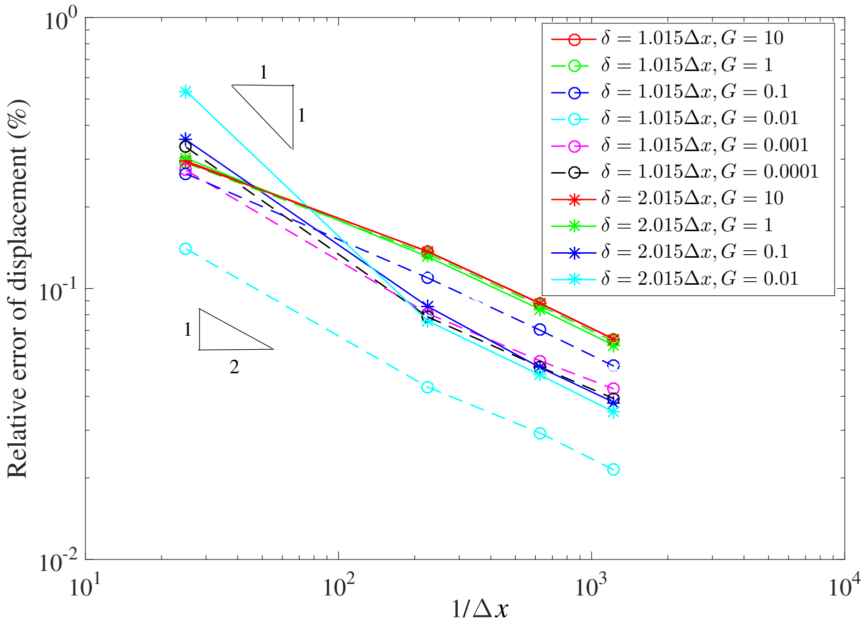

Figure 5.6: Hydrostatic expansion: convergence with $\delta = 1.015\Delta x$ and $\delta = 2.015\Delta x$ and different values of the stabilisation parameter, G.

5.2.2 Clamped slender beam subjected to a uniform transverse pressure

The second problem considered was the behaviour of a slender beam subjected to a uniform transverse pressure of p = 276 kPa applied in 10 loadsteps. The beam domain at the beginning had a length, L of 254 mm and a depth, d_0 of 5.08 mm, Young's modulus of $E = 68.95$ GPa and Poisson's ratio of $\nu = 0.25$. Due to symmetry, only half of the beam was analysed and it was uniformly discretised into two different particle discretisations. To further quantify the effectiveness of G, three different horizon sizes of $\delta = 1.015\Delta x$, $\delta = 2.015\Delta x$ and $\delta = 3.015\Delta x$ and different values of the stabilisation parameter were explored. In order to implement a clamped boundary condition, a fictitious boundary layer was introduced outside the actual material domain at the boundary region where the size of the layer was equivalent to the horizon size and displacement boundary conditions (BC) were imposed throughout the fictitious boundary layer. As can be seen in Figure 5.7, the beam was fixed at the fictitious boundary region at the mid-axis in both directions and the roller boundary conditions applied to other particles along the left hand fictitious region, allowing the structure to move only in the y-direction in this location as shown in Figure 5.7. A uniform transverse pressure was applied to all the particles on the top surface. A tolerance of 1×10^{-10} was used on the global normalised out-of-balance force for unstabilised ($G = 0$) and stabilised ($G > 0$) correspondence material.

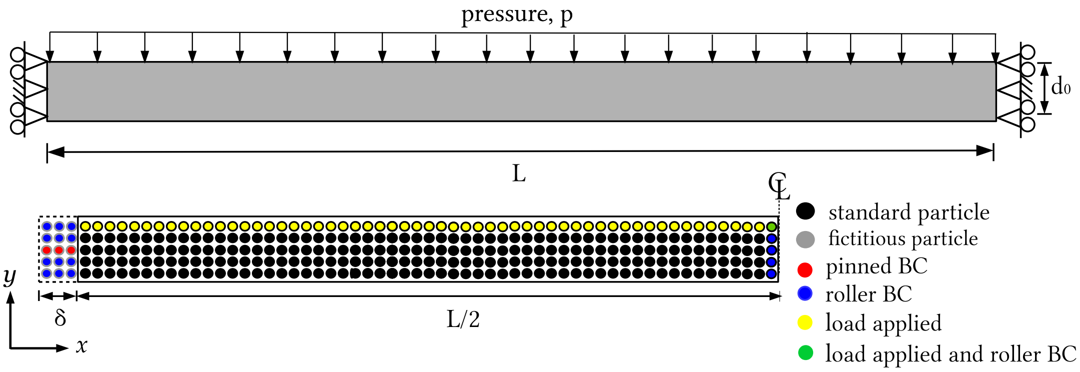

Figure 5.7: Clamped slender beam subjected to uniform pressure, p.

In Figures 5.8 and 5.9, the final normalised vertical displacement of the material is compared against the analytical solution of the same problem [155] for two different particle discretisations; 3 × 75 particles and 5 × 125 particles with different horizon sizes and different values of G. For a given particle spacing, the displacement obtained shows larger departures from the analytical solution in the absence of zero-energy control ($G = 0$) as the horizon size increases, as shown in Figures 5.8 and 5.9, while the smallest horizon size of one particle spacing used in this problem, minimises the effects of zero-energy modes.

The relative displacement errors, e_u are given for both particle discretisations and different horizon sizes for unstabilised material in Table 5.1. As can be seen, there are significant differences ($e_u = 6.678\times10^0$ for $\delta = 1.015\Delta x$, $e_u = 2.733\times10^1$ for $\delta = 2.015\Delta x$ and $e_u = 6.380\times10^1$ for $\delta = 3.015\Delta x$) between the three horizon sizes with 3 × 75 particles. It is seen that as the horizon size increases, the errors increase. These numerical results are in general agreement with observation published in [77, 115], in which it was demonstrated that the resulting axial displacement and stress show significant instabilities and errors as the horizon size increases in the absence of zero-energy control. This behaviour could be due to larger horizon sizes, where a larger number of bonds are connected to each particle which leads to an increase in the nonuniform part of the deformation state, with the missing role of the centre particle. Hence, it is expected that larger stabilisation term may need to be added to the force state in order to be effective at suppressing zero-energy, indicating that G must be adjusted based on the horizon size. However, continuing to increase the value of G results in an eventual increase of stiffness, thus artificially affecting the displacement as seen in both Figures 5.8 and 5.9.

Comparing the results in Figures 5.8 and 5.9, it can be seen that with the finer particle discretisation in Figure 5.9, the error for an unstabilised material ($G = 0$) is smaller than those in Figure 5.8 for all horizon sizes. Therefore using simulations with smaller particle spacings is a possible way to decrease the zero-energy mode oscillation although it significantly reduces the computational efficiency. Clearly, the discretisation scheme (i.e the particle arrangement) plays an important role in selecting the optimum value of G. Therefore, the smaller particle spacings were used, the smaller value of stabilised parameter, G will be needed.

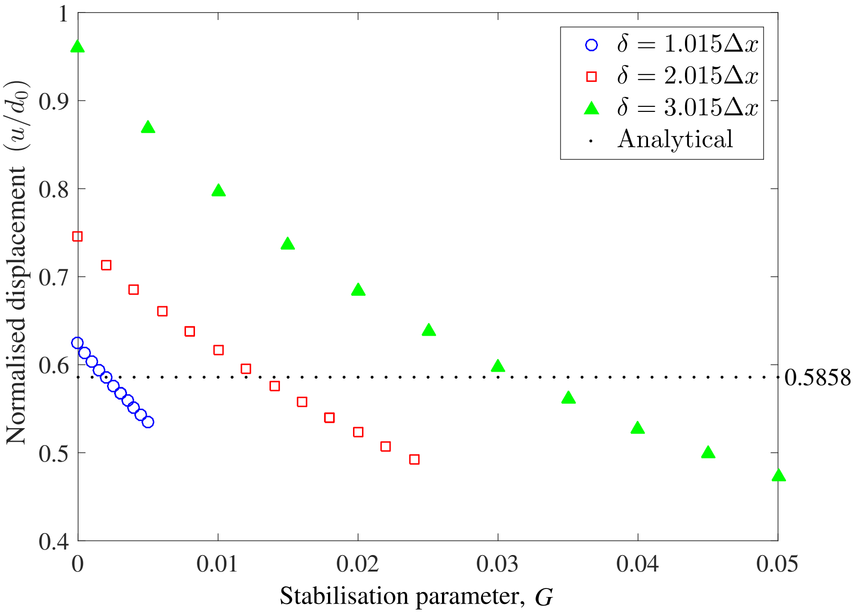

Figure 5.8: Clamped beam: normalised vertical displacement with changing G values and horizon sizes with 3 × 75 particles.

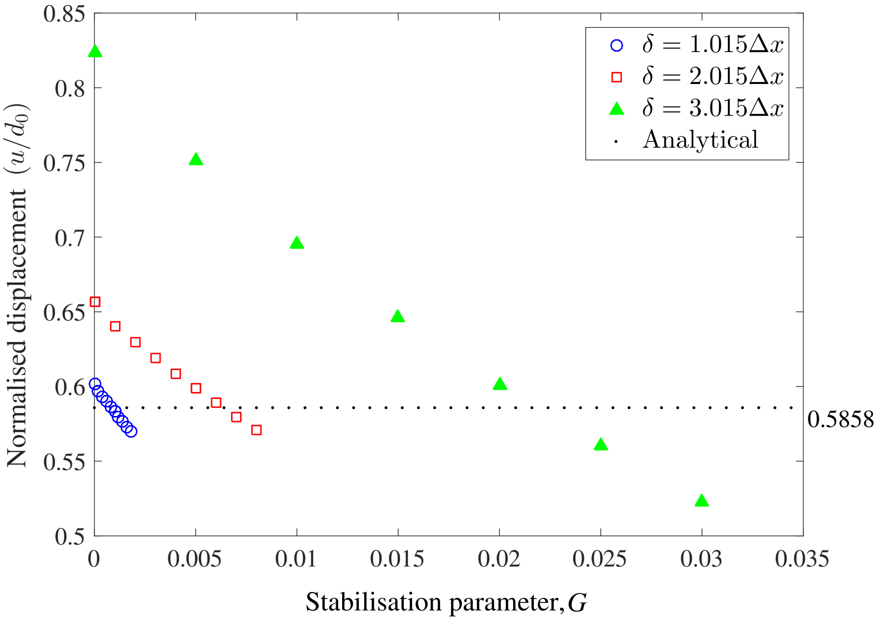

Figure 5.9: Clamped beam: normalised vertical displacement with changing G values and horizon sizes with 5×125 particles.

Figure 5.10 shows the error against computational time for the implicit approach developed in this paper alongside that of an explicit implementation using dynamic relaxation to achieve a pseudo static result. In this case the horizon size was set to $\delta = 1.015\Delta x$, $G = 0$ and the particle discretisation was varied. The errors and timings are for a uniform pressure of p = 276 kPa applied over 10 loadsteps. The results show that for a given discretisation, both methods predict the same response, with the same relative displacement error. The figure also show that the implicit time integration has a significantly reduced computational time. This is due to the number of iterations required by the explicit algorithm to achieve a pseudo static, or steady state, response.

In Figure 5.11, the maximum normalised vertical displacement of the material is compared against the analytical solution of the same problem with 3×75 particles and three different horizon sizes with an “optimum” stabilisation parameter, $G = 0.002$ with $\delta = 1.015\Delta x$, $G = 0.013$ with $\delta = 2.015\Delta x$ and $G = 0.031$ with $\delta = 3.015\Delta x$. The results using the NOSB PD are presented alongside the analytical solution of Molstad [155]. In all cases excellent agreement is seen between the NOSB PD normalised vertical displacement with the analytical result.

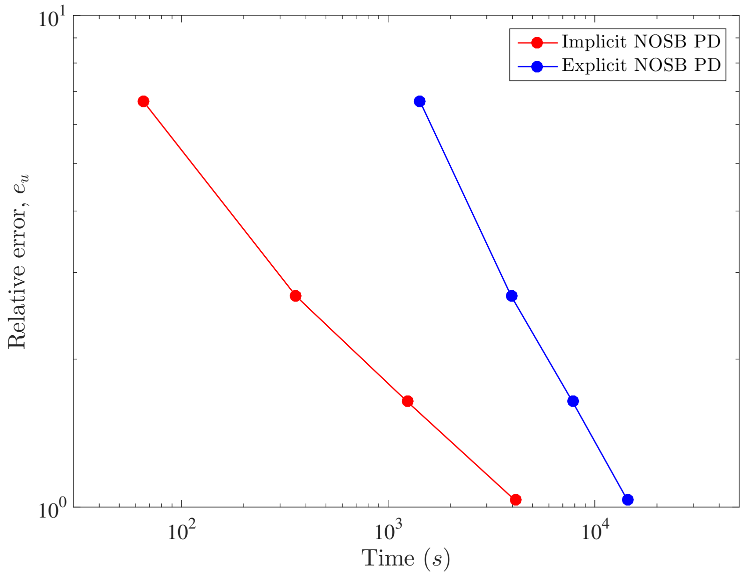

Figure 5.10: Clamped beam: displacement error versus time for implicit and explicit NOSB PD.

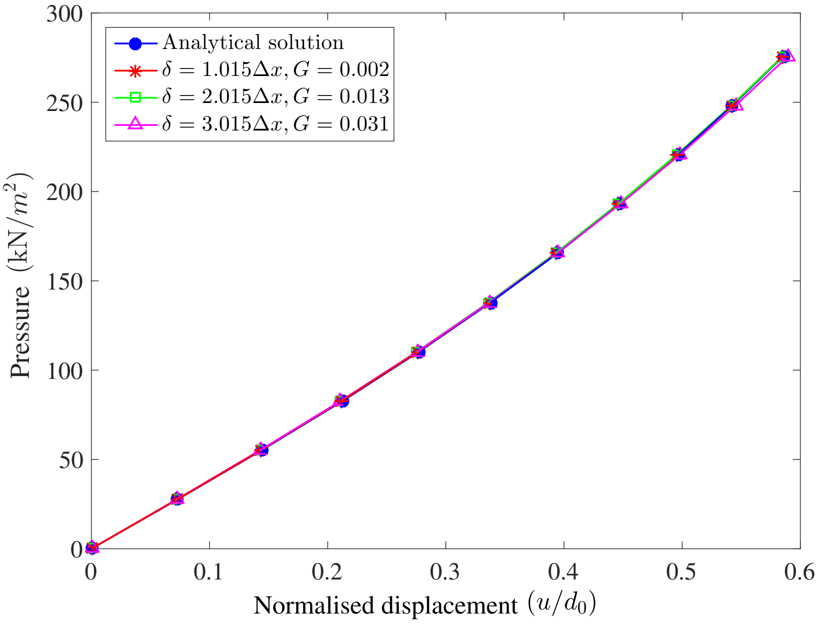

Figure 5.11: Clamped beam: normalised midpoint vertical displacements with 3×75 particles and different δ.

Table 5.1: Clamped beam: Relative displacement error with different particle discretisations and different horizon sizes for $G = 0$.

Particles discretisation	Horizon size, δ	Relative displacement error (%)
3 × 75	$1.015\Delta x$	6.678×10^{0}
	$2.015\Delta x$	2.733×10^{1}
	$3.015\Delta x$	6.380×10^{1}
5 × 125	$1.015\Delta x$	2.683×10^{0}
	$2.015\Delta x$	1.216×10^{1}
	$3.015\Delta x$	4.050×10^{1}

Figure 5.2 presents the global Newton-Raphson (NR) residual for the final 5 steps with 3 × 75 particles and $\delta = 3.015\Delta x$ and a global tolerance of 1×10^{-10}. Notable in Figure 5.2 is that the data shows near quadratic and a maximum number of iterations of 4, indicating the correct derivation and implementation of the Jacobian matrix and this is a point of novelty of the thesis.

Table 5.2: Clamped beam: Newton-Raphson residuals showing near-quadratic convergence ($tol = 1 \times 10^{-10}$) with $\delta = 3.015\Delta x$ and $G = 0.031$.

Step	6	7	8	9	10
Iteration 1	4.781×10^{-2}	3.680×10^{-2}	2.890×10^{-2}	2.313×10^{-2}	1.871×10^{-2}
Iteration 2	4.799×10^{-5}	3.805×10^{-5}	2.920×10^{-5}	2.206×10^{-5}	1.659×10^{-5}
Iteration 3	2.332×10^{-9}	1.341×10^{-9}	7.413×10^{-10}	4.036×10^{-10}	2.201×10^{-10}
Iteration 4	3.532×10^{-12}	2.686×10^{-12}	2.965×10^{-12}	2.434×10^{-12}	2.626×10^{-12}

The plot of normal stress component, σ_{xx}, and the deformed shape of the beam (x-axis and y-axis: mm) corresponding to the external load for p = 276 GPa, $\delta = 2.015\Delta x$ and 5 × 125 particles for the clamped slender beam using $G = 0$, 0.002, 0.004, 0.006, 0.007 and 0.008 are compared in Figure 5.12. The plots show that, without stabilisation, NOSB PD shows instabilities, evident, for instance, in the top plot, where colour corresponds to stress magnitude in kPa. The absence of the zero-energy mode control leads to significant oscillation in the stress field, which is most obvious near the support and the region experiencing larger displacements.

The stabilisation method proposed in [12] effectively suppresses the zero-energy modes, where $G = 0.006$, resulting in a stabilised stress field. However, continuing to increase the value of G results in a domination of the stabilisation force density over the PD force density, which subsequently results in the increase of stiffness.

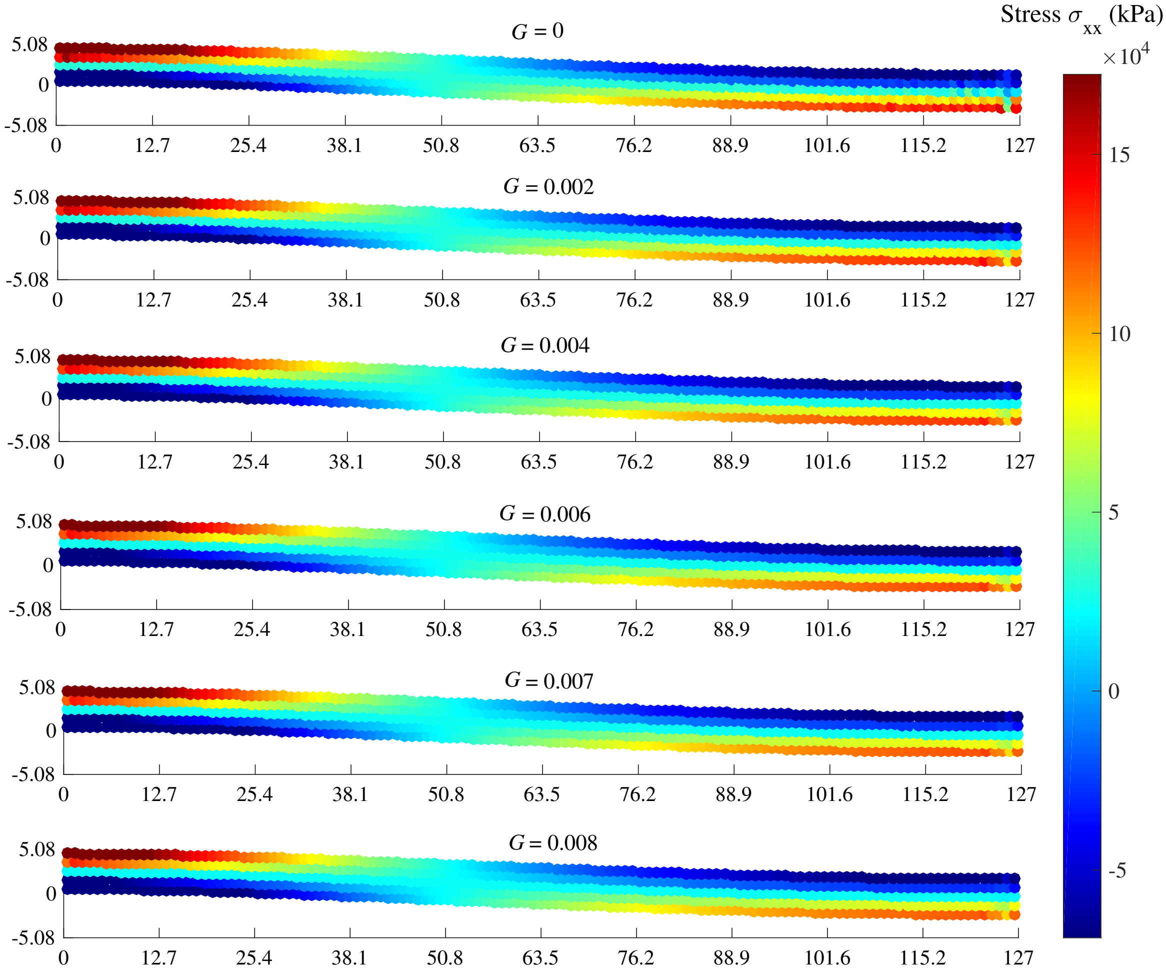

Figure 5.12: Clamped beam: stress contour, σ_{xx} for p = 276 kPa, $\delta = 2.015\Delta x$ with 5×125 particles with different G.

5.2.3 Simply-supported slender beam

A beam with the same material and geometric properties as the clamped slender beam in the example above but having simply-supported ends was next analysed. The same particle discretisations were used; however, the boundary conditions at the support were appropriately modified. As in the previous example, a fictitious boundary layer, of equivalent size to the horizon was introduced outside the actual material domain at the boundary region and displacement boundary conditions were imposed through this layer. To model the simply-supported edge, only one particle at the fictitious left-hand region of the middle surface was prevented from having in-plane displacement, allowing free rotation of the remainder of the end as shown in Figure 5.13. The problem was analysed using a loading increment of 27.6 kPa, applied in 10 load steps to a maximum loading of 276 kPa. Due to symmetry, only half of the beam was analysed and uniformly discretised into two different particle discretisation with three different horizon sizes.

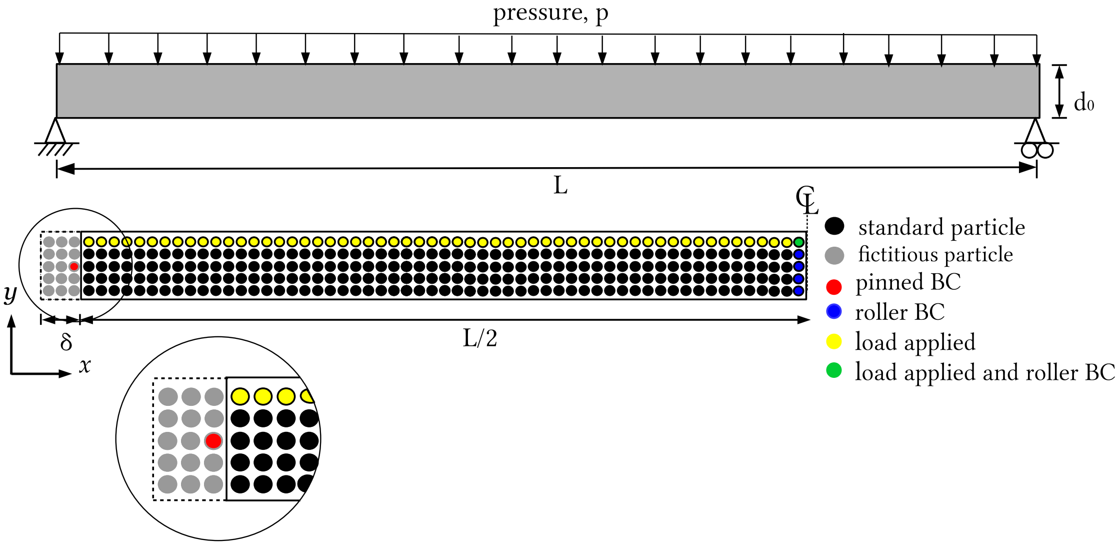

Figure 5.13: Simply-supported slender beam subjected to uniform transverse pressure.

The conclusions reached for the previous example are again supported by the results from this example in that the impact of zero-energy modes for larger horizon size results in larger displacements for a given particle spacing in the absence of additional stabilisation. The final normalised vertical displacement is compared in Figures 5.14 and 5.15 against the analytical result for two different particle discretisations, i.e. 3 × 75 particles and 5 × 125 particles, with different horizon sizes and different value of the stabilisation parameter, G. The agreement between analytical and numerical solutions reduces as the horizon size increases; however, the small horizon size of one particle spacing used in this problem tends itself to minimise the effect of the zero-energy modes. It is to be expected from previous examples, that a larger stabilisation parameter value would need to be added to the original PD force state for a problem with a larger horizon size in order to be effective at suppressing zero-energy modes. Since the PD formulations are nonlocal, this finding, while preliminary, predicts that the maximum accuracy will be achieved only for the horizon size approaches zero. The optimum value of G for larger horizon sizes is shown to be larger in order to provide enough stiffness for stability. However, continuing to increase the value of G once again results in an increase of non-realistic stiffness, thus reduced displacements as seen in both Figure 5.14 and 5.15.

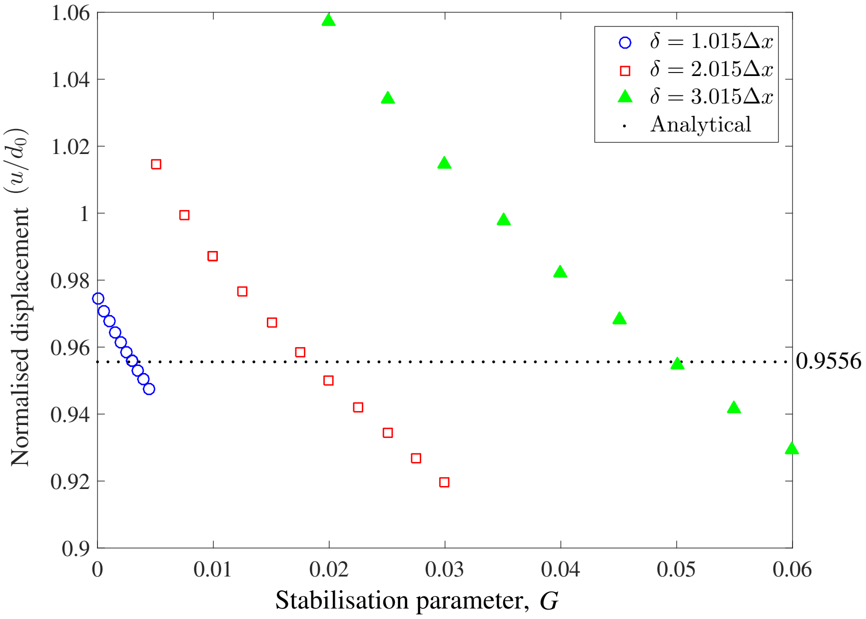

Figure 5.14: Simply-supported beam: normalised vertical displacement with changing G values and horizon sizes with 3 × 75 particles.

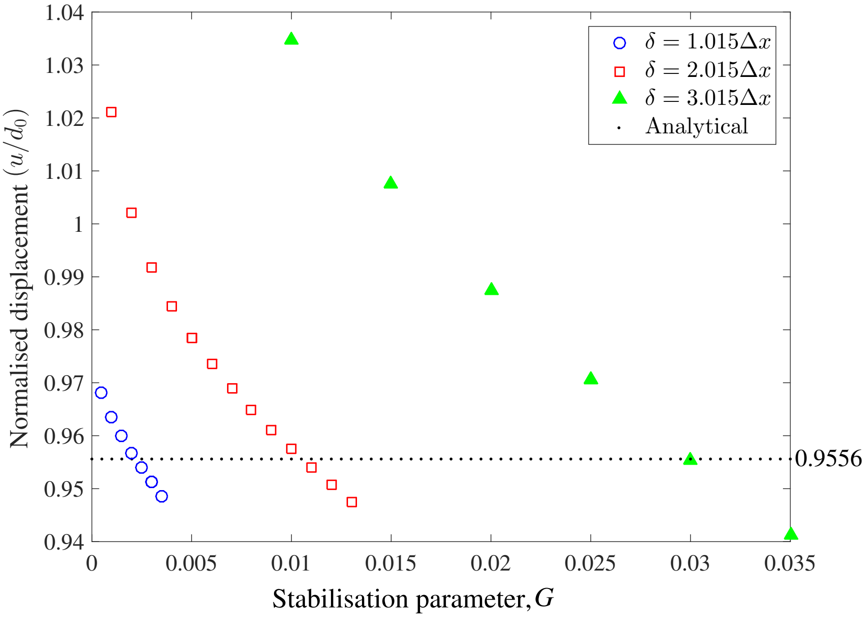

Figure 5.15: Simply-supported beam: normalised vertical displacement with changing G values and horizon sizes with 5 × 125 particles.

In Figure 5.16, the pressure versus normalised displacement response is compared against the analytical solution. The response is shown with three different horizon sizes, with stabilisation parameters of $G = 0.003$ with $\delta = 1.015\Delta x$, $G = 0.018$ with $\delta = 2.015\Delta x$ and $G = 0.0495$ with $\delta = 3.015\Delta x$. The analytical solution given by Molstad [155] is also shown. It can be clearly seen that the normalised vertical displacements agree well with the analytical result for all the horizon sizes.

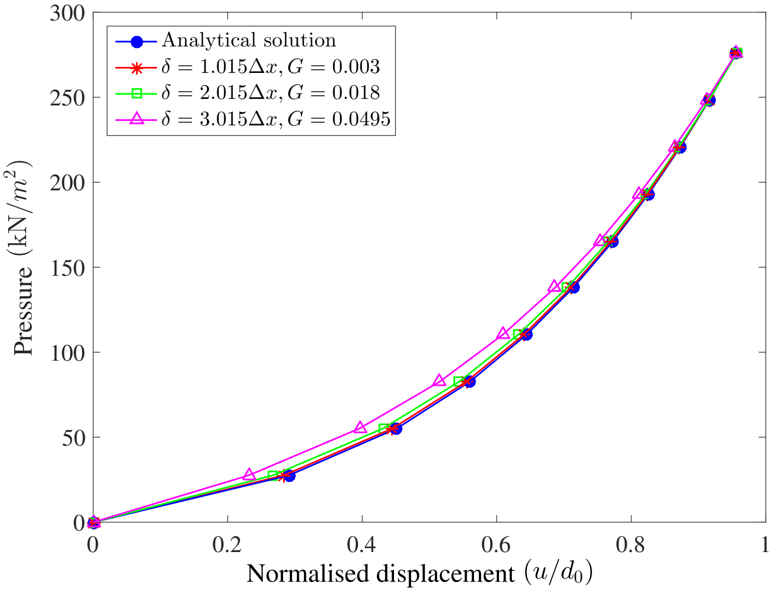

Figure 5.16: Simply-supported beam: normalised vertical end with 5 × 125 particles.

Table 5.3 gives the global Newton-Raphson (NR) residual for loadsteps 6 to 10 in this problem, with $G = 0.02$ and $\delta = 2.015$. The global tolerance was 1×10^{-10} and the data presented in the table shows quadratic (or near quadratic) convergence of the global out of balance force, demonstrating a correct implementation of the algorithmic consistent tangent for large deformation elasticity.

Table 5.3: Simply-supported beam: Newton-Raphson residuals showing near-quadratic convergence ($tol = 1 \times 10^{-10}$) with $\delta = 2.015\Delta x$ and $G = 0.02$.

Step	6	7	8	9	10
Iteration 1	6.120×10^{-2}	4.421×10^{-2}	3.070×10^{-2}	2.342×10^{-2}	1.842×10^{-2}
Iteration 2	2.610×10^{-4}	1.285×10^{-4}	7.000×10^{-5}	4.113×10^{-5}	2.568×10^{-5}
Iteration 3	5.343×10^{-8}	1.279×10^{-8}	3.780×10^{-9}	1.309×10^{-9}	5.126×10^{-10}
Iteration 4	7.758×10^{-12}	6.316×10^{-12}	5.661×10^{-12}	5.383×10^{-12}	5.357×10^{-12}

The plot of the normal stress component, σ_{xx}, and the deformed shape of the beam (x-axis and y-axis: mm) corresponding to the total external load of p = 276 kPa, with $\delta = 1.015\Delta x$ and a 5 × 125 particle distribution for the simply-supported slender beam problem are shown in Figure 5.17. Once again, it is clear that NOSB PD solutions exhibit instabilities, indicating the necessity of zero-energy modes control. The absence of the zero-energy mode control results leads to significant oscillations in the stress field. Increasing the value of G from 0 to 0.01 significantly reduces the stress oscillation leading to a more realistic stress profile. However, the zero-energy modes are still evident closer to supported end if $G < 0.01$. However, continuing to increase G results in the stabilisation force density dominating the original PD force density, which then results in an increase in stiffness which causes a reduction in the predicted displacement.

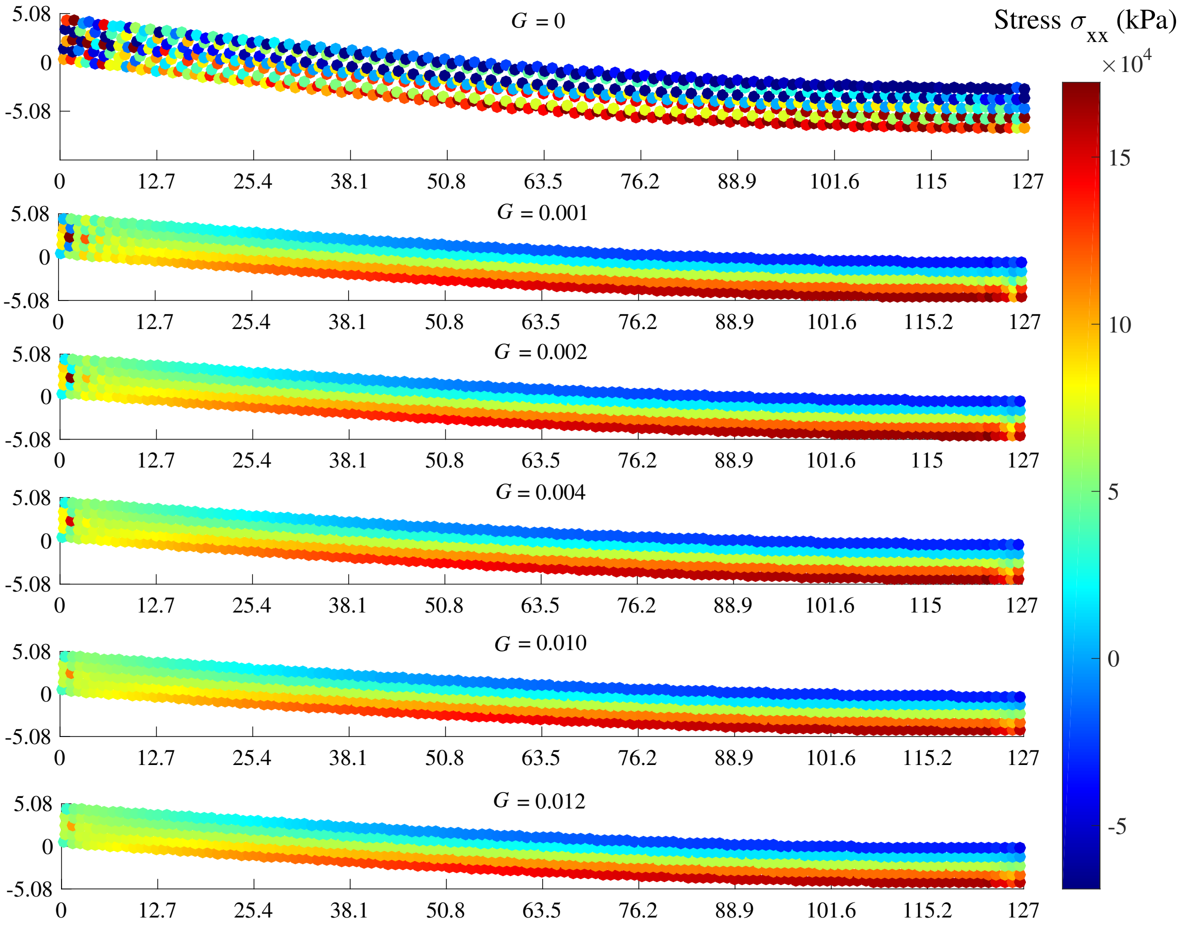

Figure 5.17: Simply-supported beam: stress contour, σ_{xx}, for p = 276 kPa, $\delta = 2.015\Delta x$, 5 × 125 particles with different G.

5.2.4 Cantilever beam

The final example tested was of a deep elastic cantilever beam, fixed at one end and subjected to a vertical mid-height particle load on its free end. The beam has a length, L of 10 m, depth, d_0 of 1 m, and is uniformly discretised with 5 × 50 particles.

Three values of horizon radius, $\delta = 1.015\Delta x$, $\delta = 2.015\Delta x$ and $\delta = 3.015\Delta x$ were used in this problem. The material properties were Young's modulus, $E = 12$ MPa and Poisson's ratio, $\nu = 0.2$. The beam was pinned at the fictitious boundary region at the mid-axis in both directions and roller boundary conditions applied to other particles along the fictitious left-hand region, allowing the structure to move only in the y-direction as shown in Figure 5.18. Compared to Section 4.4.2, a fictitious boundary layer in this example was introduced outside the actual material domain where displacement boundary conditions (BC) were imposed through the fictitious boundary layer. A vertical load of 100 kN was applied in 10 load steps with a tolerance of $1{\times}10^{-10}$ used on the global normalised out of balance force. The loads were applied through a layer of an actual particle on the right-hand region at the mid-axis, as shown in Figure 5.18 instead through an actual particle as shown in Section 4.4.2.

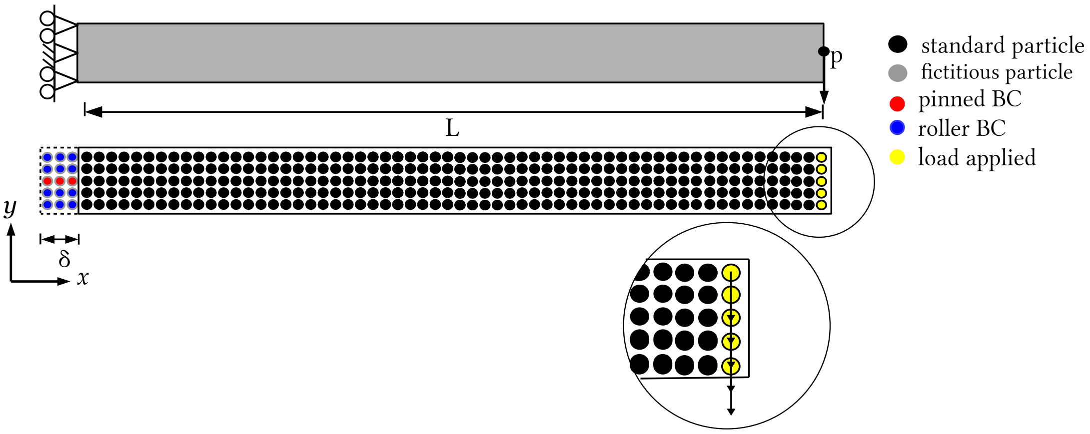

Figure 5.18: Cantilever beam subjected to vertical mid-side load.

Figure 5.19 compares the normalised displacement, at the end of the beam for different values of δ and G with the analytical solution [155] corresponding to the external load of 10 kN. As shown in the figure, for the unstabilised material, a significant difference in terms of normalised displacement ($u/L = 0.302$ with $\delta = 1.015\Delta x$, $u/L = 0.342$ with $\delta = 2.015\Delta x$ and $u/L = 0.529$ with $\delta = 3.015\Delta x$) is evident between those three horizon sizes. From Figure 5.19, we can also see that increasing G from an initial value of 0 visibly affects the normalised displacements.

In Figure 5.20, the load-deflection results predicted by the NOSB PD are compared against the analytical solution for the same problem [155] with three different horizon sizes and optimum stabilisation parameters, i.e. $G = 0$ with $\delta = 1.015\Delta x$, $G = 0.05$ with $\delta = 2.015\Delta x$ and $G = 0.315$ with $\delta = 3.015\Delta x$. Figure 5.20 shows there to be good agreement with the corresponding analytical solution with the optimum stabilisation parameter. It can be clearly seen that errors are small with smallest horizon values, $\delta = 1.015\Delta x$ to be efficient (no zero-energy issues) without the addition of the stabilised term to NOSB PD. This agrees with the results published in [120] where the zero-energy mode is not significant when adopting local horizon. Thus, a very small value of G is needed to eliminate any zero-energy mode for problems with horizon $\delta = 1.015\Delta x$.

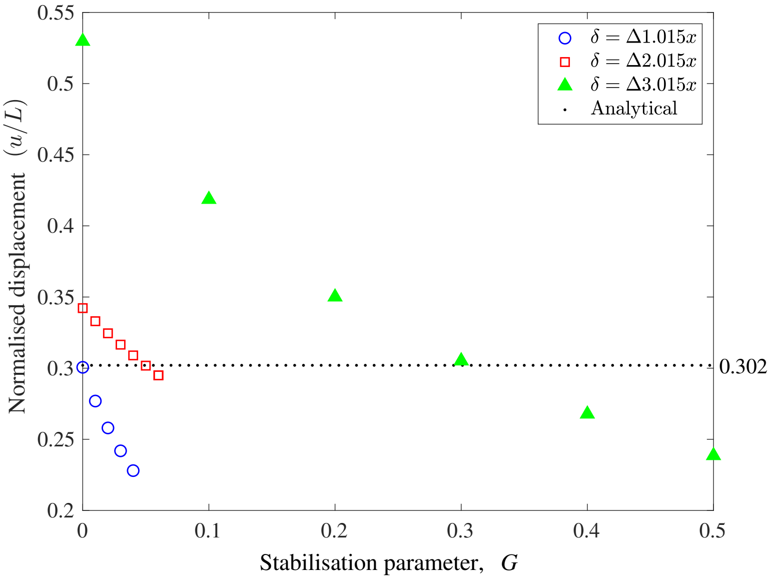

Figure 5.19: Cantilever beam: normalised vertical displacement with changing G and horizon sizes with with 5×50 particles.

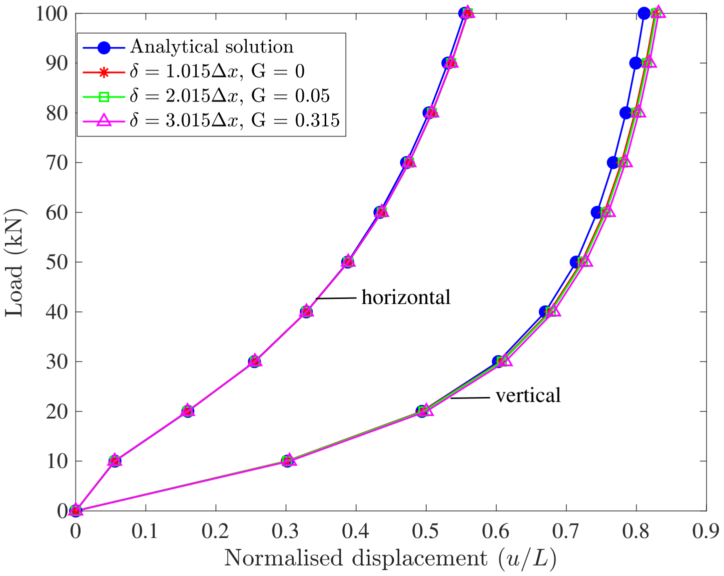

Figure 5.20: Cantilever beam: normalised vertical and horizontal displacement at the midpoint of the free end with 5 × 50 particles.

Stress distribution plots of the three stress components and the deformed shape for the fully loaded cantilever of $\delta = 2.015\Delta x$ when $G = 0.05$ are shown in Figure 5.21. These are plotted on the final deformed configuration showing the very large deformations modelled. The stabilisation method proposed in [12] effectively suppresses the zero-energy modes with the increase value of G, resulting in a stabilised stress field. However, for this problem, the method fails to converge with horizon sizes of $\delta = 2.015\Delta x$ when $G < 0.05$ .Therefore, a higher value of G is needed to eliminate the zero-energy modes. Figure 5.4 shows the convergence for the final 5 load steps of the Newton-Raphson process in this case. It can be seen that the Newton-Raphson algorithm needs more iterations to find the correct path, which then reaches asymptotic quadratic convergence compared to the other examples shown in Sections 5.2.2 and 5.2.3.

Table 5.4: Cantilever beam: Newton-Raphson residuals showing near-quadratic convergence ($tol = 1 \times 10^{-10}$) with $\delta = 2.015\Delta x$ and $G = 0.05$.

Step	6	7	8	9	10
Iteration 1	2.746×10^{-1}	1.513×10^{-1}	9.050×10^{-2}	5.792×10^{-2}	3.921×10^{-2}
Iteration 2	6.012×10^{-1}	6.251×10^{-4}	4.244×10^{-4}	2.790×10^{-4}	1.773×10^{-4}
Iteration 3	1.419×10^{-3}	3.054×10^{-4}	6.681×10^{-5}	1.526×10^{-5}	3.758×10^{-6}
Iteration 4	3.705×10^{-8}	1.838×10^{-9}	1.679×10^{-10}	1.863×10^{-11}	1.861×10^{-12}
Iteration 5	2.420×10^{-13}	7.773×10^{-14}	8.187×10^{-14}	–	–

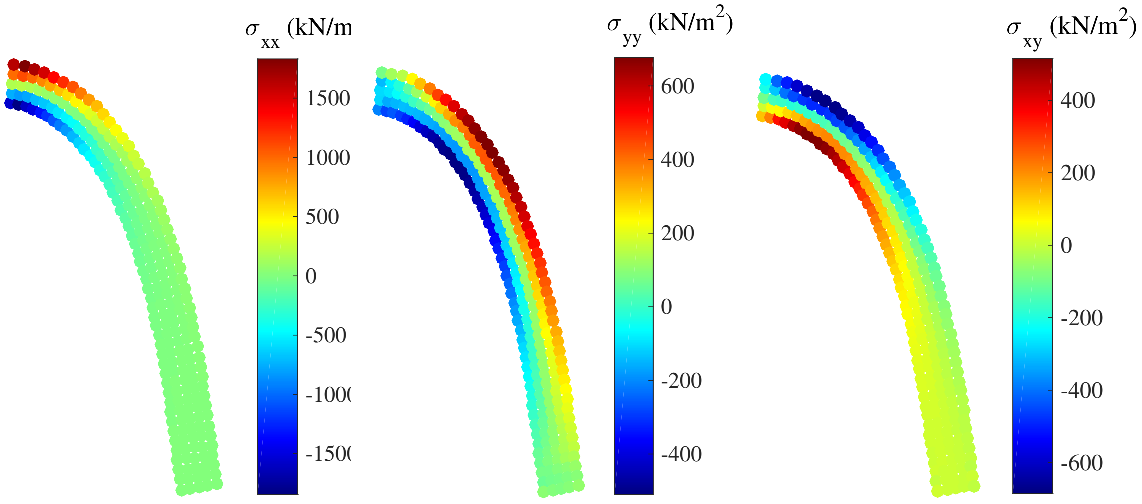

(a) (b) (c)

Figure 5.21: Cantilever beam: stress distribution for p = 100 kN (a) σ_{xx}, (b) σ_{yy} and (c) σ_{xy} with $\delta = 2.015\Delta x$ and $G = 0.05$.

5.3 Observations

In this chapter, a development of NOSB PD for large deformation with an implicit time integration scheme has been introduced. The Jacobian matrix based on the analytical expression of the equation of motion of NOSB PD was also explained. Within this, proper implementation of Jacobian was confirmed by the convergence rate of the global residual force in the various examples presented. The method was then demonstrated with numerical examples to validate the effectiveness of this approach, where analytical results exist. Results from these examples show horizon sizes, particle spacing, and the problem itself appear to be related to the optimum value of G. Overall, these results indicate that the NOSB PD simulation becomes mesh dependent in the absence of zero-energy mode control and for a given particle spacing, a smaller horizon size shows greater accuracy with no control on the zero-energy modes. The stabilised correspondence material model allows the proposed boundary condition to be used. Additionally, it is shown that the value of the optimum stabilisation parameter G used in this chapter is a positive constant less than 1, which has also been suggested by Silling in [12]. The next chapter will investigate an implicit NOSB PD problem with damage for which PD most applicable.

Chapter 6

Damage in the implicit NOSB PD model

6.1 Introduction

In the previous chapter, an implicit non-ordinary state-based peridynamics (NOSB PD) method has been implemented for large deformations based on an analytically constructed tangent stiffness for 2D problems. The Jacobian matrices of the NOSB PD with a correspondence continuum model for both the unstabilised and stabilised versions have been developed and the accuracy has been assessed with the inclusion of stabilisation parameters suggested by Silling [12]. Since the original peridynamics (PD) formulation was focused on dynamic problems, the earliest research focused mainly on the explicit formulation for dynamic simulations [9, 65, 74]. PD was adapted to the quasi-static case mainly using a dynamic relaxation method by introducing artificial damping in the time integration. Some existing work with implicit PD has been done, for example, [129] which was focused on crystal plasticity problems. However, the work did not extend to the prediction of damage. Another implicit implementation of NOSB PD, presented in [77], was limited to the development and numerical implementation of a small strain linearly elastic model. Zaccariotto and *et al.* [159] proposed a progressive damage formulation to be taken into account for a microelastic brittle material, and implemented the formulation within a bond-based peridynamics (BB PD) framework.

The most frequently used damage model in PD is the Prototype Microelastic Brittle (PMB) material proposed by Silling and Askari [53] for which, when a bond fails, its strength and stiffness suddenly drop to zero. In this chapter, the implementation of the NOSB PD approach detailed in the previous chapter is extended to include static crack propagation phenomena solved with a Newton-Raphson method. However, the discontinuity of the damage law prevents a standard implementation of a Newton-Raphson (NR) type of algorithm as explained in [160]. The best solution is identify regions of the response of the structure in which the stiffness matrix is constant and then change it as soon as one or more bonds fail, as stated in [160]. However, in complex models, with a large number of bonds, such an approach would be impractical.

This chapter provides the numerical implementation, and the theory behind the implementation in Section 6.2, which introduces a modification to the force term including a softening term and develops modified Jacobian matrices of the NOSB PD with a correspondence continuum model [12]. Numerical examples are demonstrated in Section 6.3, and the accuracy is assessed with the inclusion of different stabilisation parameters, and finally, a chapter review is drawn in Section 6.4. This chapter introduces for the first time non-ordinary state-based peridynamics (NOSB PD) with non-linear implicit static solution procedures to study crack propagation problems and proves the viability of using implicit approaches for the static solution of crack propagation problems.

6.2 Damage

Material damage in PD is introduced through the elimination of interaction (bonds) among particles. Recall from Chapter 2, once a bond fails, there is no force sustained in the bond and fracture is introduced through the failure of bonds. The mostly used damage criteria available in the literature are based on the critical bond stretch as explained in Section 2.4.1. This critical bond stretch damage criteria had been widely used in BB PD and had been applied in ordinary state-based peridynamics (OSB PD) and NOSB PD [81, 116, 148]. The criteria is based on the initial position and the deformation. In terms of the critical bond stretch, it is assumed that when the stretch, s, between two particles exceeds its critical stretch value, s_{cr}, damage occurs.

A new damage model in implicit NOSB PD is proposed here based on the critical bond stretch criterion. This damage model assumes that a crack begins to initiate when the bond stretch exceeds the critical bond stretch, and the influence of this bond on other bonds within the corresponding horizon is then removed. Therefore, the force density vector of other bonds within the horizon will not be considered anymore. However, to ensure optimum convergence of the global equilibrium equations, instead of vanishing the influence of the bond immediately, the best way is to establish a degradation in the interaction of the bond as the bond stretch increases.

6.2.1 Damage model

In the classical PD material damage explained in Section 2.4, the bond force drops abruptly to zero when the bond reaches its failure limit. This Prototype Microelastic Brittle (PMB) material proposed by Silling and Askari [53] and has been widely used for modeling fracture problems in elastic brittle materials with explicit time-integration scheme. However, the discontinuity of the constitutive law prevents a standard implementation of a Newton-Raphson type of algorithm as stated in [36]. In this work, damage will be included for the first time within a NOSB PD approach with an implicit solution scheme based on the Newton-Raphson (NR) solution procedure. Recently, there have been initial attempts to include material damage and failure for PD with implicit solution procedures. Two implicit static solution procedures have been introduced by Tao Ni et al. [161] and this has been implemented in BB PD. In this study, it is assumed that a term is proposed to be added to the force vector-state given by T_{s}, the bond stiffness where

$$T_s = \begin{cases} 1 & \text{if } s < s_{min}, \\ \frac{1}{2}\left(1 - \tanh\left(\frac{\beta(s_{min}+s_{cr}-2s)}{s_{min}-s_{cr}}\right)\right) & \text{if } s_{min} \leqslant s < s_{cr}, \\ 0 & \text{otherwise.} \end{cases} \tag{6.1}$$

s_{min} is a value between 0 to s_{cr} and β is a positive constant value to control the rate of degradation in the bond interaction, as shown in Figure 6.1. In this study, $\beta = 3$ is used and hence, the following new stabilised force vector-state is formulated as follows:

$$\underline{\mathbf{T}}\langle\boldsymbol{\xi}\rangle = \omega(|\boldsymbol{\xi}|)[\sigma^0(\mathbf{F})]^T\,\mathbf{B}\,(\mathbf{x})\,\boldsymbol{\xi}\,T_s + \underline{\mathbf{T}}_z\omega(|\boldsymbol{\xi}|)\,T_s. \tag{6.2}$$

In order to control stability in the simulation, no bonds can completely fail during the equilibrium NR iterations. The bonds are removed after equilibrium has been found and the contribution of the broken bonds to the global stiffness matrix has to be removed. This is to stop oscillations occurring within the NR procedure due to the load redistribution as bonds are removed from the analysis, i.e. a smooth variation from intact to failed is obtained via equal Eq. (6.1). With the additional softening term added to the internal force, the Jacobian can be expressed as

$$\begin{aligned}\mathbf{K} = \sum_{i}^{I_n}\sum_{j=1}^{m}\sum_{k}^{ndof} & \left(\omega_i(|\boldsymbol{\xi}|)\frac{\partial\underline{\mathbf{T}}[\mathbf{x}_i]}{\partial\mathbf{u}_k}T_s[\mathbf{x}_i] + \omega_i(|\boldsymbol{\xi}|)\frac{\partial T_s[\mathbf{x}_i]}{\partial\mathbf{u}_k}\underline{\mathbf{T}}[\mathbf{x}_i]\right) \\ & - \left(\omega_j(|\boldsymbol{\xi}|)\frac{\partial\underline{\mathbf{T}}[\mathbf{x}_j]}{\partial\mathbf{u}_k}T_s[\mathbf{x}_j] + \omega_i(|\boldsymbol{\xi}|)\frac{\partial T_s[\mathbf{x}_j]}{\partial\mathbf{u}_k}\underline{\mathbf{T}}[\mathbf{x}_j]\right),\end{aligned} \tag{6.3}$$

and with the stabilisation term, the analytical expression of the new Jacobian is as follows

$$\begin{aligned}\mathbf{K} = \sum_{i}^{I_n}\sum_{j=1}^{m}\sum_{k}^{ndof} & \Bigg(\left(\omega_i(|\boldsymbol{\xi}|)\frac{\partial\underline{\mathbf{T}}[\mathbf{x}_i]}{\partial\mathbf{u}_k}T_s[\mathbf{x}_i] + \omega_i(|\boldsymbol{\xi}|)\frac{\partial T_s[\mathbf{x}_i]}{\partial\mathbf{u}_k}\underline{\mathbf{T}}[\mathbf{x}_i]\right) \\ & + \left(T_s[\mathbf{x}_i]\frac{GC}{\omega_0}\left(\frac{\partial\underline{\mathbf{Y}}\langle\mathbf{x}_j-\mathbf{x}_i\rangle}{\partial\mathbf{u}_k} - \frac{\partial\mathbf{F}(\mathbf{x}_i)}{\partial\mathbf{u}_k}(\mathbf{x}_j-\mathbf{x}_i)\right) + \underline{\mathbf{T}}_z[\mathbf{x}_i]\omega(|\boldsymbol{\xi}|)\frac{\partial T_s[\mathbf{x}_i]}{\partial\mathbf{u}_k}\right)\Bigg) \\ & - \Bigg(\left(\omega_j(|\boldsymbol{\xi}|)\frac{\partial\underline{\mathbf{T}}[\mathbf{x}_j]}{\partial\mathbf{u}_k}T_s[\mathbf{x}_j] + \omega_i(|\boldsymbol{\xi}|)\frac{\partial T_s[\mathbf{x}_j]}{\partial\mathbf{u}_k}\underline{\mathbf{T}}[\mathbf{x}_j]\right) \\ & + \left(T_s[\mathbf{x}_j]\frac{GC}{\omega_0}\left(\frac{\partial\underline{\mathbf{Y}}\langle\mathbf{x}_i-\mathbf{x}_j\rangle}{\partial\mathbf{u}_k} - \frac{\partial\mathbf{F}(\mathbf{x}_j)}{\partial\mathbf{u}_k}(\mathbf{x}_i-\mathbf{x}_j)\right) + \underline{\mathbf{T}}_z[\mathbf{x}_j]\omega(|\boldsymbol{\xi}|)\frac{\partial T_s[\mathbf{x}_j]}{\partial\mathbf{u}_k}\right)\Bigg).\end{aligned} \tag{6.4}$$

The derivative of the softening term with respect to the displacement can be expressed as

$$\frac{\partial T_s[\mathbf{x}_i]}{\partial \mathbf{u}_k} = \frac{\partial T_s}{\partial q}\frac{\partial q}{\partial n}\frac{\partial n}{\partial s}\frac{\partial s}{\partial \|\eta+\xi\|}\frac{\partial \|\eta+\xi\|}{\partial \mathbf{u}_k}, \tag{6.5}$$

where

$$T_s = \frac{1}{2}(q), \quad q = 1-\tanh(n) \quad \text{and} \quad n = \frac{\beta(s_{min}+s_{cr}-2s)}{s_{min}-s_{cr}}, \tag{6.6}$$

and

$$\frac{\partial T_s}{\partial q} = \frac{1}{2}, \quad \frac{\partial q}{\partial n} = \tanh^2(n-1), \quad \frac{\partial n}{\partial s} = \frac{-2\beta}{s_{min}-s_{cr}} \quad \text{and} \quad \frac{\partial s}{\partial \|\eta+\xi\|} = \frac{1}{\|\xi\|}. \tag{6.7}$$

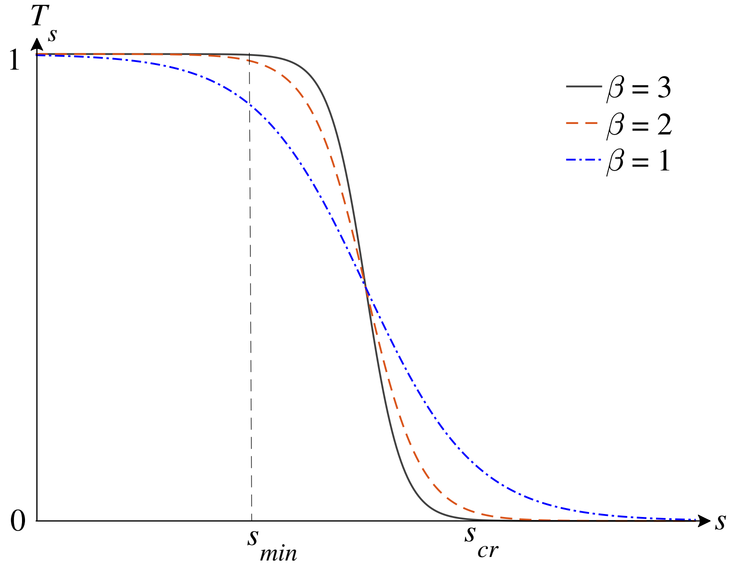

Figure 6.1: Scalar function to control the decrease of the bond force, T_{s}.

The details of this implicit NOSB PD algorithm are given in the flowchart as shown in Figure 6.2. As shown, the following procedure is followed:

1. PD simulation starts from initialisation (parameter, mesh generation, interactions search, and boundary conditions).
2. Identify s_{min} and s value.

3. Determine T_s and calculate the new force vector-state based, $\underline{\mathbf{T}}\langle\boldsymbol{\xi}\rangle$.
4. The equilibrium equation is solved with iterative update of the modified Jacobian as in Eq. (6.4).
5. Bonds are allowed to fail after the convergence criterion is attained before applying the next load increment.

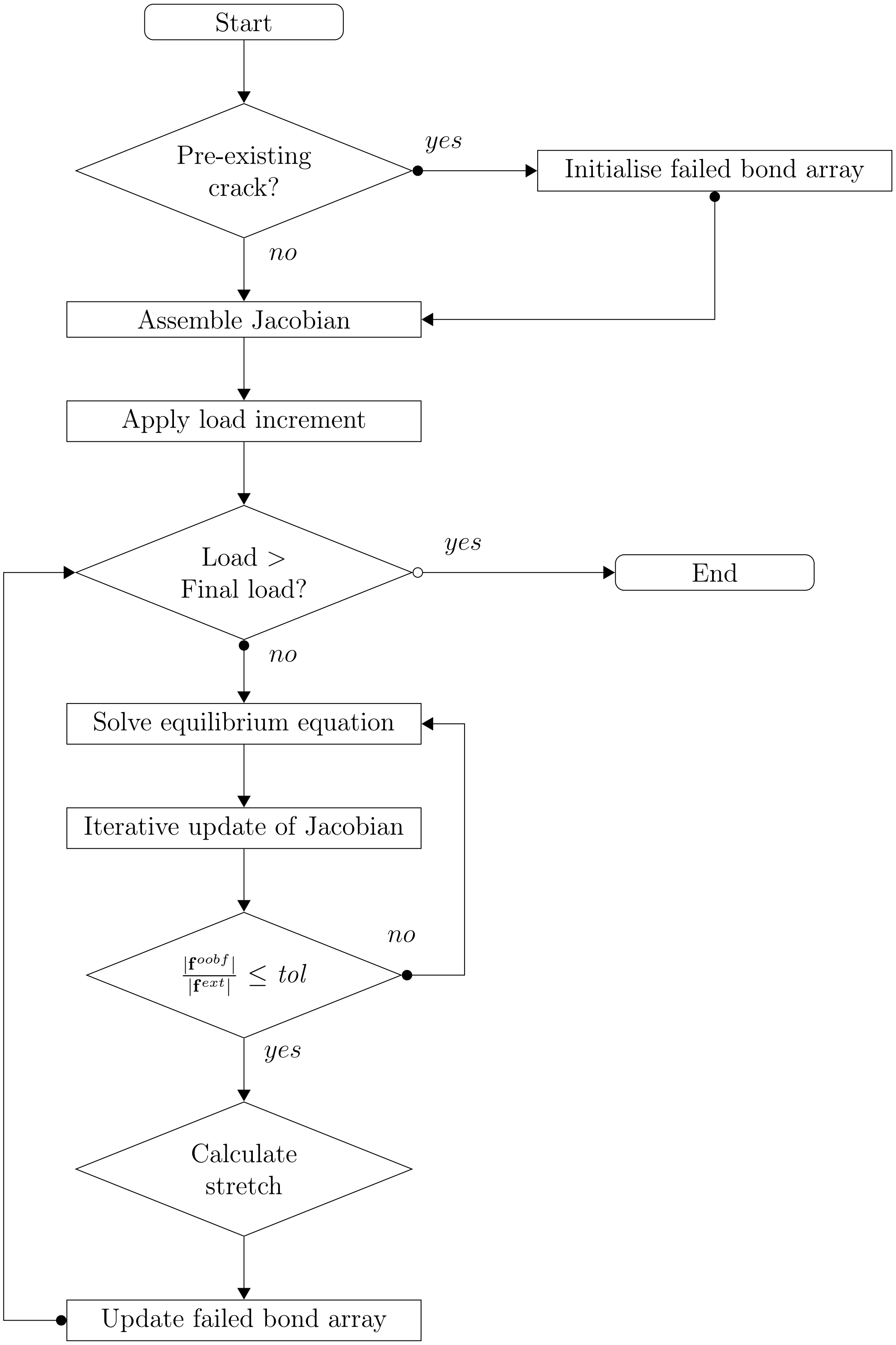

Figure 6.2: Flowchart of the NOSB PD implicit algorithm with material failure.

6.3 Numerical examples

6.3.1 Plate with a hole

A rectangular plate with a circular hole in the centre is first considered. The left and right ends of the plate were subjected to a horizontal displacement in opposite directions (so that the plate is under tension) of 1 × 10^4 mm in 15 load steps as illustrated in Figure 6.3. Layers of fictitious boundary particles were introduced outside the actual material domain at the boundary region where the size of the layer was equivalent to the horizon size and the Dirichlet boundary conditions (BC) were imposed through the fictitious boundary layer. The plate initially had a length, L of 150 mm and a width, W of 50 mm with radius of hole, r of 10 mm as shown in Figure 6.3. The plate was made from material with a Young's modulus of $E = 210$ GPa and Poisson's ratio of $\nu = 0.33$. The analysis assumes plane strain conditions. To further quantify the effectiveness of the proposed implicit framework , different values of the stabilisation parameter were used with the horizon radius, $\delta = 3.015\Delta x$ and particle discretisations of 30 × 10 particles were used.

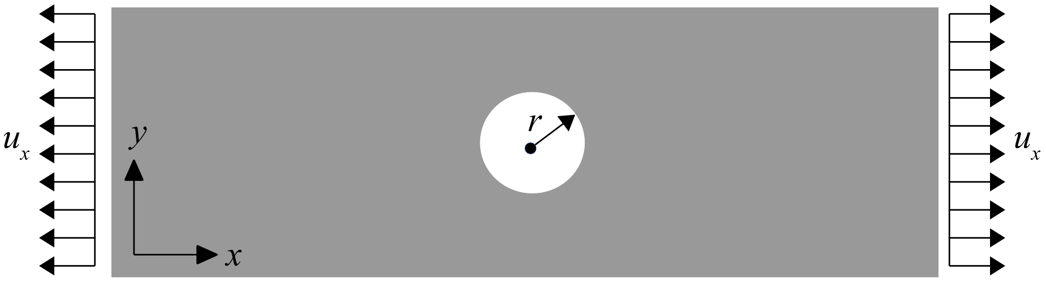

Figure 6.3: Plate with circular hole: geometry.

A surface plot of displacements in the x-direction when failure is not allowed with 30 × 10 particles and without stabilisation is shown in Figure 6.4, resulting in a unstabilised displacement field. This prediction exhibits zero-energy mode deformation and oscillations in the form of displacement during quasi-static simulations. The same problem was analysed with $G = 0.01$ and results are shown in Figure 6.5, where horizontal displacement predictions are now free of any oscillations.

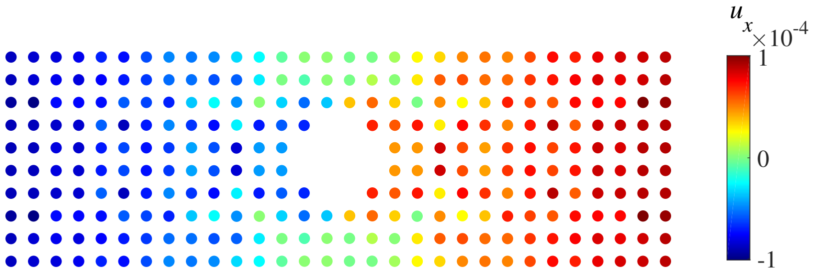

Figure 6.4: Plate with circular hole: horizontal displacement plots (NOSB PD) when failure is not allowed with 30 × 10 particles and $G = 0$.

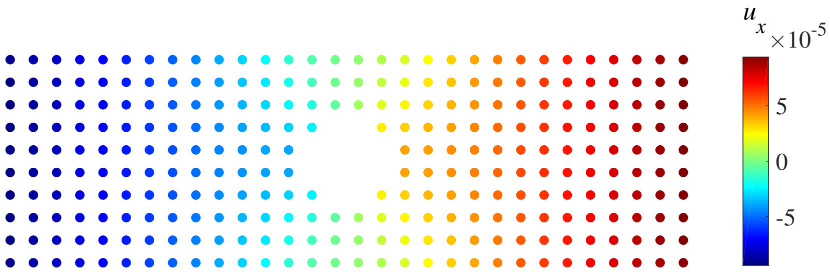

Figure 6.5: Plate with a circular hole: horizontal displacement plots (NOSB PD) when failure is not allowed with 30 × 10 particles with $G = 0.01$.

Damage is now incorporated and the critical stretch failure criterion is adopted, with $s_{cr} = 0.002$ and $s_{min} = 0.0015$. As illustrated in Figure 6.6, damage is plotted with $G = 0.01$ at the end of the analysis. It can be seen that the modelling predicts a wide damage area in terms of crack shape.

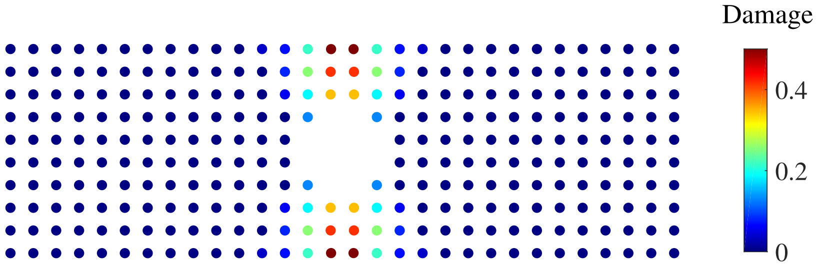

Figure 6.6: Plate with a circular hole: damage with 30 × 10 particles and $G = 0.01$ at the end of the analysis.

A finer grid spacing is now used for the same problem, with 150 × 50 particles. Although most of the PD literature validate their proposed models by comparing the shape of fracture patterns to assess the accuracy of PD based simulations, in this example, FEM analysis was used to verify the accuracy of the results obtained by the proposed NOSB PD model. The variation of horizontal displacement along the central axes when damage was not allowed is shown in Figure 6.7. The determination of the stabilisation parameter, G needs to be done before the damage is considered. From Figure 6.7, it can be seen that increasing G from an initial value of 0 visibly affects the displacements in the x-direction. The stabilisation method is demonstrated to be effective on suppressing zero-energy modes as G is increased up to $G = 0.001$. However, continuing to increase the value of G results in a domination of the stabilisation force density over the PD force density which subsequently results in the increase of stiffness.

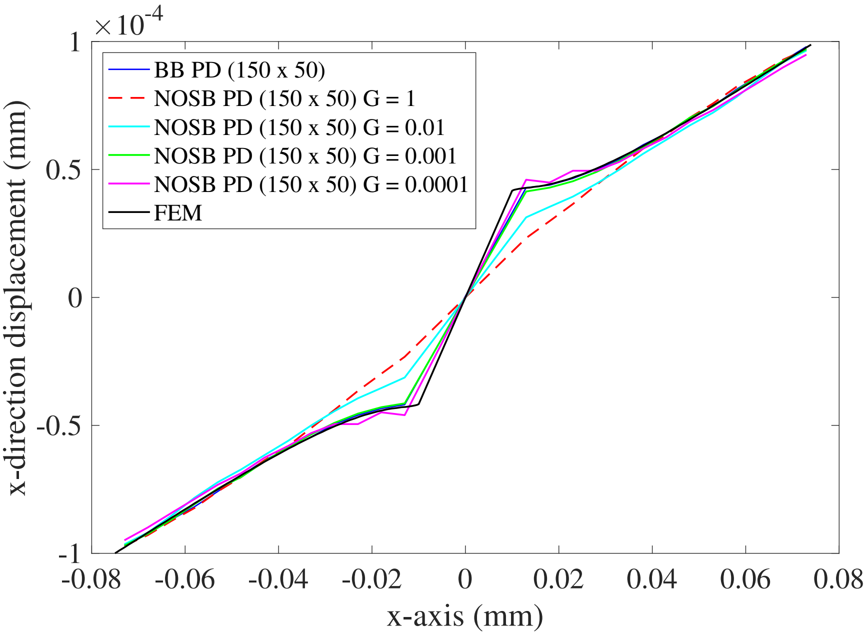

Figure 6.7: Plate with circular hole: variation of horizontal displacement along the central axes when failure is not allowed with 150 × 50 particles.

Figure 6.8 shows the displacement plots without damage with $G = 0.001$, and the damage plots when failure is allowed is shown in Figure 6.9. As expected, cracks are initiated from the hole boundary and propagates towards the edges of the plate and wiith decreasing particle spacing, the resolution of the crack is improved. The failure progress of holed plates subjected to a horizontal displacement can therefore be successfully predicted by the proposed implicit NOSB PD. Figures 6.10 and 6.11 show initial and final phases, respectively bonds that are still connected when failure is allowed. It is not surprising that once the bonds near the hole start breaking, they extend towards the free edges of the plate.

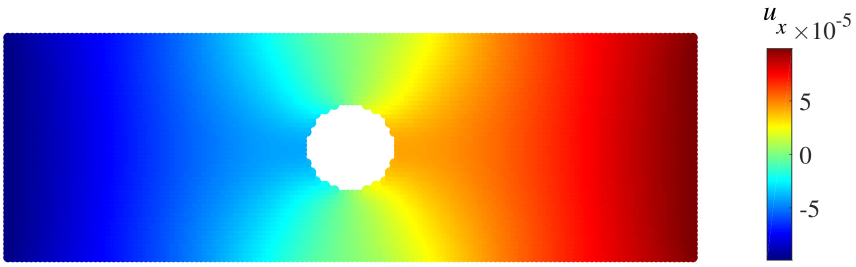

Figure 6.8: Plate with a circular hole: horizontal displacement plots (NOSB PD) when failure is allowed with 30 × 10 particles and $G = 0.01$.

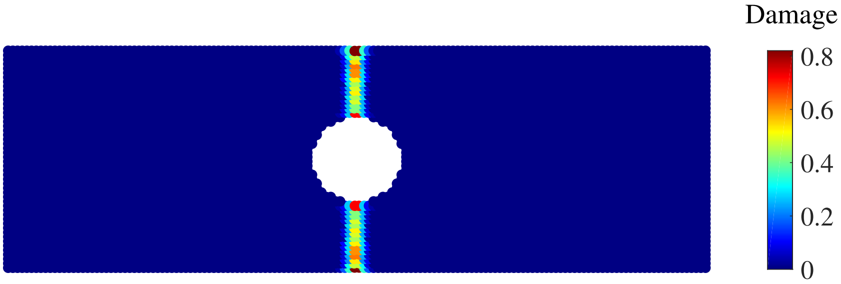

Figure 6.9: Plate with a circular hole: damage plots (NOSB PD) when failure is allowed with 150 × 50 particles and $G = 0.001$.

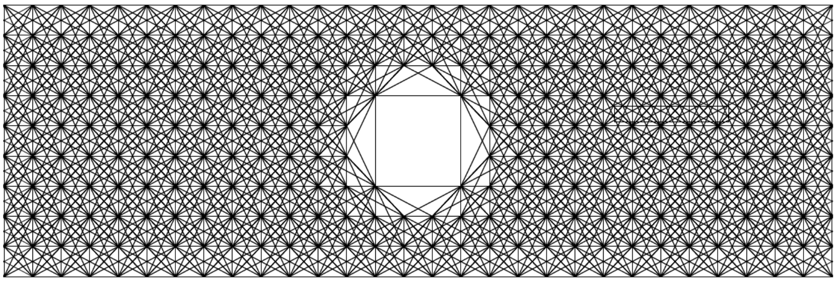

Figure 6.10: Plate with a circular hole: initial connected bonds.

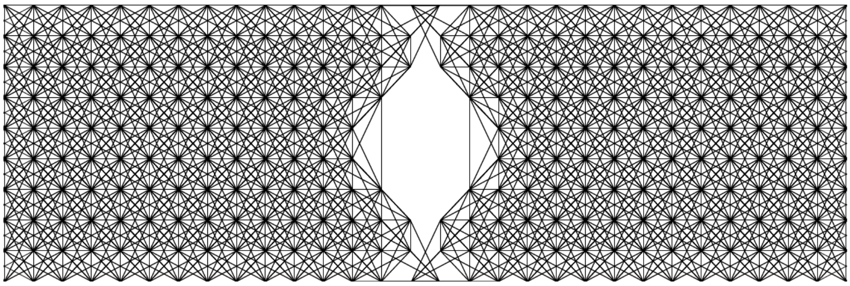

Figure 6.11: Plate with a circular hole: connected bonds due to crack propagation.

6.3.2 Plate with an initial crack

The second problem considered in this chapter is the behaviour of a square plate with an existing crack. The plate at the beginning of the analysis had a length, L of 50 mm with an existing crack of 10 mm, Young's modulus of $E = 192$ GPa and Poisson's ratio of $\nu = 0.33$ as shown in Figure 6.12. The top and bottom ends of the plate were subjected to the displacement of 1.6×10^{-5} in opposite directions in 15 load steps. In order to implement displacement boundary conditions (BCs), a fictitious boundary layer was introduced outside the actual material domain at the boundary region where the size of the layer was equivalent to the horizon size and displacement BCs were imposed through the fictitious boundary layer as illustrated in Figure 6.13. The analysis assumes plane strain conditions. The horizon radius was set to $\delta = 3.015\Delta x$ and particle discretisations of 50 $\times$50 particles were used. Damage was incorporated, and the critical stretch failure criterion was adopted, with a critical stretch $s_{cr} = 0.002$ and $s_{min} = 0.0015$.

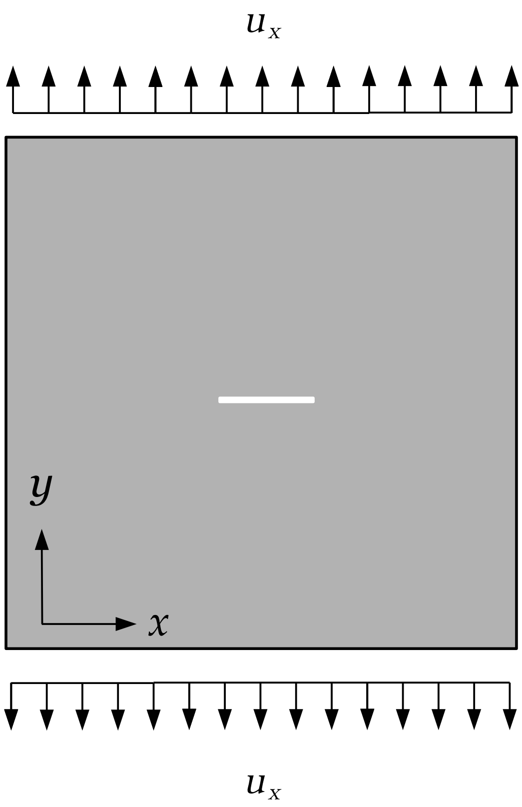

Figure 6.12: Plate with existing crack: geometry under slow stretch.

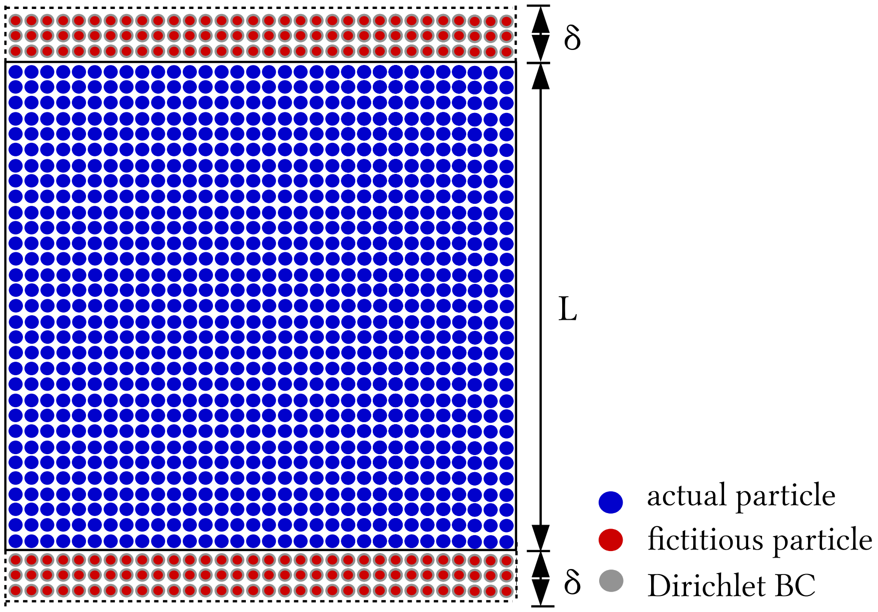

Figure 6.13: Plate with existing crack: geometry under slow stretch.

The value of the stabilisation parameter, G used in this example is $G = 0.001$, which is assumed to be the same as the previous examples since the particle spacings and horizon size are the same. In Figure 6.14, the initial damage plots are shown for the two different particle discretisations; 50 × 50 particles with horizon sizes, $\delta = 3.015\Delta\mathbf{x}$ and $G = 0.001$. Figure 6.15 show the final damage plots are shown for particle discretisations; 50 × 50 particles. As expected, the crack emanates from the existing crack at which high displacement gradients exist and propagates toward the edges of the plate, as shown in Figures 6.15.

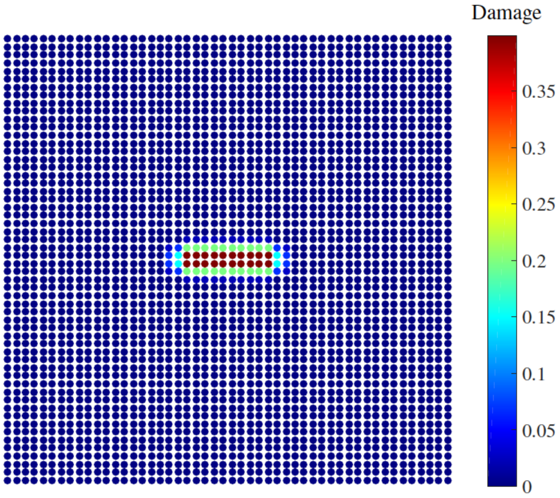

Figure 6.14: Plate with existing crack: initial damage plots (NOSB PD) with 50 × 50 particles.

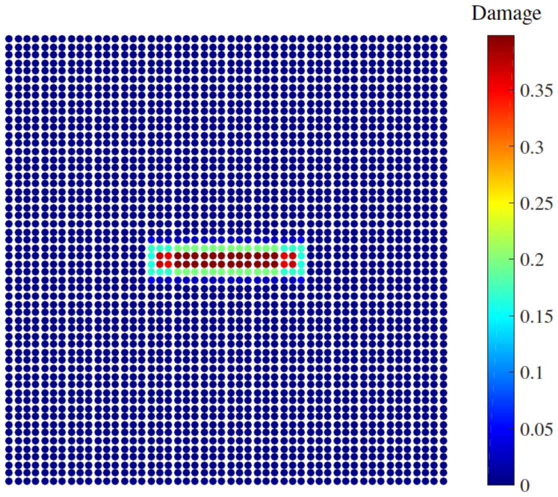

Figure 6.15: Plate with existing crack: final damage plots (NOSB PD) with 50 × 50 particles.

6.3.3 Cantilever beam with pre-existing crack

The final example shown in this chapter is of an elastic cantilever beam with a pre-existing crack, as shown in Figure 6.16. The length and width of the beam were L = 10 m and d_0 = 1 m. The depth of the notch is 0.15 m vertically starting from the upper surface of the beam. The notch is located at a distance of 9 m from the free end of the beam. The cantilever beam was uniformly discretised with 5 × 50 particles. The beam was fixed at one end and subjected to a vertical mid-height particle load on its free end. The horizon radius were selected as $\delta = 3.015\Delta x$ in this problem, The optimum stabilisation parameters, $G = 0.315$ was chosen, as being used in Section 5.2.4. The material parameters used were Young's modulus, $E = 12$ MPa and Poisson's ratio, $\nu = 0.2$. In order to implement displacement constrains, the fictitious boundary region were created with a width of $3.015\Delta x$. The beam was pinned at the fictitious boundary region at the mid-axis in both directions and roller boundary conditions applied to other particles along the fictitious left-hand region, allowing the structure to move only in the y-direction as shown in Figure 6.16. A vertical load of 6 kN was applied in 10 load steps with a tolerance of 1×10^{-10} used on the global normalised out of balance force. The loads are applied through a layer of an actual particle on the right-hand region at the mid-axis, as shown in Figure 6.16.

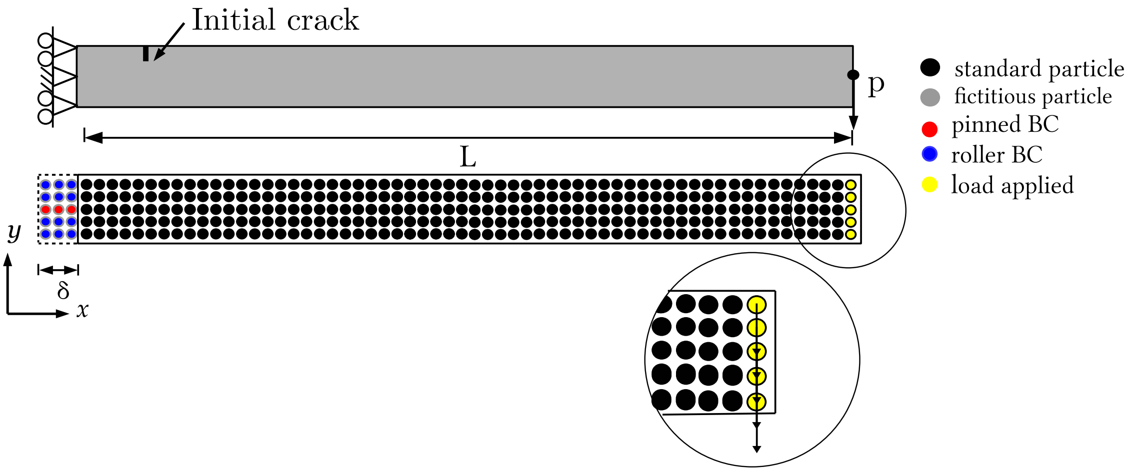

Figure 6.16: Cantilever beam with pre-existing crack: geometry subjected to vertical mid-side load.

Figure 6.17 shows the model of a cantilever beam with a pre-existing crack. The nodes shown in Figures 6.17 and 6.18 are PD nodes and the blue lines are the initial bonds connecting particles. Figure 6.18 is an enlarged view near the crack region.

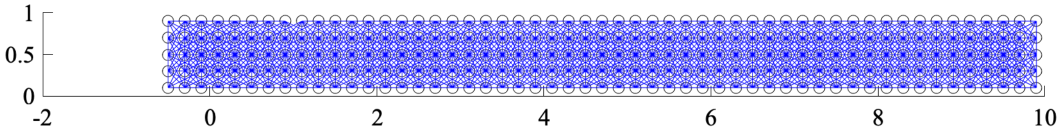

Figure 6.17: Cantilever beam with pre-existing crack: initial bond breakage.

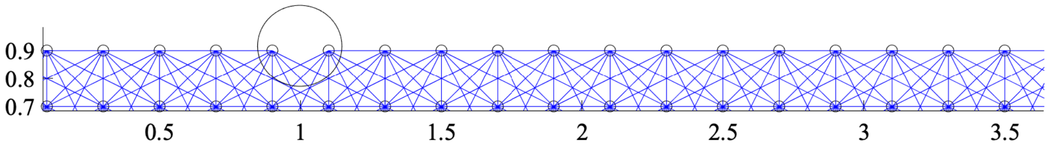

Figure 6.18: Cantilever beam with pre-existing crack: zoomed-in initial bond breakage.

The initial damage plot evaluated at each particle based on the broken bonds are shown in Figure 6.19 and the final damage plot are shown in Figure 6.21, where growth of the crack is close to straight in this case. Since the damage of each particle is defined by the broken bonds in the particle's horizon domain, with the increase of particle spacing, the damage zone becomes wider.

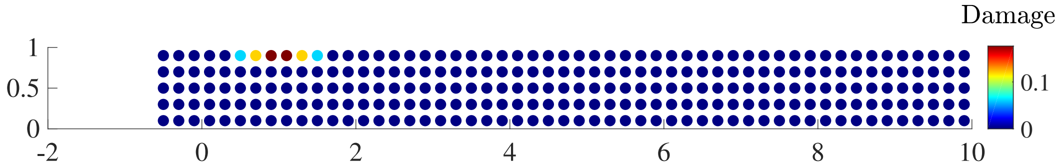

Figure 6.19: Cantilever beam with pre-existing crack: initial damage plots.

The final crack initiatiation is shown in Figure 6.20. The blue lines in this Figure 6.20 represent the broken bonds

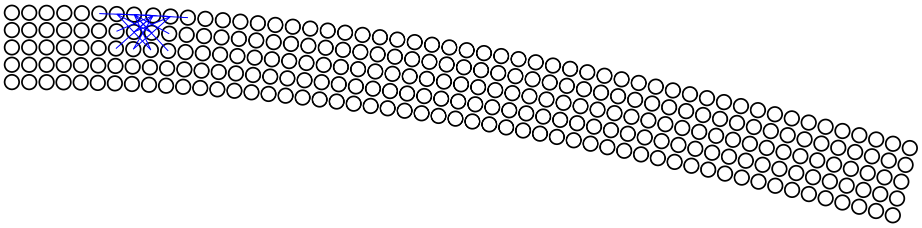

Figure 6.20: Cantilever beam with pre-existing crack: final broken bonds due to crack propagation

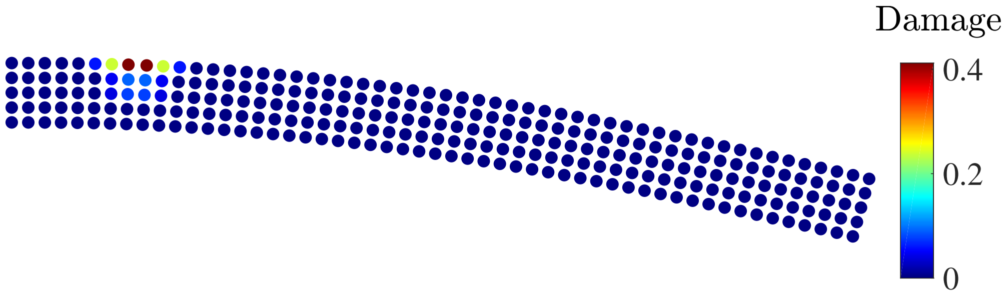

Figure 6.21: Cantilever beam with pre-existing crack: final damage plots (NOSB PD).

In Figure 6.22, the load-displacement results predicted by the NOSB PD are shown with horizon sizes and optimum stabilisation parameters, i.e. $G = 0.315$ with $\delta = 3.015\Delta x$ at the midpoint of the free end with 5 × 50 particles.

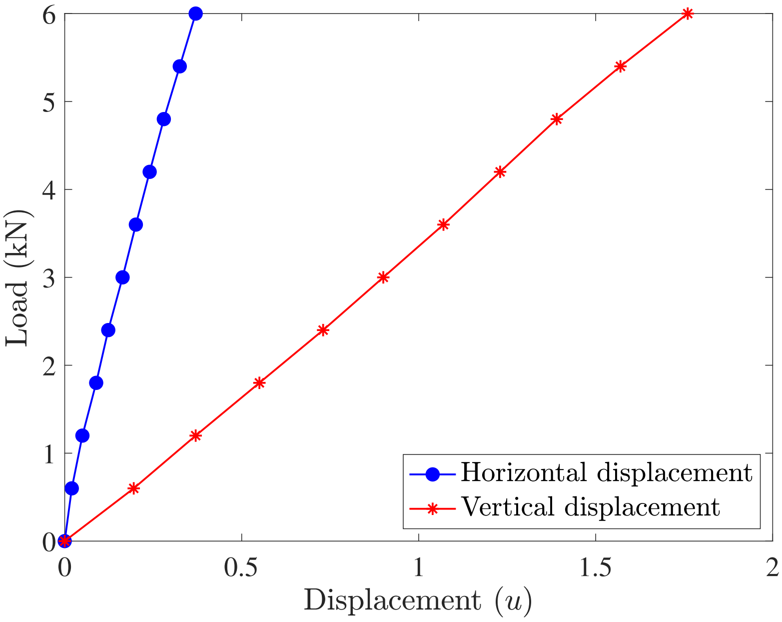

Figure 6.22: Cantilever beam with pre-existing crack: variation of vertical and horizontal displacement at the midpoint of the free end.

With the identical load increment of 0.6 kN, the cantilever beam with pre-existing crack can hold the external vertical load of 4.2 kN without any damage or broken bond. While another two load increments are subsequently applied to the structure one by one, the beam can still reach an updated equilibrium state each time, though damage occurs along the notch end. The cantilever beam with pre-existing crack would surely be able to hold lower external load than the perfect cantiliver beam. Moreover, in a cantilever beam model with pre-existing crack, the section close to the fixed end will share higher stress when subjected to the vertical load on its free end will weaken the loading capacity of the structure to a much greater extent.

6.4 Observations

In this chapter, the development of NOSB PD for large deformation with an implicit time integration scheme with the prediction of damage has been introduced. A new damage model in implicit NOSB PD is proposed based on the critical bond stretch, therefore instead of vanishing the influence of bond immediately, a degradation in the interaction of bond has been established as the bond stretch increases.The development of the Jacobian matrix based on the analytical expression of the equation of motion of NOSB PD with the damage model and inclusion of degradation in the bond interction were also explained. The method was then demonstrated with an examples to validate the effectiveness of this approach (different value of G) with (FEM) results. The approach developed in this chapter has been shown to model damage with and without pre-existing crack.

Chapter 7

Conclusions

Numerical modelling of damage and failure remains challenging due to the inherent limitation of classical continuum mechanics (CCM). On the other hand, peridynamics (PD) method is an attractive way to handle discontinuities based on integral equilibrium equations naturally. In this thesis, a NOSB PD method has been developed with a stabilised correspondence model as a method with potential for use to handle both large deformations and crack propagation. In previous work, a significant proportion of research in PD has been found to be focused on explicit integration scheme since this scheme is more straightforward to implement. However, the implicit approach offers obvious advantages, including the allowance of larger load steps, and improvement of error control. With these advantages in mind, an implicit non-ordinary state-based peridynamics (NOSB PD) method has been implemented for the first time for large deformation problems. This NOSB PD has been combined with stabilised correspondence model with the aim of introducing additional forces into the PD formulation to overcome zero-energy mode problems. The overview and motivation of this thesis have been introduced in Chapter 1. Chapter 2 has presented the background of PD, providing an in-depth review of the method, a summary of the development in PD since its inception and published literature of both bond-based peridynamics (BB PD) and non-ordinary state-based peridynamics (NOSB PD). The idea of the PD method in the simplest way has been summarised in this chapter, as well as describing current known issues in NOSB PD, such as zero-energy modes. The BB PD formulation has been introduced and implemented as a base for the following chapters, followed by an example to demonstrate the BB PD formulation. The main contributions of this thesis are contained in Chapter 3 through Chapter 6. In the following, the important points and main conclusions of each contributing chapter are summarised.

The explicit non-ordinary state-based peridynamics

In Chapter 3, the BB PD has been extended to the non-ordinary state-based peridynamics (NOSB PD) in order to overcome the limitation of a fixed Poisson's ratio in BB PD. The conventional BB PD has been implemented first. However, the major problem associated with the BB PD is the difficulties on adapting constitutive models into the BB PD framework since its limitation on its fixed effective Poisson's ratio. The NOSB PD implementation has, therefore, been employed, where the issue of zero-energy modes has been addressed, where oscillations exist in the NOSB PD solutions. Adaptive dynamic relaxation (ADR) method has been used to guide the solution into the steady-state regime as fast as possible. In addition, the comparison in terms of converging rate has been studied, where the $\Delta t = 1$ and $\Delta t = 10$ performs better as the results are converging faster and stably than the other, as suggested in [81]. The NOSB PD method has been demonstrated with a numerical example showing agreement with an analytical solution and convergence with increasing degrees of freedom. Numerical examples demonstrate the smaller errors induced by, the finer particles' discretisation. The implementation of BB PD and NOSB PD with the introduction of bond failure has been validated using the numerical example to model damage without a pre-existing crack.

Implicit NOSB PD for small deformation analysis

In Chapter 4, the development of NOSB PD with an implicit time integration scheme based on numerically constructed tangent problems has been introduced. The global stiffness matrix based on the numerical expression of the equation of motion of NOSB PD was also explained. The method was then demonstrated with numerical examples to validate the effectiveness of this approach where analytical results exist, and it has been demonstrated that it can provide good results. Results from these examples show for a given particle spacing; a smaller horizon size shows greater accuracy with no control on the zero-energy modes. A comparison of implicit and explicit approaches for peridynamics in solid mechanics focusing on quasi-static problems with large deformations has been presented for the first time using the non-ordinary state-based framework. Both implicit and explicit method predicts the same response. However, implicit time integration with numerically constructed tangent stiffness allows, compared to the techniques based on explicit dynamic relaxation, a reduced computational time.

Stabilised NOSB PD for large deformation analysis

In Chapter 5, an implicit approach of NOSB PD for quasi-static problems with large deformation mechanics with an analytically constructed tangent stiffness has been developed. The numerical implementation of the Jacobian matrices of NOSB PD with a correspondence continuum models for both the unstabilised and stabilised versions [12] have been highlighted in this chapter. A variety of numerical examples subjected to large deformation have been used to assess the accuracy of the method with the inclusion of different stabilisation parameters, to validate the effectiveness of this approach where analytical solutions exist. Results from the numerical examples have shown, horizon sizes, particle spacing and the problem itself appear to be related to the optimum value of G. The results indicated that for a given particle spacing, a smaller horizon size shows greater accuracy with no control on the zero-energy modes. The proposed stabilised correspondence material model allows the boundary condition to be used and bounds for values of the stabilisation parameter G has been observe to ensure stability. Additionally, it has been shown that the value of the optimum stabilisation parameter G used in this chapter is a positive constant less than 1, which has also been suggested by Silling in [12].

Damage in implicit NOSB PD model

In Chapter 6, the NOSB PD with implicit time-integration has been extended to model crack propagation. A modified analytically constructed Jacobian has been introduced in order to study crack propagation problems together with the inclusion of stabilisation parameters. In order to ensure optimum convergence of global equilibrium equations, a degradation in the interaction of the particles has been employed and in order to control accuracy in the simulation, no bonds are allowed to fail during the iterative procedure. Some numerical examples, have been analysed to validate the proposed methods. A quasi-static deformation and fracture problems in the form of a a plate with hole has been analysed with the present approach, and compared with the finite element predictions when failure is not allowed. In addition, the comparison in terms of horizontal displacement has been studied with inclusion of different stabilisation parameter G. It was demonstrated that increasing the value of G offers an acceptable results, suppressing the numerical oscillation of responses and reflecting an effective approach. However, continuing to increase the value of G results in domination of the stabilisation force density over PD force density, which results in the increase of stiffness. The implicit NOSB PD implementation has, therefore, been employed, where the issue of zero-energy modes has been addressed, where oscillations exist in the NOSB PD solutions. In addition, the proposed approach demonstrates its capability of predicting the crack initiation and propagation problems.

7.1 Recommendations and future works

Based on the work undertaken in this thesis, a number of areas could be usefully explored to provide important insights for future research and development. Some of the points are listed below:

- An additional force based on the nonlocal deformation gradient proposed in [12] has been added to the original NOSB PD force states to overcome instability problem due to zero-energy modes in numerical simulations. However, the determination of the additional force still requires stabilisation parameter adjustment, depending on the horizon sizes, particle discretisations and the problem itself. This chosen value of the stabilisation parameter influences the extent of suppression of zero-energy modes and thereby the quality of the solution too. Certainly, to circumvent the instability issue, some other ways could also be considered to make a comparison in terms of accuracy, such as a stress-point method [118].

- Damage has been introduced into the PD model by permitting the bonds between particles to break irreversibly. Breakage occurs when a bond is stretched beyond some prescribed critical amount. This thesis has provided examples of damage based on the critical bond stretch that is followed widely in the PD literature. However, it would be interesting to see the performance of the other damage criteria such as critical energy, critical strain, and critical stress [7, 65, 146] for the proposed implicit NOSB PD.

- Geometric non-linearity has been modelled using the proposed NOSB PD in some problems in this thesis, which gives the structural response under extremely large external loads or low stiffness. The proposed NOSB PD can be further applied to material non-linearity.

- All numerical examples demonstrated in this thesis have two-dimensional geometries. Extending the numerical analyses using NOSB PD to three dimensions which is more realistic and challenging can be further explored.

- There was no emphasis on optimising specific algorithms or parallelisation for use in this thesis. However, simulating three dimensions and real-life problems using PD requires tracking of millions of PD particles over a sufficient time period, due to the non-local nature of PD. Implementing the implicit NOSB PD method in a massively parallel computational code could also be considered in further study.

- An approach to couple implicit stabilised nordinary state-based peridynamics (NOSB PD) with finite element method (FEM) can be further explored proposed. The coupling method can provide an accurate result and at the same time greatly reduces computational cost for any problems involving damages.

7.2 Final thoughts

It is hoped that the ideas presented in this thesis would be a fruitful area for further research and in the future, the findings of this study would have a number of important implications in some capacity to the progress of the NOSB PD method.

Appendix A

Appendix A

A.1 Material tangent modulus

The derivative of the Piola Kirchhoff with respect to the deformation gradient is given by

$$\begin{aligned} A_{imkn} &= \frac{\partial}{\partial F_{kn}}(\tau_{ip}F^{-T}_{pm}) \\ &= \frac{\partial}{\partial F_{kn}}(\tau_{ip}F^{-1}_{mp}) \\ &= \frac{\partial \tau_{ip}}{\partial F_{kn}}F^{-1}_{mp} + \tau_{ip}\frac{\partial F^{-1}_{mp}}{\partial F_{kn}}, \end{aligned} \tag{A.1.1}$$

and the derivative of the Kirchhoff stress tensor with respect to the deformation gradient in the first term of the right-hand side of Eq. (A.1.1) can be shown to be

$$\begin{aligned} M_{ipkn} &= \frac{\partial \tau_{ip}}{\partial F_{kn}} \\ &= \frac{\partial \tau_{ip}}{\partial \epsilon_{ab}}\frac{\partial \epsilon_{ab}}{\partial c_{cd}}\frac{\partial c_{cd}}{\partial F_{kn}} \\ &= \frac{1}{2}\frac{\partial \tau_{ip}}{\partial \epsilon_{ab}}\frac{\partial ln(c_{ab})}{\partial c_{cd}}\frac{\partial c_{cd}}{\partial F_{kn}}, \end{aligned} \tag{A.1.2}$$

where the derivative of the elastic logarithmic strain tensor with respect to the elastic left Cauchy green strain tensor follows as

$$Q_{abcd} = \frac{\partial \epsilon_{ab}}{\partial c_{cd}} = \frac{1}{2}\frac{\partial ln(c_{ab})}{\partial c_{cd}}, \quad \text{where} \quad c_{ab} = F_{ac}F_{bc}, \tag{A.1.3}$$

and determined as a particular case of the derivative of symmetric second order isotropic tensor function by a symmetric second order argument where Q_{abcd} can be determined as a particular case of the derivative of a general symmetric second order tensor argument (see Miehe [162] for details). Derivative in the second term of the right-hand side of the equation (A.1.2) is given by

$$\frac{\partial \tau_{ip}}{\partial \epsilon_{ab}} = D^e_{ipab}, \tag{A.1.4}$$

where the D^e_{ipab} must be write in four by four matrix notation . Derivative in the last term of the right-hand side of the Eq. (A.1.2) is given by

$$\begin{aligned} N_{cdkn} = \frac{\partial b_{cd}}{\partial F_{kn}} &= \frac{\partial F_{cg} F_{dg}}{\partial F_{kn}} \\ &= F_{dg} \frac{\partial F_{cg}}{\partial F_{kn}} + F_{cg} \frac{\partial F_{dg}}{\partial F_{kn}} \\ &= F_{dg} \delta_{kc} \delta_{gn} + F_{cg} \delta_{kd} \delta_{gn} \\ &= F_{dn} \delta_{kc} + F_{cn} \delta_{kd}, \end{aligned} \tag{A.1.5}$$

where δ_{kc} denotes the Kronecker delta tensor with the following properties

$$\delta_{kc} = 1 \;\text{ if }\; k = c, \quad \delta_{kc} = 0 \;\text{ if }\; k \neq c. \tag{A.1.6}$$

From the relation for the derivative of the inverse of a tensor given in the literature, the derivative in the last term of the right-hand side of the Eq. (A.1.1) is given by

$$B_{pmkn} = \left[\frac{\partial (F^{-1})_{mp}}{\partial F_{kn}} \right]^T = (-(F^{-1})_{mk} (F^{-1})_{np})^T. \tag{A.1.7}$$

Substituting Eq. (A.1.7) into Eq. (A.1.1) gives

$$A_{imkn} = \frac{\partial \tau_{ip}}{\partial F_{kn}} F^{-1}_{mp} - \tau_{ip} F^{-T}_{mk} F^{-T}_{np}. \tag{A.1.8}$$

References

[1] E. Madenci and E. Oterkus, *Peridynamic Theory and Its Applications*. No. 2, New York, NY: Springer New York, 2014.

[2] T. Belytschko, Y. Krongauz, D. Organ, M. Fleming, and P. Krysl, "Meshless methods: An overview and recent developments," *Computer Methods in Applied Mechanics and Engineering*, vol. 139, no. 1-4, pp. 3–47, 1996.

[3] V. G. Patel and N. V. Rachchh, "Meshless method–review on recent developments," *Materials Today: Proceedings*, 2020.

[4] D. Hu, S. Long, X. Han, and G. Li, "A meshless local petrov–galerkin method for large deformation contact analysis of elastomers," *Engineering Analysis with Boundary Elements*, vol. 31, no. 7, pp. 657–666, 2007.

[5] S. A. Silling, "Reformulation of elasticity theory for discontinuities and long-range forces," *Journal of the Mechanics and Physics of Solids*, vol. 48, no. 1, pp. 175–209, 2000.

[6] D. Huang, G. Lu, C. Wang, and P. Qiao, "An extended peridynamic approach for deformation and fracture analysis," *Engineering Fracture Mechanics*, vol. 141, pp. 196–211, 2015.

[7] W. Y. Zhou, X. and Q. Qian, "Numerical simulation of crack curving and branching in brittle materials under dynamic loads using the extended non-ordinary state-based peridynamics," *European Journal of Mechanics, A/Solids*, vol. 60, pp. 277–299, 2016.

[8] Z. Z. K. A. Basoglu, M.F. and E. Oterkus, "A computational model of peridynamic theory for deflecting behavior of crack propagation with micro-cracks," *Computational Materials Science*, vol. 162, no. November 2018, pp. 33–46, 2019.

[9] Y. Ha and F. Bobaru, “Studies of dynamic crack propagation and crack branching with peridynamics,” *International Journal of Fracture*, vol. 162, no. 1-2, pp. 229–244, 2010.

[10] S. A. Silling and R. B. Lehoucq, “Convergence of peridynamics to classical elasticity theory,” *Journal of Elasticity*, vol. 93, no. 1, pp. 13–37, 2008.

[11] S. A. Silling and F. Bobaru, “Peridynamic modeling of membranes and fibers,” *International Journal of Non-Linear Mechanics*, vol. 40, no. 2-3, pp. 395–409, 2005.

[12] S. A. Silling, “Stability of peridynamic correspondence material models and their particle discretizations,” *Computer Methods in Applied Mechanics and Engineering*, vol. 322, pp. 42–57, 2017.

[13] O. C. Zienkiewicz, M. Huang, and M. Pastor, “Localization problems in plasticity using finite elements with adaptive remeshing,” *International Journal for Numerical and Analytical Methods in Geomechanics*, vol. 19, no. 2, pp. 127–148, 1995.

[14] J.-F. Remacle, C. Geuzaine, G. Compère, and E. Marchandise, “High-quality surface remeshing using harmonic maps,” *International Journal for Numerical Methods in Engineering*, vol. 83, no. 4, pp. 403–425, 2010.

[15] A. Maligno, S. Rajaratnam, S. Leen, and E. Williams, “A three-dimensional (3D) numerical study of fatigue crack growth using remeshing techniques,” *Engineering Fracture Mechanics*, vol. 77, no. 1, pp. 94–111, 2010.

[16] H. Stoker, *Developments of the Arbitrary Lagrangian-Eulerian method in non-linear solid mechanics*. PhD thesis, Universiteit Twente, 1999.

[17] N. Moës, J. Dolbow, and T. Belytschko, “A finite element method for crack growth without remeshing,” *International Journal for Numerical Methods in Engineering*, vol. 46, no. 1, pp. 131–150, 1999.

[18] T. Belytschko and T. Black, “Elastic crack growth in finite elements with minimal remeshing,” *International Journal for Numerical Methods in Engineering*, vol. 45, no. 5, pp. 601–620, 1999.

[19] C. Daux, N. Moës, J. Dolbow, N. Sukumar, and T. Belytschko, “Arbitrary branched and intersecting cracks with the extended finite element method,” *International Journal for Numerical Methods in Engineering*, vol. 48, no. 12, pp. 1741–1760, 2000.

[20] N. Moës, J. Dolbow, and T. Belytschko, “A finite element method for crack growth without remeshing,” *International Journal for Numerical Methods in Engineering*, vol. 46, no. 1, pp. 131–150, 1999.

[21] N. Moës and T. Belytschko, “Extended finite element method for cohesive crack growth,” *Engineering Fracture Mechanics*, vol. 69, no. 7, pp. 813–833, 2002.

[22] P. Laborde, J. Pommier, Y. Renard, and M. Salaün, “High-order extended finite element method for cracked domains,” *International Journal for Numerical Methods in Engineering*, vol. 64, no. 3, pp. 354–381, 2005.

[23] F. L. Stazi, E. Budyn, J. Chessa, and T. Belytschko, “An extended finite element method with higher-order elements for curved cracks,” *Computational Mechanics*, vol. 31, no. 1-2, pp. 38–48, 2003.

[24] G. Zi, J. Song, E. Budyn, S. Lee, and T. Belytschko, “A method for growing multiple cracks without remeshing and its application to fatigue crack growth,” *Modelling and Simulation in Materials Science and Engineering*, vol. 12, no. 5, pp. 901–915, 2004.

[25] C. Daux, N. MoÃ«s, J. Dolbow, N. Sukumar, and T. Belytschko, “Arbitrary branched and intersecting cracks with the extended finite element method,” *International Journal for Numerical Methods in Engineering*, vol. 48, no. 12, pp. 1741–1760, 2000.

[26] T. Belytschko, D. Organ, and C. Gerlach, “Element-free galerkin methods for dynamic fracture in concrete,” *Computer Methods in Applied Mechanics and Engineering*, vol. 187, no. 3-4, pp. 385–399, 2000.

[27] L. B. Lucy, “A numerical approach to the testing of the fission hypothesis,” *The Astronomical Journal*, vol. 82, p. 1013, 1977.

[28] P. Cleary and R. Das, “The Potential for SPH Modelling of Solid Deformation and Fracture,” in *IUTAM Symposium on Theoretical, Computational and Modelling Aspects of Inelastic Media*, pp. 287–296, Dordrecht: Springer Netherlands, 2008.

[29] W. Benz and E. Asphaug, “Simulations of brittle solids using smooth particle hydrodynamics,” *Computer Physics Communications*, vol. 87, no. 1-2, pp. 253–265, 1995.

[30] P. Randles and L. Libersky, "Smoothed Particle Hydrodynamics: Some recent improvements and applications," *Computer Methods in Applied Mechanics and Engineering*, vol. 139, no. 1-4, pp. 375–408, 1996.

[31] V. Mehra, C. Sijoy, V. Mishra, and S. Chaturvedi, "Tensile instability and artificial stresses in impact problems in sph," in *Journal of Physics: Conference Series*, vol. 377, p. 012102, IOP Publishing, 2012.

[32] T. Belytschko, Y. Y. Lu, and L. Gu, "Element-free Galerkin methods," *International Journal for Numerical Methods in Engineering*, vol. 37, no. 2, pp. 229–256, 1994.

[33] T. Belytschko, L. Gu, and Y. Y. Lu, "Fracture and crack growth by element free Galerkin methods," *Modelling and Simulation in Materials Science and Engineering*, vol. 2, no. 3A, pp. 519–534, 1994.

[34] T. Belytschko, Y. Lu, L. Gu, and M. Tabbara, "Element-free galerkin methods for static and dynamic fracture," *International Journal of Solids and Structures*, vol. 32, no. 17-18, pp. 2547–2570, 1995.

[35] G. Ventura, J. X. Xu, and T. Belytschko, "A vector level set method and new discontinuity approximations for crack growth by EFG," *International Journal for Numerical Methods in Engineering*, vol. 54, no. 6, pp. 923–944, 2002.

[36] A. C. Zhuang, X. and S. Bordas, "Accurate fracture modelling using meshless methods, the visibility criterion and level sets: Formulation and 2D modelling," *International Journal for Numerical Methods in Engineering*, vol. 86, no. 2, pp. 249–268, 2011.

[37] X. Zhuang, C. Augarde, and K. Mathisen, "Fracture modeling using meshless methods and level sets in 3D: Framework and modeling," *International Journal for Numerical Methods in Engineering*, vol. 92, no. 11, pp. 969–998, 2012.

[38] P. A. Cundall and O. D. Strack, "A discrete numerical model for granular assemblies," *geotechnique*, vol. 29, no. 1, pp. 47–65, 1979.

[39] B. Chiaia, A. Vervuurt, and J. Van Mier, "Lattice model evaluation of progressive failure in disordered particle composites," *Engineering Fracture Mechanics*, vol. 57, no. 2-3, pp. 301–318, 1997.

[40] F. A. Tavarez and M. E. Plesha, "Discrete element method for modelling solid and particulate materials," *International journal for numerical methods in engineering*, vol. 70, no. 4, pp. 379–404, 2007.

[41] F. V. Donzé, V. Richefeu, and S.-A. Magnier, “Advances in discrete element method applied to soil, rock and concrete mechanics,” *Electronic Journal of Geotechnical Engineering*, vol. 8, no. 1, p. 44, 2009.

[42] K. J. Hanley, C. O’Sullivan, and X. Huang, “Particle-scale mechanics of sand crushing in compression and shearing using dem,” *Soils and Foundations*, vol. 55, no. 5, pp. 1100–1112, 2015.

[43] S. Lobo-Guerrero, L. E. Vallejo, and L. F. Vesga, “Visualization of crushing evolution in granular materials under compression using dem,” *International Journal of Geomechanics*, vol. 6, no. 3, pp. 195–200, 2006.

[44] T. Zhang, C. Zhang, J. Zou, B. Wang, F. Song, and W. Yang, “Dem exploration of the effect of particle shape on particle breakage in granular assemblies,” *Computers and Geotechnics*, vol. 122, p. 103542, 2020.

[45] J. Lin, E. Bauer, and W. Wu, “A combined method to model grain crushing with dem,” *Geoscience Frontiers*, vol. 11, no. 2, pp. 451–459, 2020.

[46] E. Rougier, A. Munjiza, and N. John, “Numerical comparison of some explicit time integration schemes used in dem, fem/dem and molecular dynamics,” *International journal for numerical methods in engineering*, vol. 61, no. 6, pp. 856–879, 2004.

[47] F. Bertrand, L.-A. Leclaire, and G. Levecque, “Dem-based models for the mixing of granular materials,” *Chemical Engineering Science*, vol. 60, no. 8-9, pp. 2517–2531, 2005.

[48] I. S. Aranson, V. A. Kalatsky, and V. M. Vinokur, “Continuum Field Description of Crack Propagation,” *Physical Review Letters*, vol. 85, no. 1, pp. 118–121, 2000.

[49] K. R. Ambati, M. and L. De Lorenzis, “A phase-field model for ductile fracture at finite strains and its experimental verification,” *Computational Mechanics*, vol. 57, no. 1, pp. 149–167, 2016.

[50] Z. A. Wilson and C. M. Landis, “Phase-field modeling of hydraulic fracture,” *Journal of the Mechanics and Physics of Solids*, vol. 96, pp. 264–290, 2016.

[51] C. Miehe, H. Dal, L.-M. Schänzel, and A. Raina, “A phase-field model for chemo-mechanical induced fracture in lithium-ion battery electrode particles,” *International Journal for Numerical Methods in Engineering*, vol. 106, no. 9, pp. 683–711, 2016.

[52] J. Mehrmashhadi, M. Bahadori, and F. Bobaru, “Comparison of peridynamic and phase-field models for dynamic brittle fracture in glassy materials,” 2020.

[53] S. A. Silling and E. Askari, “A meshfree method based on the peridynamic model of solid mechanics,” *Computers and Structures*, vol. 83, no. 17-18, pp. 1526–1535, 2005.

[54] F. Bobaru, J. T. Foster, P. H. Geubelle, and S. A. Silling, *Handbook of Peridynamic Modeling.* Chapman and Hall/CRC, 2017.

[55] E. Kröner, “Elasticity theory of materials with long range cohesive forces,” *International Journal of Solids and Structures*, vol. 3, no. 5, pp. 731–742, 1967.

[56] A. C. Eringen, C. G. Speziale, and B. S. Kim, “Crack-tip problem in non-local elasticity,” *Journal of the Mechanics and Physics of Solids*, vol. 25, no. 5, pp. 339–355, 1977.

[57] D. Rogula, *Nonlocal Theory of Material Media.* Vienna: Springer Vienna, 1982.

[58] I. A. Kunin, *Elastic Media with Microstructure I*, vol. 26 of *Springer Series in Solid-State Sciences.* Berlin, Heidelberg: Springer Berlin Heidelberg, 1982.

[59] A. C. Eringen and D. G. B. Edelen, “On nonlocal elasticity,” *International Journal of Engineering Science*, vol. 10, no. 3, pp. 233–248, 1972.

[60] R. Jabakhanji and R. H. Mohtar, “A peridynamic model of flow in porous media,” *Advances in Water Resources*, vol. 78, pp. 22–35, 2015.

[61] E. Emmrich and O. Weckner, “The Peridynamic Equation and Its Spatial Discretisation,” *Mathematical Modelling and Analysis*, vol. 12, no. 1, pp. 17–27, 2007.

[62] F. Bobaru and M. Duangpanya, “The peridynamic formulation for transient heat conduction,” *International Journal of Heat and Mass Transfer*, vol. 53, no. 19-20, pp. 4047–4059, 2010.

[63] F. Bobaru and W. Hu, “The meaning, selection, and use of the peridynamic horizon and its relation to crack branching in brittle materials,” *International Journal of Fracture*, vol. 176, no. 2, pp. 215–222, 2012.

[64] W. Gerstle, N. Sau, and S. A. Silling, “Peridynamic modeling of concrete structures,” *Nuclear Engineering and Design*, vol. 237, no. 12-13, pp. 1250–1258, 2007.

[65] J. T. Foster, S. A. Silling, and W. W. Chen, “State based peridynamic modeling of dynamic fracture,” in *9th International Conference on Mechanical and Physical Behaviour of Materials under Dynamic Loading*, no. September 2009, pp. 1529–1535, 2009.

[66] S. A. Silling, M. Epton, O. Weckner, J. Xu, and E. Askari, “Peridynamic States and Constitutive Modeling,” *Journal of Elasticity*, vol. 88, no. 2, pp. 151–184, 2007.

[67] W. Gerstle, N. Sau, and S. A. Silling, “Peridynamic modeling of plain and reinforced concrete structures,” *18th International Conference on Structural Mechanics in Reactor Technology (SMiRT 18)*, no. SMiRT 18, pp. 1–15, 2005.

[68] N. Sau, J. Medina-Mendoza, and A. C. Borbon-Almada, “Peridynamic modelling of reinforced concrete structures,” *Engineering Failure Analysis*, vol. 103, pp. 266–274, 2019.

[69] P. Wu, J. Zhao, Z. Chen, and F. Bobaru, “Validation of a stochastically homogenized peridynamic model for quasi-static fracture in concrete,” *Engineering Fracture Mechanics*, vol. 237, p. 107293, 2020.

[70] K. Dayal and K. Bhattacharya, “Kinetics of phase transformations in the peridynamic formulation of continuum mechanics,” *Journal of the Mechanics and Physics of Solids*, vol. 54, no. 9, pp. 1811–1842, 2006.

[71] M. R. Sadat, K. Muralidharan, G. N. Frantziskonis, and L. Zhang, “From atomic-scale to mesoscale: A characterization of geopolymer composites using molecular dynamics and peridynamics simulations,” *Computational Materials Science*, vol. 186, p. 110038, 2021.

[72] J. Zhan, X. Yao, and F. Han, “An approach of peridynamic modeling associated with molecular dynamics for fracture simulation of particle reinforced metal matrix composites,” *Composite Structures*, vol. 250, p. 112613, 2020.

[73] Y. Zhang, H. Deng, J. Deng, C. Liu, and B. Ke, “Peridynamics simulation of crack propagation of ring-shaped specimen like rock under dynamic loading,” *International Journal of Rock Mechanics and Mining Sciences*, vol. 123, p. 104093, 2019.

[74] Y. D. Ha and F. Bobaru, "Characteristics of dynamic brittle fracture captured with peridynamics," *Engineering Fracture Mechanics*, vol. 78, no. 6, pp. 1156–1168, 2011.

[75] D. Huang, G. Lu, and P. Qiao, "An improved peridynamic approach for quasi-static elastic deformation and brittle fracture analysis," *International Journal of Mechanical Sciences*, vol. 94-95, pp. 111–122, 2015.

[76] B. Kilic and E. Madenci, "An adaptive dynamic relaxation method for quasi-static simulations using the peridynamic theory," *Theoretical and Applied Fracture Mechanics*, vol. 53, no. 3, pp. 194–204, 2010.

[77] M. S. Breitenfeld, P. H. Geubelle, O. Weckner, and S. A. Silling, "Non-ordinary state-based peridynamic analysis of stationary crack problems," *Computer Methods in Applied Mechanics and Engineering*, vol. 272, pp. 233–250, 2014.

[78] W. Liu and J. W. Hong, "Discretized peridynamics for linear elastic solids," *Computational Mechanics*, vol. 50, no. 5, pp. 579–590, 2012.

[79] O. Weckner and R. Abeyaratne, "The effect of long-range forces on the dynamics of a bar," *Journal of the Mechanics and Physics of Solids*, vol. 53, no. 3, pp. 705–728, 2005.

[80] Z. Q. Huang, D. and P. Qiao, "Damage and progressive failure of concrete structures using non-local peridynamic modeling," *Science China Technological Sciences*, vol. 54, no. 3, pp. 591–596, 2011.

[81] B. Kilic and E. Madenci, "Prediction of crack paths in a quenched glass plate by using peridynamic theory," *International Journal of Fracture*, vol. 156, no. 2, pp. 165–177, 2009.

[82] J. Lu, Y. Zhang, H. Muhammad, Z. Chen, Y. Xiao, and B. Ye, "3d analysis of anchor bolt pullout in concrete materials using the non-ordinary state-based peridynamics," *Engineering Fracture Mechanics*, vol. 207, pp. 68–85, 2019.

[83] W. Hu, Y. D. Ha, and F. Bobaru, "Peridynamic model for dynamic fracture in unidirectional fiber-reinforced composites," *Computer Methods in Applied Mechanics and Engineering*, vol. 217-220, pp. 247–261, 2012.

[84] B. Kilic, A. Agwai, and E. Madenci, "Peridynamic theory for progressive damage prediction in center-cracked composite laminates," *Composite Structures*, vol. 90, no. 2, pp. 141–151, 2009.

[85] M. E. W. O. S. S. B. P. Oterkus, E. and A. Tessler, “Combined finite element and peridynamic analyses for predicting failure in a stiffened composite curved panel with a central slot,” *Composite Structures*, vol. 94, no. 3, pp. 839–850, 2012.

[86] J. Xu, A. Askari, O. Weckner, and S. A. Silling, “Peridynamic Analysis of Impact Damage in Composite Laminates,” *Journal of Aerospace Engineering*, vol. 21, no. 3, pp. 187–194, 2008.

[87] M. Ghajari, L. Iannucci, and P. Curtis, “A peridynamic material model for the analysis of dynamic crack propagation in orthotropic media,” *Computer Methods in Applied Mechanics and Engineering*, vol. 276, pp. 431–452, 2014.

[88] M. R. Tupek, J. J. Rimoli, and R. Radovitzky, “An approach for incorporating classical continuum damage models in state-based peridynamics,” *Computer Methods in Applied Mechanics and Engineering*, vol. 263, pp. 20–26, 2013.

[89] F. Bobaru and Y. D. Ha, “Adaptive Refinement and Multiscale Modeling in 2D Peridynamics,” *International Journal for Multiscale Computational Engineering*, vol. 9, no. 6, pp. 635–660, 2011.

[90] F. Bobaru and M. Duangpanya, “A peridynamic formulation for transient heat conduction in bodies with evolving discontinuities,” *Journal of Computational Physics*, vol. 231, no. 7, pp. 2764–2785, 2012.

[91] P. Seleson and M. Parks, “On the role of the influence function in the peridynamic theory,” *International Journal for Multiscale Computational Engineering*, vol. 9, no. 6, pp. 689–706, 2011.

[92] R. W. Macek and S. A. Silling, “Peridynamics via finite element analysis,” *Finite Elements in Analysis and Design*, vol. 43, no. 15, pp. 1169–1178, 2007.

[93] Y. Azdoud, F. Han, and G. Lubineau, “A Morphing framework to couple non-local and local anisotropic continua,” *International Journal of Solids and Structures*, vol. 50, no. 9, pp. 1332–1341, 2013.

[94] Y. Azdoud, F. Han, and G. Lubineau, “The morphing method as a flexible tool for adaptive local/non-local simulation of static fracture,” *Computational Mechanics*, vol. 54, no. 3, pp. 711–722, 2014.

[95] G. Lubineau, Y. Azdoud, F. Han, C. Rey, and A. Askari, “A morphing strategy to couple non-local to local continuum mechanics,” *Journal of the Mechanics and Physics of Solids*, vol. 60, no. 6, pp. 1088–1102, 2012.

[96] S. Liu, G. Fang, J. Liang, and M. Fu, “A coupling method of non-ordinary state-based peridynamics and finite element method,” *European Journal of Mechanics-A/Solids*, vol. 85, p. 104075.

[97] S. A. Silling, “Linearized Theory of Peridynamic States,” *Journal of Elasticity*, vol. 99, no. 1, pp. 85–111, 2010.

[98] C. T. Nguyen and S. Oterkus, “Ordinary state-based peridynamic model for geometrically nonlinear analysis,” *Engineering Fracture Mechanics*, vol. 224, p. 106750, 2020.

[99] L. Wu, L. Wang, D. Huang, and Y. Xu, “An ordinary state-based peridynamic modeling for dynamic fracture of laminated glass under low-velocity impact,” *Composite Structures*, vol. 234, p. 111722, 2020.

[100] Z. Liu, Y. Bie, Z. Cui, and X. Cui, “Ordinary state-based peridynamics for nonlinear hardening plastic materials’ deformation and its fracture process,” *Engineering Fracture Mechanics*, vol. 223, p. 106782, 2020.

[101] S. R. Kazemi, “Plastic deformation due to high-velocity impact using ordinary state-based peridynamic theory,” *International Journal of Impact Engineering*, vol. 137, p. 103470, 2020.

[102] S. S. Kulkarni and A. Tabarraei, “An ordinary state based peridynamic correspondence model for metal creep,” *Engineering Fracture Mechanics*, p. 107042, 2020.

[103] Y. Zhang, D. Huang, Z. Cai, and Y. Xu, “An extended ordinary state-based peridynamic approach for modelling hydraulic fracturing,” *Engineering Fracture Mechanics*, p. 107086, 2020.

[104] H. Zhang and P. Qiao, “A two-dimensional ordinary state-based peridynamic model for elastic and fracture analysis,” *Engineering Fracture Mechanics*, p. 107040, 2020.

[105] M. Ozdemir, A. Kefal, M. Imachi, S. Tanaka, and E. Oterkus, “Dynamic fracture analysis of functionally graded materials using ordinary state-based peridynamics,” *Composite Structures*, p. 112296, 2020.

[106] Y. Bie, Z. Liu, H. Yang, and X. Cui, “Abaqus implementation of dual peridynamics for brittle fracture,” *Computer Methods in Applied Mechanics and Engineering*, vol. 372, p. 113398, 2020.

[107] M. Imachi, S. Tanaka, and T. Q. Bui, “Mixed-mode dynamic stress intensity factors evaluation using ordinary state-based peridynamics,” *Theoretical and Applied Fracture Mechanics*, vol. 93, pp. 97–104, 2018.

[108] T. L. Warren, S. A. Silling, A. Askari, O. Weckner, M. A. Epton, and J. Xu, “A non-ordinary state-based peridynamic method to model solid material deformation and fracture,” *International Journal of Solids and Structures*, vol. 46, no. 5, pp. 1186–1195, 2009.

[109] J. O’Grady and J. Foster, “Peridynamic beams: A non-ordinary, state-based model,” *International Journal of Solids and Structures*, vol. 51, no. 18, pp. 3177–3183, 2014.

[110] J. O’Grady and J. Foster, “Peridynamic plates and flat shells: A non-ordinary, state-based model,” *International Journal of Solids and Structures*, vol. 51, no. 25-26, pp. 4572–4579, 2014.

[111] C. T. Wu and B. Ren, “A stabilized non-ordinary state-based peridynamics for the nonlocal ductile material failure analysis in metal machining process,” *Computer Methods in Applied Mechanics and Engineering*, vol. 291, pp. 197–215, 2015.

[112] X. P. Zhou and Y. T. Wang, “Numerical simulation of crack propagation and coalescence in pre-cracked rock-like Brazilian disks using the non-ordinary state-based peridynamics,” *International Journal of Rock Mechanics and Mining Sciences*, vol. 89, pp. 235–249, 2016.

[113] J. Amani, E. Oterkus, P. Areias, G. Zi, T. Nguyen-Thoi, and T. Rabczuk, “A non-ordinary state-based peridynamics formulation for thermoplastic fracture,” *International Journal of Impact Engineering*, vol. 87, pp. 83–94, 2016.

[114] Y. Wang, X. Zhou, and X. Xu, “Numerical simulation of propagation and coalescence of flaws in rock materials under compressive loads using the extended non-ordinary state-based peridynamics,” *Engineering Fracture Mechanics*, vol. 163, pp. 248–273, 2016.

[115] A. Yaghoobi and M. G. Chorzepa, “Higher-order approximation to suppress the zero-energy mode in non-ordinary state-based peridynamics,” *Computers and Structures*, vol. 188, pp. 63–79, 2017.

[116] P. Li, Z. M. Hao, and W. Q. Zhen, “A stabilized non-ordinary state-based peridynamic model,” *Computer Methods in Applied Mechanics and Engineering*, vol. 339, pp. 262–280, 2018.

[117] G. Hattori, J. Trevelyan, and W. M. Coombs, “A non-ordinary state-based peridynamics framework for anisotropic materials,” *Computer Methods in Applied Mechanics and Engineering*, vol. 339, pp. 416–442, 2018.

[118] J. Luo and V. Sundararaghavan, “Stress-point method for stabilizing zero-energy modes in non-ordinary state-based peridynamics,” *International Journal of Solids and Structures*, vol. 150, pp. 197–207, 2018.

[119] M. E. Gu, X. and Q. Zhang, “Revisit of non-ordinary state-based peridynamics,” *Engineering Fracture Mechanics*, vol. 190, pp. 31–52, 2018.

[120] C. Nicely, S. Tang, and D. Qian, “Nonlocal matching boundary conditions for non-ordinary peridynamics with correspondence material model,” *Computer Methods in Applied Mechanics and Engineering*, vol. 338, pp. 463–490, 2018.

[121] X. Lai, L. Liu, S. Li, M. Zeleke, Q. Liu, and Z. Wang, “A non-ordinary state-based peridynamics modeling of fractures in quasi-brittle materials,” *International Journal of Impact Engineering*, vol. 111, pp. 130–146, 2018.

[122] S. Shang, X. Qin, H. Li, and X. Cao, “An application of non-ordinary state-based peridynamics theory in cutting process modelling of unidirectional carbon fiber reinforced polymer material,” *Composite Structures*, vol. 226, p. 111194, 2019.

[123] Z. Q. Gu, X. and E. Madenci, “Non-ordinary state-based peridynamic simulation of elastoplastic deformation and dynamic cracking of polycrystal,” *Engineering Fracture Mechanics*, vol. 218, p. 106568, 2019.

[124] Y. Hu, G. Feng, S. Li, W. Sheng, and C. Zhang, “Numerical modelling of ductile fracture in steel plates with non-ordinary state-based peridynamics,” *Engineering Fracture Mechanics*, vol. 225, p. 106446, 2020.

[125] D. J. Littlewood, “A Nonlocal Approach to Modeling Crack Nucleation in AA 7075-T651,” in *Volume 8: Mechanics of Solids, Structures and Fluids; Vibration, Acoustics and Wave Propagation*, pp. 567–576, ASME, 2011.

[126] H. Wang, Y. Xu, and D. Huang, “A non-ordinary state-based peridynamic formulation for thermo-visco-plastic deformation and impact fracture,” *International Journal of Mechanical Sciences*, vol. 159, pp. 336–344, 2019.

[127] X. Gu, Q. Zhang, D. Huang, and Y. Yv, “Wave dispersion analysis and simulation method for concrete SHPB test in peridynamics,” *Engineering Fracture Mechanics*, vol. 160, pp. 124–137, 2016.

[128] W. Liu and J. W. Hong, “A coupling approach of discretized peridynamics with finite element method,” *Computer Methods in Applied Mechanics and Engineering*, vol. 245-246, pp. 163–175, 2012.

[129] S. Sun and V. Sundararaghavan, “A peridynamic implementation of crystal plasticity,” *International Journal of Solids and Structures*, vol. 51, no. 19-20, pp. 3350–3360, 2014.

[130] M. Brothers, J. T. Foster, and H. R. Millwater, “A comparison of different methods for calculating tangent-stiffness matrices in a massively parallel computational peridynamics code,” *Computer Methods in Applied Mechanics and Engineering*, vol. 279, pp. 247–267, 2014.

[131] Y. Wang, X. Zhou, Y. Wang, and Y. Shou, “A 3-D conjugated bond-pair-based peridynamic formulation for initiation and propagation of cracks in brittle solids,” *International Journal of Solids and Structures*, vol. 134, pp. 89–115, 2018.

[132] M. L. Parks, D. J. Littlewood, J. A. Mitchell, and S. A. Silling, “Peridigm usersâ guide v1. 0.0,” *SAND Report*, vol. 7800, 2012.

[133] E. T. Phipps, D. M. Gay, and R. Bartlett, “Sacado: Automatic differentiation tools for c++ codes.,” tech. rep., Sandia National Lab.(SNL-NM), Albuquerque, NM (United States), 2009.

[134] M. R. Tupek and R. Radovitzky, “An extended constitutive correspondence formulation of peridynamics based on nonlinear bond-strain measures,” *Journal of the Mechanics and Physics of Solids*, vol. 65, no. 1, pp. 82–92, 2014.

[135] H. Cui, C. Li, and H. Zheng, “A higher-order stress point method for non-ordinary state-based peridynamics,” *Engineering Analysis with Boundary Elements*, vol. 117, no. 10, pp. 104–118, 2020.

[136] M. Behzadinasab and J. T. Foster, “On the stability of the generalized, finite deformation correspondence model of peridynamics,” *International Journal of Solids and Structures*, vol. 182, pp. 64–76, 2020.

[137] E. Madenci, M. Dorduncu, N. Phan, and X. Gu, "Weak form of bond-associated non-ordinary state-based peridynamics free of zero energy modes with uniform or non-uniform discretization," *Engineering Fracture Mechanics*, vol. 218, p. 106613, 2019.

[138] S. R. Chowdhury, P. Roy, D. Roy, and J. Reddy, "A modified peridynamics correspondence principle: Removal of zero-energy deformation and other implications," *Computer Methods in Applied Mechanics and Engineering*, vol. 346, pp. 530–549, 2019.

[139] X. Gu, Q. Zhang, E. Madenci, and X. Xia, "Possible causes of numerical oscillations in non-ordinary state-based peridynamics and a bond-associated higher-order stabilized model," *Computer Methods in Applied Mechanics and Engineering*, vol. 357, p. 112592, 2019.

[140] D. P. Flanagan and T. Belytschko, "A uniform strain hexahedron and quadrilateral with orthogonal hourglass control," *International Journal for Numerical Methods in Engineering*, vol. 17, no. 5, pp. 679–706, 1981.

[141] S. Oterkus, *Peridynamics for the solution of multiphysics problems*. PhD thesis, The University of Arizona, 2015.

[142] C. Diyaroglu, E. Oterkus, S. Oterkus, and E. Madenci, "Peridynamics for bending of beams and plates with transverse shear deformation," *International Journal of Solids and Structures*, vol. 69-70, pp. 152–168, 2015.

[143] Z. Yang, E. Oterkus, and C. Tien, "Implementation of peridynamic beam and plate formulations," *Continuum Mechanics and Thermodynamics*, vol. 31, no. 1, pp. 301–315, 2019.

[144] S. R. Mase, G.T. and J. Rossmann, *Continuum Mechanics for Engineers, Third Edition*. CRC Press, 2009.

[145] P. Seleson, S. Beneddine, and S. Prudhomme, "A force-based coupling scheme for peridynamics and classical elasticity," *Computational Materials Science*, vol. 66, pp. 34–49, 2013.

[146] Z. X. Ren, H. and T. Rabczuk, "A new peridynamic formulation with shear deformation for elastic solid," 2016.

[147] E. Madenci, K. Colavito, and N. Phan, "Peridynamics for unguided crack growth prediction under mixed-mode loading," *Engineering Fracture Mechanics*, vol. 167, pp. 34–44, 2016.

[148] Y. Zhang and P. Qiao, “Peridynamic Simulation of Two-dimensional Axisymmetric Pull-out Tests,” *International Journal of Solids and Structures*, vol. 168, pp. 42–57, 2019.

[149] A. Queiruga and G. Moridis, “Numerical experiments on the convergence properties of state-based peridynamic laws and influence functions in two-dimensional problems,” *Computer Methods in Applied Mechanics and Engineering*, vol. 322, pp. 97–122, 2017.

[150] D. Flanagan and L. Taylor, “An accurate numerical algorithm for stress integration with finite rotations,” *Computer methods in applied mechanics and engineering*, vol. 62, no. 3, pp. 305–320, 1987.

[151] S. Niazi, Z. Chen, and F. Bobaru, “Crack nucleation in brittle and quasi-brittle materials: A peridynamic analysis,” 2020.

[152] N. M. Newmark, “A Method of Computation for Structural Dynamics,” *ASCE Journal of the Engineering Mechanics Division*, vol. 85, pp. 67–94, 1959.

[153] P. Underwood, “Dynamic relaxation,” *Computational method for transient analysis*, vol. 1, pp. 245–263, 1986.

[154] B. Kilic and E. Madenci, “Structural stability and failure analysis using peridynamic theory,” *International Journal of Non-Linear Mechanics*, vol. 44, no. 8, pp. 845–854, 2009.

[155] T. Molstad, *Finite Deformation Analysis using the Finite Element Method.* PhD thesis, University of British Columbia, 1977.

[156] J. O’Grady and J. Foster, “Peridynamic beams: a non-ordinary, state-based model,” *International Journal of Solids and Structures*, vol. 51, no. 18, pp. 3177–3183, 2014.

[157] P. Deuflhard, *Newton Methods for Nonlinear Problems: Affine Invariance and Adaptive Algorithms*, vol. 35. Springer Publishing Company, Incorporated, 2011.

[158] N. A. Hashim, W. Coombs, C. Augarde, and G. Hattori, “An implicit non-ordinary state-based peridynamics with stabilised correspondence material model for finite deformation analysis,” *Computer Methods in Applied Mechanics and Engineering*, vol. 371, p. 113304, 2020.

[159] M. Zaccariotto, F. Luongo, G. Sarego, and U. Galvanetto, "Examples of applications of the peridynamic theory to the solution of static equilibrium problems," *The Aeronautical Journal*, vol. 119, no. 1216, pp. 677–700, 2015.

[160] M. Zaccariotto, T. Mudric, D. Tomasi, A. Shojaei, and U. Galvanetto, "Coupling of FEM meshes with Peridynamic grids," *Computer Methods in Applied Mechanics and Engineering*, vol. 330, pp. 471–497, 2018.

[161] Z. M. Z. Q. Ni, T. and U. Galvanetto, "Static solution of crack propagation problems in Peridynamics," *Computer Methods in Applied Mechanics and Engineering*, vol. 346, pp. 126–151, 2019.

[162] C. Miehe, "Comparison of two algorithms for the computation of fourth-order isotropic tensor functions," *Computers & Structures*, vol. 66, no. 1, pp. 37–43, 1998.